University of Groningen

Dynamics of self-propelled colloids and their application as active matter

Choudhury, Udit

IMPORTANT NOTE: You are advised to consult the publisher's version (publisher's PDF) if you wish to cite from it. Please check the document version below.

Document Version
Publisher's PDF, also known as Version of record

Publication date:
2019

Link to publication in University of Groningen/UMCG research database

Citation for published version (APA):
Choudhury, U. (2019). *Dynamics of self-propelled colloids and their application as active matter*. [Thesis fully internal (DIV), University of Groningen]. University of Groningen.

Copyright
Other than for strictly personal use, it is not permitted to download or to forward/distribute the text or part of it without the consent of the author(s) and/or copyright holder(s), unless the work is under an open content license (like Creative Commons).

The publication may also be distributed here under the terms of Article 25fa of the Dutch Copyright Act, indicated by the “Taverne” license. More information can be found on the University of Groningen website: https://www.rug.nl/library/open-access/self-archiving-pure/taverne-amendment.

Take-down policy
If you believe that this document breaches copyright please contact us providing details, and we will remove access to the work immediately and investigate your claim.

Downloaded from the University of Groningen/UMCG research database (Pure): http://www.rug.nl/research/portal. For technical reasons the number of authors shown on this cover page is limited to 10 maximum.

Download date: 05-05-2023

Dynamics of self-propelled colloids and their application as active matter

Udit Choudhury

university of groningen

faculty of mathematics and natural sciences

zernike insitute for advanced materials

The research presented in this thesis was performed in the Max Planck Institute for Intelligent Systems, Germany and the Zernike Institute for Advanced Materials at the University of Groningen, The Netherlands.

MICRO NANO & MOLECULAR SYSTEMS LAB

Zernike Institute PhD thesis series 2019-06

ISSN: 1570-1530

ISBN: 978-94-034-1363-1 (Printed version)

ISBN: 978-94-034-1362-4 (Electronic version)

Print: Studentendrukwerk, Groningen

Cover design by Udit Choudhury

Contents

1 : INTRODUCTION TO ACTIVE COLLOIDS

Colloids move when they are in a suspension due to Brownian motion. However, generally colloids do not move by themselves. This is in contrast to, for instance swimming bacteria, that are at a similar length scale, but have the ability to self-propel by converting chemicals into mechanical motion. In this thesis, inanimate colloidal particles are equipped with catalysts to form self-propelling colloids that can swim in fluids. First, some background information is provided on active self-propelling colloids[1–11], which are model systems to study swimming and the emergence of collective phenomena. To achieve self-propulsion, typically the colloidal particle should consist of different materials or is shape anisotropic and contain a material that can convert an external energy source stemming from a chemical fuel[9] or light into motion.[12]. This thesis studies the dynamics and the fabrication of active colloids. While self-propulsion due to chemical reactions is known, it is also interesting to study the motion of self-propelled colloids in complex environments. The thesis further examines if self-propelling colloids can be used to improve the function of nanosensors. Although considerable theoretical and experimental research has focused on understanding the dynamics of such colloids, there have been limited efforts to develop this field towards realistic applications or to realize 'active materials'. This thesis demonstrates how dense bulk suspension of self-propelled chemically active colloids can form the basis for new 'active materials' – that can be prepared at the gram-scale.

1.1 Colloids at low Reynolds number

Propulsion in fluids at small scales and small speeds is governed by low Reynolds-number physics.[13] The Reynolds number (Re) is a dimensionless number that characterizes fluid flow. It is defined as the ratio of the inertial to the viscous forces exerted on a solid body by the surrounding fluid flow.

$$Re = \frac{Inertial\ Forces}{Viscous\ forces} = \frac{\rho v d}{\mu} \quad , \qquad (1)$$

where, ρ is the density of the fluid, v is the velocity of the flow field, d is the characteristic length scale of the body and μ the dynamic viscosity. At large length scales, for example a human swimming in water, the inertial forces are dominant. So, a solid object (Re>1) can easily move through fluid by employing a strategy of geometrically reciprocal motion.

However, this strategy fails at low Reynolds number (Re << 1), where inertia plays no role. Consequently, reciprocal motion causes no net fluid motion and the object cannot propel.[12]

In this regime, the Navier-Stokes equations simplify to the Stokes equations , which are in the overall force-free case,

$$\nabla p - \mu \nabla^2 v = 0, \quad \nabla . v = 0 \tag{2}$$

where, p is the pressure, v is the velocity and μ is the viscosity. It is seen that there is no explicit time dependence. For an object to swim or self-propel at low Reynolds number it is therefore important that it generates a time non-reciprocal flow, i.e. breaks symmetry. In case of self-propelling colloids this may be achieved by virtue of the geometry of the colloid. Symmetry is broken by the asymmetric distribution of catalyst on the surface of the swimmer. It follows that in the presence of a fuel the catalytic reaction occurs only on a particular region of the two-faced "Janus" particle which gives rise to a gradient of the reaction product molecules. This locally generated gradient propels the colloid by a "self"-phoretic mechanism.[10,14,15]

In what follows the most common phoretic mechanisms are discussed, in particular self-diffusiophoresis[16] and self-thermophoresis[17], as well as the fabrication of self-propelling colloidal swimmers.

1.2 Phoresis and self-phoresis

Phoretic transport is motion of a colloid under the influence of an external field.[18] A solid colloid immersed in a fluid develops an interfacial boundary layer around it. The thickness of this layer is much smaller than the diameter of the microparticle. Under the influence of an external field like an electric field, or a chemical, or temperature gradient, the fluid in this layer moves. Considering the solid colloid plus the thin boundary layer as a whole, there is no net force that is applied to the particle by the external gradient. Hence, the motion of the phoretic particles can be considered as overall force and torque-free.

Diffusiophoresis is the motion of a colloid under the influence of a chemical concentration gradient. In self-diffusiophoresis, the colloid itself generates a local chemical gradient.

Commonly, the colloidal particle is half coated with a catalyst via physical vapor deposition (PVD) process.[19] The catalyst reacts with the fuel in the solution and product molecules are released into the solution (Figure 1.1). The colloidal particle and the product molecules experience either an attractive or a repulsive interaction that is governed by van der Waals force, steric repulsion, depletion or electrostatic interactions.[16] Due to the asymmetry of the distribution of catalyst on the particle a chemical concentration gradient is established across the body of the colloid and a net propulsive force acts on the colloid.

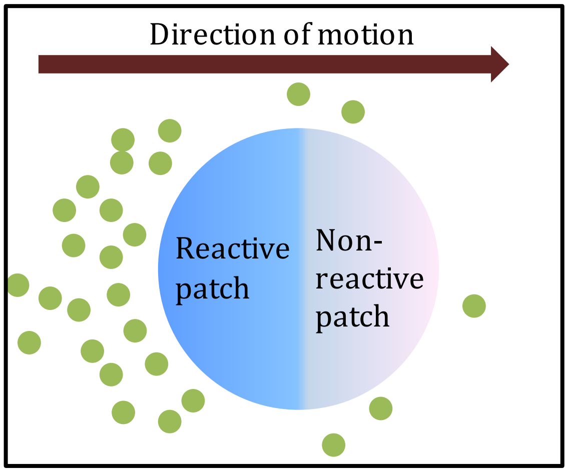

Figure 1.1 Example of a self-diffusiophoretic colloid. The direction of motion will depend on the particular chemical potentials.

In practice this is implemented by fabricating Janus particles[20–22] which have a reactive and a non-reactive surface. In case of diffusiophoresis common types of self-propelled colloids are silicon-dioxide (SiO_2)–Platinum (Pt) swimmers, or polystyrene(PS)-Platinum swimmers. Hydrogen peroxide (H_2O_2) is a common fuel that decomposes in the presence of the Pt catalyst. The speed of a particle exhibiting self-diffusiophoresis is given by[9]

$$V = \frac{3\pi}{2} k a \lambda^2 \tag{3}$$

where k is the reaction rate, a is hydrodynamic radius of the solute (products) and λ is the interaction zone between solute and the particle.

Thermophoresis is the motion of a colloid under the influence of an external temperature gradient.[23,24] The particle may move towards or away from the hotter side depending on whether the colloid is thermophobic or thermophilic. In self-thermophoresis[25] the motion is again not generated by a global gradient, but by an asymmetric temperature profile across the body of the swimmer. In practice, only a part of the swimmer is coated by an active layer like gold or carbon. On illumination by a laser, one side of the colloid can be heated, if it absorbs the light. This causes a local heating on one side of the colloid and causes it to move by thermophoresis in a self-generated temperature gradient. The thermophoretic speed for a spherical colloid is given by[25]

$$V = -DS_T\frac{\Delta T}{3r} \tag{4}$$

where V is the speed of the colloid, D the diffusion coefficient, S_T the Soret coefficient, ΔT the temperature gradient due to the incident laser and r is radius of the particle.

1.3 Fabrication of colloids with Glancing angled deposition

Self-phoretic micro-swimmers are most commonly fabricated by physical vapor deposition (PVD). Firstly, passive colloids are deposited on a wafer, either by drop casting or by Langmuir-Blodgett deposition.[26] Then the wafer with the colloidal particles is loaded in the vacuum deposition chamber. With an electron-beam or a thermal heater, the source material is heated until a vapor flux evaporates from the source material and deposits onto the wafer. In PVD, the wafer faces directly the incoming vapor flux. Since the colloids are typically spherical only the face of the colloids exposed to the vapor flux is coated. These half-coated particles with two faces are called Janus particles. In order to fabricate more complex and anisotropic colloidal structures with PVD the technique of glancing angle deposition is used. In Glancing Angle Deposition (GLAD),[27–29] the wafer is loaded at a very high angle of incidence to the incoming vapor flux. The colloids here act as a seed layer on which material is deposited. At a high angle of incidence, this creates a self-shadowing effect which makes it possible to grow defined shapes on the seeded wafer. Figure 1.2 shows a schematic of GLAD setup to fabricate rod-shaped particles. By rotating and angling the wafer during the deposition it becomes possible to obtain unique shaped structures.[28]

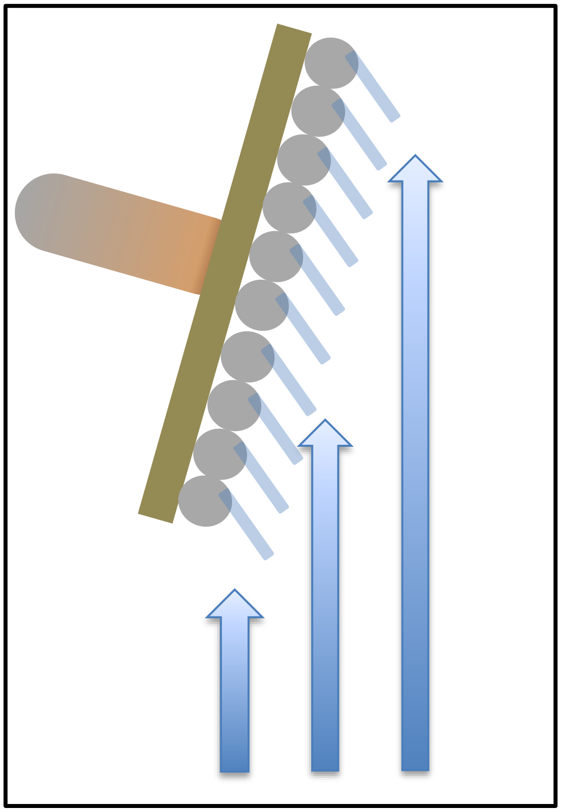

Figure 1.2 Schematic of glancing angle deposition (GLAD) for fabrication of complex colloidal particles that can be removed from the substrate into solution after fabrication. The angle of incidence is here > 80°.

While a considerable amount of research has been devoted to studies of the dynamics and applications of single microswimmers, there is a growing interest to understand the behavior of a collection such microswimmers[30]. Since, microswimmers consume energy to swim, their behavior is inherently out of "thermodynamic equilibrium". The behavior of a collection of such individual units driven out of equilibirum, such as self-propelling colloids, is known as "active matter".[31–34] Broadly, active matter describes materials composed of units that consume energy from their environment to power themselves, such that they can move, and interact with each other. Collective phenomena seen in nature, such as the flocking of birds[35] or the swarming fish serve as models for artificial active matter systems. At the microscale, the most well studied examples are actin-motor protein[36–38] solutions or dense bacterial suspensions.[39,40] Both show non-equilibrium dynamic and steady states as a function of activity or energy consumed from their ambience. Spontaneous symmetry breaking,[41] hierarchal organization,[42] microstructural phase change[43,44] are some of the properties exhibited by these materials. Collective bacterial dynamics was also observed as a function of activity in dense suspensions.[45,46] To mimic these phenomena with the aid of inanimate synthetic "active" colloids, experimental systems of Quincke rollers[47,48] and magnetic rollers[49] have been developed. They show collective behavior like directional motion and fingering of bulk suspensions. With chemically active colloids studied in the thesis, there has not been a 'dense' enough system to study the collective behavior of microswimmers. We address this challenge in our thesis and develop system to study the collective properties of a microswimmer suspension.

The thesis is organized in the following chapters:

Chapter 1 gives a brief introduction to active self-propelling colloids and their fabrication, as well as self-diffusiophoresis and self-thermophoresis.

The following chapters discuss experimental results. Chapter 2 and Chapter 3, concern the enhancement of the propulsion speed of catalytically-propelled microswimmers. The Janus colloids are then used as model system to study active diffusion on a lattice.

Chapter 2 describes how surface roughness affects the propulsion speed of self-diffusiophoretic colloids.[5] I demonstrate that a simple physical vapor deposition based fabrication method can be used to obtain self-propelled active Janus micro particles with rough catalytic platinum surfaces that show a four-fold increase in their propulsion speed compared to conventional Janus particles coated with a smooth Pt layer.

In Chapter 3, I present results from a study of self-propelled Janus colloids moving atop a two-dimensional crystalline surface realized as a hexagonally close-packed monolayer of colloidal particles of the same size as the mobile one.[21] The dynamics of the self-propelled colloid reflects the competition between the periodic surface, hindered diffusion, and active motion, as well as enhanced diffusion. The mean-square displacements obtained from the experiment exhibit enhanced diffusion at long lag times, which is reduced compared to the case of a planar surface. This study experimentally demonstrates the effects the surface topography has on the motion of active colloids.

In Chapter 4 and Chapter 5, I describe a mechanism to obtain very large numbers of active colloids and I describe two applications for active microswimmers.

In Chapter 4, I show how nanodiamonds can be coupled to colloids to make swimmers that can also function as a sensor.[50] Nanodiamonds are emerging as nanoscale quantum probes for bio-sensing and imaging. This necessitates the development of new methods to accurately manipulate their position and orientation in aqueous solutions.[51–54] I report the realization of an "active" nanodiamond (ND) swimmer in fluids, composed of a ND crystal containing nitrogen vacancy (NV) centers and a light-driven self-thermophoretic micromotor. This hybrid swimmer is propelled by a local temperature gradient created by laser illumination on its metal-coated side. Its locomotion - from translational to rotational motion - is successfully controlled by shape-dependent hydrodynamic interactions. The precise engineering of the swimmer's geometry is achieved by self-assembly combined with physical vapor shadow growth. The optical addressability of the suspended ND swimmers is demonstrated by observing the electron spin resonance in the presence of a magnetic field. Active motion at the nanoscale thus enables new sensing capabilities, including vector magnetometry, combined with active transport.

In Chapter 5, I develop an active material system: active opto-rheological fluids, whose rheological properties can be reversibly modulated as a function of the chemical activity and light intensity. These “active colloids”, convert chemical energy stored in the fuel molecules into motion to self-propel and interact with their neighbors. While a significant number of studies have focused on developing such individual synthetic active colloids, the properties of dense suspensions of active colloids have not been well-explored experimentally. Several theoretical and a few experimental studies showed the emergence of collective phenomena, as well as pattern formation in these active suspensions. These behaviors are remarkably similar to what is observed in dense bacterial baths. From studies of biological “living” suspensions, we understand that the collective motion of the individual active units change the fundamental nature and bulk properties of the entire suspension. The motion and pattern formation directly correlates with the properties of the suspension. A challenge thus far has been to prepare experimental systems of chemically active colloids in large numbers and at high density. I show how a “dense” chemically active colloidal suspension can be realized. The individual colloids interact chemically by consuming solvent fuel and cause the fluidic suspension to change its bulk viscosity. I demonstrate light triggered reversible change of the active suspension’s viscosity by an order of magnitude.

In Chapter 6, I draw conclusions from my studies on active colloids and discuss possible future directions of research.

The thesis is based on published research. In particular chapters 2, 3, 4, and 5 have been published or have been submitted for publication. In particular,

Chapter 2 is based on the publication: “Surface roughness-induced speed increase for active Janus micromotors:” Udit Choudhury, Lluis Soler, John G. Gibbs, Samuel Sanchez and Peer Fischer, *Chemical Communication*, **51**, 8660-8663, (2015).

Chapter 3 is based on the publication: “Active colloidal propulsion over a crystalline surface “ Udit Choudhury, Arthur V Straube, Peer Fischer, John G Gibbs and Felix Höfling. . *New Journal of Phyics* **19,** 125010 (2017) .

Chapter 4 is based on the publication: “Nanodiamonds that swim” Jitae Kim, Udit Choudhury, Hyeon-Ho Jeong and Peer Fischer *Advanced Materials* **29,**1701024 (2017).

Chapter 5 is based on work that has been submitted for publication: “Chemical nanomotors at the gram scale at high density form an active opto-rheological medium “ Udit Choudhury, Dhruv P. Singh, Tian Qiu, and Peer Fischer . (Under review).

In addition, I have been an author of the following paper that has been prepared during the time of my Ph.D. research:

Non-equilibrium assembly of light activated colloidal mixtures
Dhruv P. Singh ,Udit Choudhury, Peer Fischer and Andrew G. Mark
Advanced Materials **29,** 1701328 (2017).

1.4 References

1. Golestanian, R., Liverpool, T. B. & Ajdari, A. Propulsion of a Molecular Machine by Asymmetric Distribution of Reaction Products. **94,** (2005).
2. Das, S. *et al.* Boundaries can steer active Janus spheres. **6,** 8999 (2015).
3. Wang, W., Duan, W., Sen, A. & Mallouk, T. E. Catalytically powered dynamic assembly of rod-shaped nanomotors and passive tracer particles. **110,** 17744–17749 (2013).
4. Brown, A. & Poon, W. Ionic effects in self-propelled Pt-coated Janus swimmers. **10,** 4016–4027 (2014).
5. Choudhury, U., Soler, L., Gibbs, J. G., Sanchez, S. & Fischer, P. Surface roughness-induced speed increase for active Janus micromotors. **51,** 8660–8663 (2015).
6. Gibbs, J. G. & Zhao, Y. Self-Organized Multiconstituent Catalytic Nanomotors. **6,** 1656–1662 (2010).
7. Singh Dhruv P., Uspal William E., Popescu Mihail N., Wilson Laurence G. & Fischer Peer. Photogravitactic Microswimmers. *Adv. Funct. Mater.* **0,** 1706660 (2018).
8. Lee, T.-C. *et al.* Self-Propelling Nanomotors in the Presence of Strong Brownian Forces. **14,** 2407–2412 (2014).
9. Howse, J. R. *et al.* Self-Motile Colloidal Particles: From Directed Propulsion to Random Walk. **99,** 048102 (2007).
10. Córdova-Figueroa, U. M. & Brady, J. F. Osmotic Propulsion: The Osmotic Motor. *Phys. Rev. Lett.* **100,** 158303 (2008).
11. Brown, A. & Poon, W. Ionic effects in self-propelled Pt-coated Janus swimmers. **10,** 4016 (2014).
12. Kroy, K., Chakraborty, D. & Cichos, F. Hot microswimmers. *Eur. Phys. J. Spec. Top.* **225,** 2207–2225 (2016).
13. Purcell, E. M. Life at low Reynolds number. *Am. J. Phys.* **45,** 3–11 (1977).
14. Brady, J. F. Particle motion driven by solute gradients with application to autonomous motion: continuum and colloidal perspectives. **667,** 216–259 (2011).
15. Velegol, D., Garg, A., Guha, R., Kar, A. & Kumar, M. Origins of concentration gradients for diffusiophoresis. *Soft Matter* **12,** 4686–4703 (2016).

16. Moran, J. L. & Posner, J. D. Phoretic Self-Propulsion. *Annu. Rev. Fluid Mech.* **49,** 511–540 (2017).
17. Jiang, H.-R., Yoshinaga, N. & Sano, M. Active Motion of a Janus Particle by Self-Thermophoresis in a Defocused Laser Beam. **105,** 268302 (2010).
18. Anderson, J. L. Colloid transport by interfacial forces. **21,** 61–99 (1989).
19. Mattox, D. M. Handbook of Physical Vapor Deposition (PVD) Processing. (William Andrew, 2010).
20. Wittmeier, A., Leeth Holterhoff, A., Johnson, J. & Gibbs, J. G. Rotational Analysis of Spherical, Optically Anisotropic Janus Particles by Dynamic Microscopy. *Langmuir* **31,** 10402–10410 (2015).
21. Choudhury, U., Straube, A. V., Fischer, P., Gibbs, J. G. & Höfling, F. Active colloidal propulsion over a crystalline surface. *New J. Phys.* **19,** 125010 (2017).
22. Walther, A. & Müller, A. H. E. Janus Particles: Synthesis, Self-Assembly, Physical Properties, and Applications. *Chem. Rev.* **113,** 5194–5261 (2013).
23. Goldhirsch, I. & Ronis, D. Theory of thermophoresis. I. General considerations and mode-coupling analysis. *Phys. Rev. A* **27,** 1616–1634 (1983).
24. Lin, X., Si, T., Wu, Z. & He, Q. Self-thermophoretic motion of controlled assembled micro-/nanomotors. *Phys. Chem. Chem. Phys.* **19,** 23606–23613 (2017).
25. Jiang, H.-R., Yoshinaga, N. & Sano, M. Active Motion of a Janus Particle by Self-Thermophoresis in a Defocused Laser Beam. *Phys. Rev. Lett.* **105,** 268302 (2010).
26. Gennes, P. G. de. Deposition of Langmuir-Blodgett layers. *Colloid Polym. Sci.* **264,** 463–465 (1986).
27. Introduction: Glancing Angle Deposition Technology. in *Glancing Angle Deposition of Thin Films* 1–30 (Wiley-Blackwell, 2014). doi:10.1002/9781118847510.ch1
28. Mark, A. G., Gibbs, J. G., Lee, T.-C. & Fischer, P. Hybrid nanocolloids with programmed three-dimensional shape and material composition. *Nat. Mater.* **12,** 802–807 (2013).
29. Hawkeye, M. M. & Brett, M. J. Glancing angle deposition: Fabrication, properties, and applications of micro- and nanostructured thin films. *J. Vac. Sci. Technol. A* **25,** 1317–1335 (2007).
30. Bechinger, C. *et al.* Active particles in complex and crowded environments. *Rev. Mod. Phys.* **88,** 045006 (2016).

31. Needleman, D. & Dogic, Z. Active matter at the interface between materials science and cell biology. *Nat. Rev. Mater.* **2,** 17048 (2017).
32. Ramaswamy, S. Active matter. *J. Stat. Mech. Theory Exp.* **2017,** 054002 (2017).
33. Ramaswamy, S. The Mechanics and Statistics of Active Matter. *Annu. Rev. Condens. Matter Phys.* **1,** 323–345 (2010).
34. Hagan, M. F. & Baskaran, A. Emergent self-organization in active materials. *Curr. Opin. Cell Biol.* **38,** 74–80 (2016).
35. Cavagna, A. & Giardina, I. Bird Flocks as Condensed Matter. **5,** 183–207 (2014).
36. Henkin, G., DeCamp, S. J., Chen, D. T. N., Sanchez, T. & Dogic, Z. Tunable dynamics of microtubule-based active isotropic gels. *Philos. Transact. A Math. Phys. Eng. Sci.* **372,** (2014).
37. Schmoller, K. M., Fernández, P., Arevalo, R. C., Blair, D. L. & Bausch, A. R. Cyclic hardening in bundled actin networks. *Nat. Commun.* **1,** 134 (2010).
38. Köhler, S., Schaller, V. & Bausch, A. R. Structure formation in active networks. *Nat. Mater.* **10,** 462 (2011).
39. Zhang, H. P., Be'er, A., Florin, E.-L. & Swinney, H. L. Collective motion and density fluctuations in bacterial colonies. **107,** 13626–13630 (2010).
40. Stenhammar, J., Nardini, C., Nash, R. W., Marenduzzo, D. & Morozov, A. Role of Correlations in the Collective Behavior of Microswimmer Suspensions. *Phys. Rev. Lett.* **119,** 028005 (2017).
41. Tjhung, E., Marenduzzo, D. & Cates, M. E. Spontaneous symmetry breaking in active droplets provides a generic route to motility. *Proc. Natl. Acad. Sci.* **109,** 12381–12386 (2012).
42. Sanchez, T., Chen, D. T. N., DeCamp, S. J., Heymann, M. & Dogic, Z. Spontaneous motion in hierarchically assembled active matter. **491,** 431–434 (2012).
43. Köhler, S., Schaller, V. & Bausch, A. R. Structure formation in active networks. *Nat. Mater.* **10,** 462 (2011).
44. Redner, G. S., Baskaran, A. & Hagan, M. F. Reentrant phase behavior in active colloids with attraction. *Phys. Rev. E* **88,** 012305 (2013).

45. Drescher, K., Dunkel, J., Cisneros, L. H., Ganguly, S. & Goldstein, R. E. Fluid dynamics and noise in bacterial cell–cell and cell–surface scattering. *Proc. Natl. Acad. Sci. U. S. A.* **108,** 10940–10945 (2011).
46. Wioland, H., Lushi, E. & Goldstein, R. E. Directed collective motion of bacteria under channel confinement. *New J. Phys.* **18,** 075002 (2016).
47. Bricard, A. *et al.* Emergent vortices in populations of colloidal rollers. **6,** 7470 (2015).
48. Bricard, A., Caussin, J.-B., Desreumaux, N., Dauchot, O. & Bartolo, D. Emergence of macroscopic directed motion in populations of motile colloids. **503,** 95–98 (2013).
49. Driscoll, M. *et al.* Unstable fronts and motile structures formed by microrollers. *Nat. Phys.* **13,** 375–379 (2017).
50. Kim, J. T., Choudhury, U., Jeong, H.-H. & Fischer, P. Nanodiamonds That Swim. *Adv. Mater.* **29,** 1701024 (2017).
51. Geiselmann, M. *et al.* Three-dimensional optical manipulation of a single electron spin. *Nat. Nanotechnol.* **8,** 175–179 (2013).
52. Horowitz, V. R., Alemán, B. J., Christle, D. J., Cleland, A. N. & Awschalom, D. D. Electron spin resonance of nitrogen-vacancy centers in optically trapped nanodiamonds. *Proc. Natl. Acad. Sci.* **109,** 13493–13497 (2012).
53. Kayci, M., Chang, H.-C. & Radenovic, A. Electron Spin Resonance of Nitrogen-Vacancy Defects Embedded in Single Nanodiamonds in an ABEL Trap. *Nano Lett.* **14,** 5335–5341 (2014).
54. Ropp, C. *et al.* Manipulating Quantum Dots to Nanometer Precision by Control of Flow. *Nano Lett.* **10,** 2525–2530 (2010).

2 : Physical vapor deposition fabricated nanoscale surface patterns increases speed for active Janus micromotors

This chapter is largely based on the journal paper "Surface roughness-induced speed increase for active Janus micromotors" by Udit Choudhury, Lluis Soler, John G. Gibbs, Samuel Sanchez and Peer Fischer in *Chemical Communication* **51**, 8660-8663, (2015).[1] The author designed the experiments together with his co-authors, and fabricated all the samples and analyzed the experimental data. The author was assisted by L.S. in the determination of the catalytic efficiencies and the video-tracking experiments of the colloids..

2.1 Introduction

Catalytically self-propelled Janus particles are model systems to study active matter. The reactive face of the colloid decomposes a fuel present in an aqueous solution and produces a gradient of product molecules across the colloid. The speed of the Janus colloid is thus directly related to the reaction rate and the amount of fuel decomposed by the catalyst. Here, in this chapter the speed enhancement of catalytically propelled Platinum-Janus particles is studied. Since, the propulsion mechanism of the Janus colloids is surface driven catalytic reaction, the surface topography is expected to play a crucial role in determining its speed. A simple versatile physical fabrication method to control surface roughness of Janus micromotors is demonstrated. Self-propelled active Janus microparticles with rough catalytic platinum surfaces were fabricated and they show a four-fold increase in their propulsion speed compared to conventional Janus particles coated with a smooth catalytic Platinum (Pt) layer.

2.2 Motivation

The use of catalytic reactions for self-propulsion of micro and nanoparticles is a well-established means to move colloidal particles in solution at low-Reynolds number.[2,3] To this end, Janus particles with two different faces have been fabricated, including platinum/insulator Janus microspheres, platinum/gold bimetallic nanoparticles and nanorods, and platinum-coated microtubular jets.[3–10] The propulsion in these micromotors arise from the decomposition of hydrogen peroxide (H_2O_2) at the platinum (Pt) surface. While a number of studies have focussed on developing new propulsion systems,[11–13] there have been only a few studies examining the effect of the surface morphology on catalytic self-propulsion.[14–16]

Since the catalytic activity is directly related to the surface area of the catalyst it should be possible to increase the area by introducing nanoscale surface-features.[17] This is commonly used to increase the surface area of conducting electrodes in electrochemical reactions.[18] Hence, one could expect that the incorporation of nanoscale features on the catalytic face of catalytic micro/nanomotors should also lead to a higher effective surface area. This should consequently lead to a higher net turn-over and thus higher propulsion speeds.

Ozin *et al.* studied the motion of electrochemically fabricated rough bimetallic rods produced by incorporating Ludox® silica nano-particles in the electroplating solution for bimetallic nano-rods.[14] Wang *et al.* included carbon nanotubes into the Pt plating solution and obtained much faster speeds of the Au-CNT/Pt nanowires compared with Au-Pt ones.[15] For polystyrene/Pt Janus microspheres a shift in the propulsion mechanism from diffusiophoresis to bubble propulsion was observed after chemically roughening the surface.[15] Increasing the surface roughness of Pt in Pt/insulator Janus particles is, however, not straightforward. First, insulating particles do not lend themselves to direct electrochemical fabrication and typical physical vapor deposition (PVD) methods usually yield smooth surfaces. Further, bimetallic micromotors grown electrochemically have limitations in propulsion in high ionic media. This necessitates exploring different material configurations for studying micro scale propulsion for which physical vapor deposition is a simple and widely used scheme.

Here, a facile method to obtain roughness using PVD is presented. Commonly, Janus particles are grown by sputtering or evaporating a layer of Pt onto silica or polystyrene beads. Pt by itself does not, in general, form rough surfaces. Here it is shown that by first depositing an under-layer of silica before depositing the Pt introduces nanoscale roughness on the Janus particles and that this then automatically yields a rough Pt surface. This leads to a four-fold speed increase compared to particles with a smooth surface. The reaction rates for catalytic propulsion was derived assuming a diffusiophoretic model of propulsion which shows a similar two to four fold increase in turnover rates for rough micromotors. The effect of roughness on catalytic activity was further verified by oxygen evolution tests and observation of the surface topology by SEM.

2.3 Results

The morphology of thin films grown by glancing angle deposition (GLAD), a variant of PVD, where the substrate is tilted relative to the vapor flux to induce shadowed film growth, whilst permitting azimuthal rotation, depends on the deposition rate, the angle of the incident vapor and the material properties. Nanoscale morphology on a plane substrate can be introduced by tilting the substrate at a high angle relative to the vapor flux to induce self-shadowing during the growth. Substrate rotation under glancing angle deposition can promote columnar growth of nanostructures.[19,20] However, metals have higher surface mobilities than (metal) oxides and will therefore diffuse on the substrate easily to form smoother surfaces compared to oxides. This effectively inhibits pure metal thin films, including Pt, from forming rough surfaces.

2.3.1 Fabrication of Janus particles

In this work, two different growth techniques are explored to introduce roughness on smooth silica spheres. First a dense monolayer of silica beads (5 µm diameter) is prepared by drop-casting a diluted suspension of beads onto a clean silicon wafer. After drying, the wafer is placed in a vacuum PVD system. Two types of rough Pt Janus particles were grown, named R_1 and R_2.

Both preparation methods are described below:

R_1 : Preparation of Pt Janus micromotors under nominally normal incidence: 80 nm of SiO_2 was deposited by an e-beam evaporator at 0^0 (normal incidence) as the first layer onto the silica beads followed by 7 nm of titanium (Ti) and 20 nm of Pt (Fig. 2.1a). Ti serves as an adhesion layer. The vapor flux necessarily impinges on the curved surfaces of the silica beads with varying angles of incidence: 90^0 at the equator to 0^0 at the pole. This procedure promotes patchy growth on the particle surface (as can be seen in Fig. 2.1c).

R_2 : Preparation of Pt Janus micromotors under nominally oblique angles: To stimulate growth of columnar structures on the surface of the microspheres the deposition of SiO_2 was performed by tilting the substrate inside the e-beam evaporation chamber. This resulted in high angles of incidence ($\alpha = 87^0$ at the pole, Fig. 2.1b). In addition, the substrate was rotated about the azimuth at five revolutions per minute (Fig 2.1b). Keeping the azimuthal rotation speed constant, the substrate tilt angle α was continuously swept from 87^0 to 0^0 to ensure even hemispherical coverage of the surface of the microsphere (Fig 2.1b). The SiO_2 deposition is followed by a 7 nm layer of Ti and then a 20 nm layer of Pt, both at nominally normal (0^0 incidence. It is important to note that the same amount of SiO_2 is deposited in both fabrication procedures R_1 and R_2.

To facilitate the direct comparison with conventional fabrication of spherical Janus micromotors, two different types of Janus particles are fabricated for control purposes, named S_1 and S_2, which are described below:

S_1 : 7 nm Ti and 20 nm Pt were evaporated keeping the substrate fixed at 0^0 on a monolayer of silica beads(see Fig. 2.1a).

S_2 : 80 nm of Ti and 20 nm of Pt was evaporated while keeping the substrate fixed at 0^0 to ensure that the particles exhibit a diameter comparable to the Janus particles of R_1 and R_2. However, here the Pt surface is smoother than for the particles in R_1 and R_2 due to the higher surface mobility of the Ti adatoms. The surface-smoothness is comparable to the particles in S_1.

To determine the surface morphology of the silica spheres qualitatively, the samples were examined by scanning electron microscopy (SEM). The images in Figs. 2.1c, d, e and f suggest the topological differences between the coated surfaces. While the top surface of R_1 shows small patches of silica on the surface of the microsphere, the surface of R_2 shows a wrinkled surface texture caused by self- shadowing. The coated surfaces of particles S_1 and S_2 have in contrast a smoother topology.

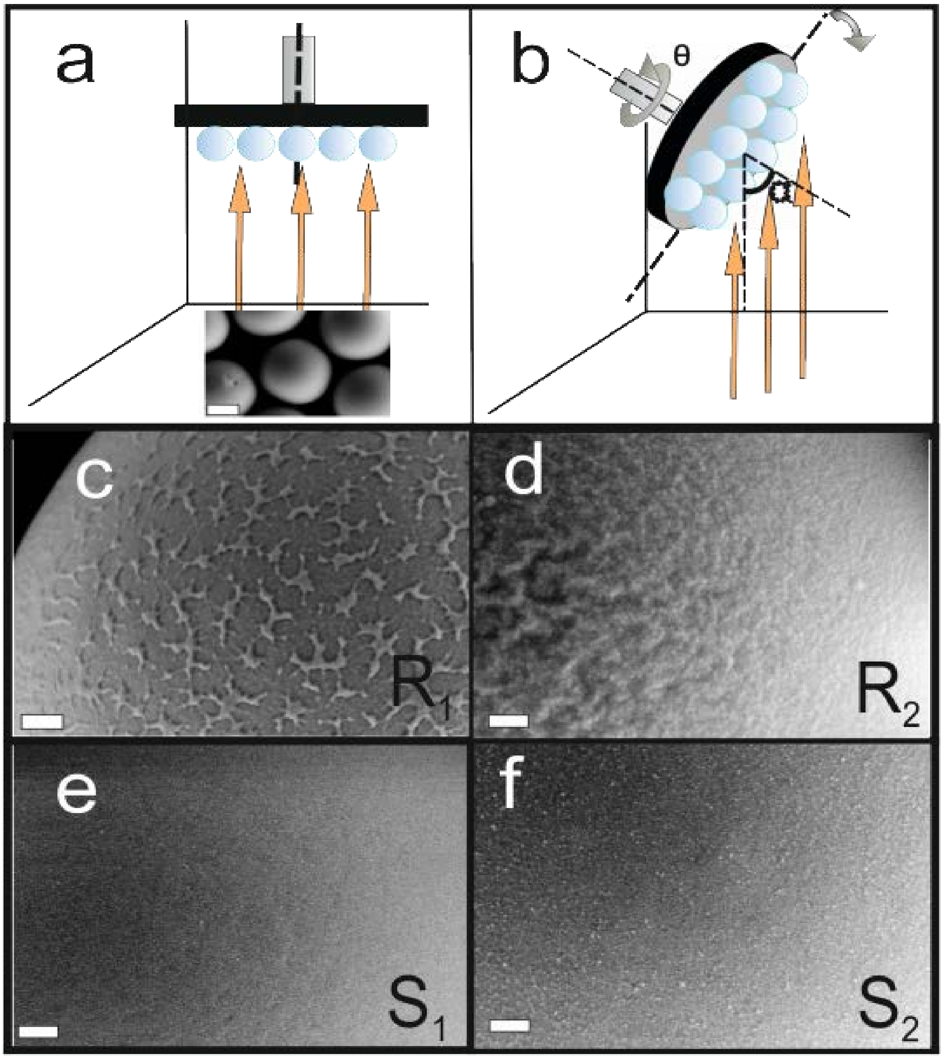

Figure 2.1: Schematic of the PVD fabrication method and images of Janus micromotor surfaces. a) Particles R_1, S_1 and S_2 were fabricated by keeping the substrate at fixed position. SiO_2 was initially deposited for R_1 and subsequently Ti and Pt were deposited. Orange arrows indicate the direction of the incoming vapor flux. b) Particle R_2 was fabricated by continuously rotating the substrate at 5 rpm and changing α from 87^0 to 0^0 while SiO2 was evaporated, while keeping the azimuthal angle θ constant. Subsequently, titanium and platinum was evaporated by keeping the substrate fixed at 0^0. The scale bar in the image 1a is 2 μm. c,d,e,f : Morphology of particles R1, R2, S1 and S2, respectively. The SEM images are captured by an SE2 detector. The scale bar for the images (c,d,e,f) is 200nm. Image taken from Ref 1.

2.3.2 Oxygen evolution test

To estimate the influence of the surface roughness on the catalytic activity of the Pt decomposition of H_2O_2, oxygen (O_2) evolution experiments were performed. In order to permit quantitative measurement, O_2 evolution tests on Si wafer-pieces (1 cm x 2cm) coated with smooth and rough Pt surfaces were performed, rather than surfaces covered with the silica particles. Silica particles do not form completely close-packed monolayers causing high variability in the particle covered surface and hence the total surface area. The smooth wafers were prepared by depositing Ti (7 nm) and Pt (20 nm) at 0^0 as shown in Figure 2.1a. The rough wafer was prepared by first depositing SiO_2 under glancing angle (as shown in Figure 2.1b) and subsequently coated with Ti (7 nm) followed by Pt (20 nm) at 0^0 The wafers therefore mimic the surface morphology of particles R_2 (rough) and particles S_1 and S_2 (smooth). The roughness for the particle R_1 is due to the surface curvature of the silica spheres and hence cannot be mimicked by a planar wafer.

After the deposition, each wafer piece was immersed in a 100 cm^3 Pyrex glass reactor containing 75 mL of 10% H_2O_2 at room temperature. The detailed experimental setup is shown in Figure 2.2.[21] The generation of O_2 started as soon as the wafer covered with catalytically-active Pt came into contact with the H_2O_2 solution. Oxygen produced by the decomposition of H_2O_2 escapes from the reactor via a silicone tube, which was then passed through a water bath at room temperature and collected in an inverted burette filled with water. The volume of the generated oxygen was deduced (at 298 K and 1 atm) from the water level change in the burette. The maximum rates of O_2 evolution were determined from the maximum slope of the experimentally determined O_2 generation curves. The maximum O_2 evolution rate for rough Pt was found to be 1.8 mmol $O_2\ cm^{-2}$ Pt min^{-1} and for smooth Pt was 0.6 mmol $O_2\ cm^{-2}$ Pt min^{-1}.

After verifying the higher catalytic rates for the rough surfaces, the different swimming characteristics of the Janus microparticles were investigated. The Janus particles were released from the wafer into deionized water by sonication and the suspension was washed and purified by centrifugation.

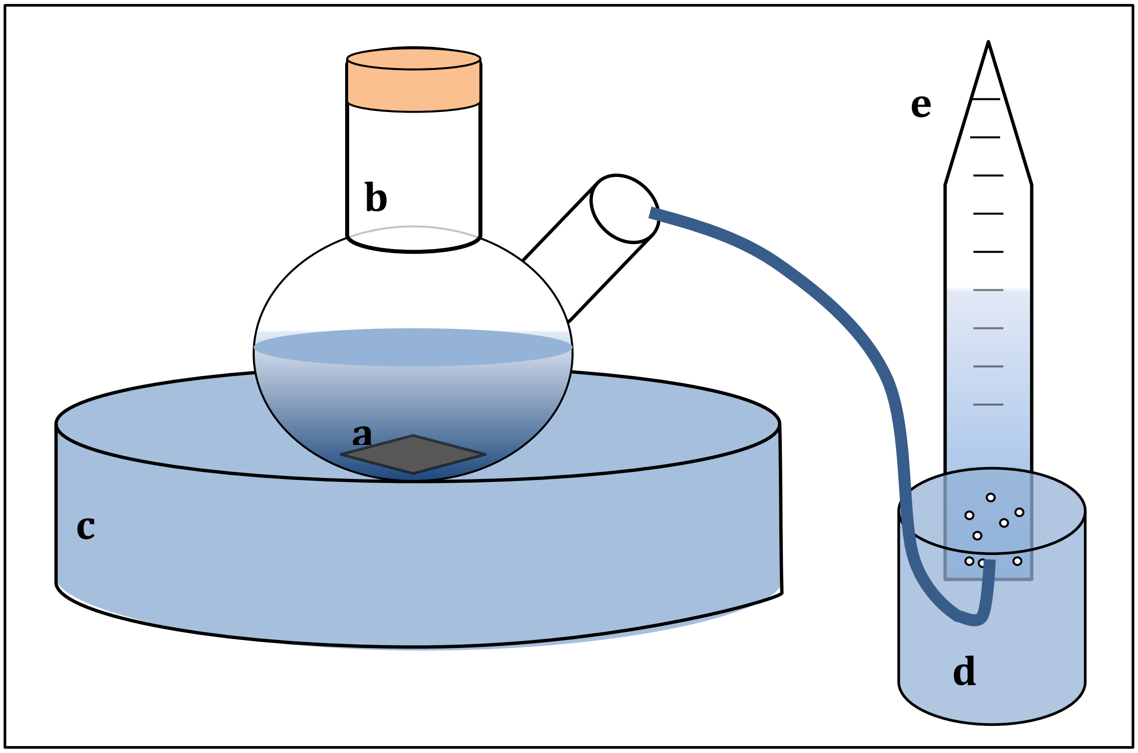

Figure 2.2: Apparatus for oxygen evolution test. a) Wafer immersed in a solution containing hydrogen peroxide b) Pyrex beaker c) Water bath d) Water filled beaker e)Inverted burette.

2.3.3 Swimming of rough and smooth Janus particles

After verifying the higher catalytic rates for the rough surfaces, the different swimming characteristics of the Janus microparticles fabricated with the rough surfaces were investigated. The Janus particles were released from the wafer into deionized water by sonication and the suspension was washed and purified by centrifugation. Aqueous suspensions of Janus micromotors were pipetted onto a silicon wafer piece, which was previously cleaned with O_2 plasma, and increasing amounts of H_2O_2 were added sequentially to obtain the desired H_2O_2 concentration. The videos of the self-propelled particles were recorded with a Leica optical microscope coupled to a CCD camera recording at 30 fps (Figure 2.4)The particles were tracked for 20 s. (Figures 2.5a and 2.5b) and the trajectories of 10 particles were combined to determine the mean squared displacement (MSD) (Figure 2.6) and speed (Figure 2.7).

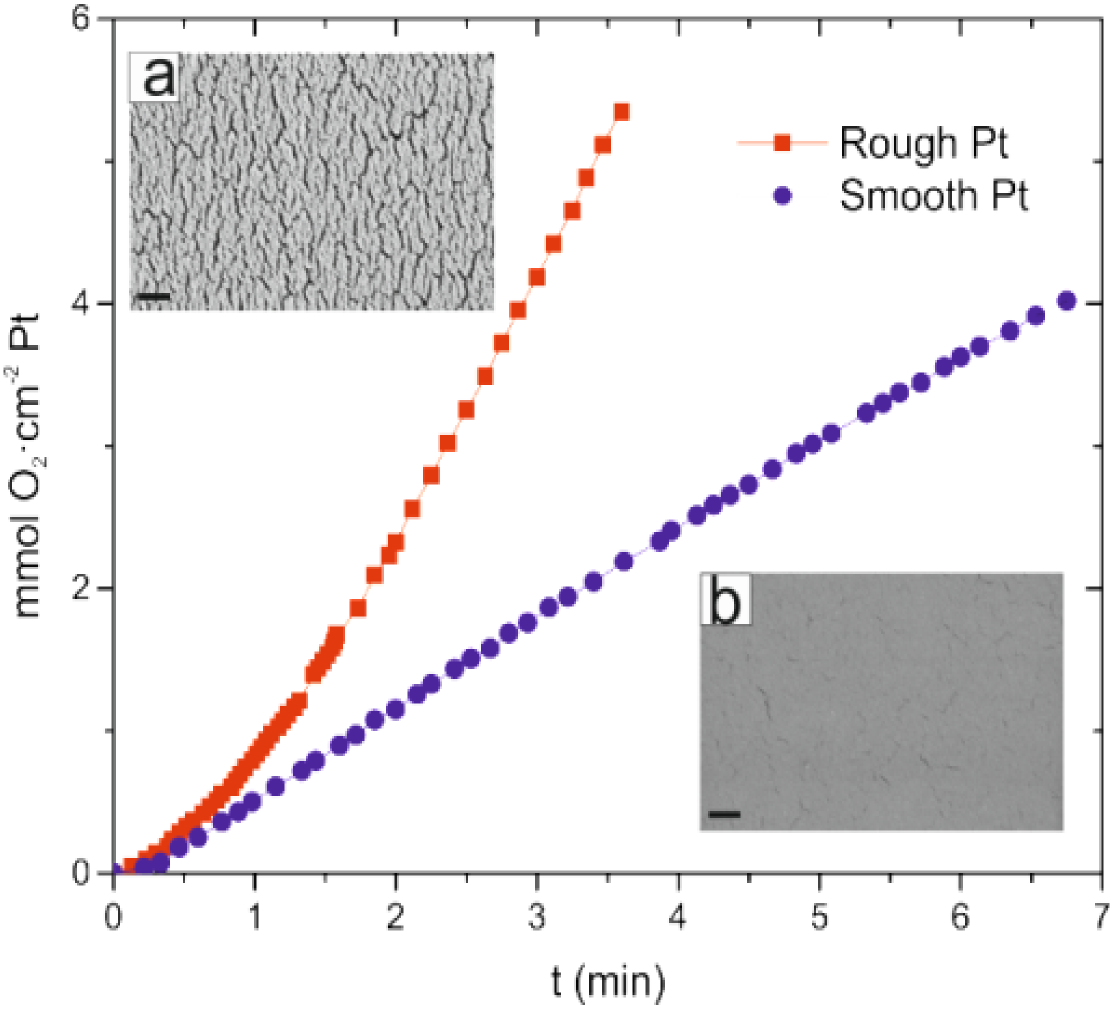

Figure 2.3: Evolution of O_2 from Pt layers (thickness 20 nm) deposited onto a Si wafer piece (1 cm × 2 cm) reacting with 10% H_2O_2.The upper left inset (a) shows a SEM image of rough Pt (as deposited by the deposition method used for particle R_2). The lower right inset (b) shows an SEM image of smooth Pt (as deposited by the deposition method used for particle S_1). The rough surface mimics the topology of particle R2 and the smooth surface that of particles S_1 and S_2. The scale bar is 200 nm. Image taken from Ref 1.

At low H_2O_2 concentration (0.5%) the speeds of all particles are low and within the experimental accuracy no differences can be observed. For higher concentrations the speed of the smooth particles S_1 and S_2 compare well to the literature value for 5 µm particles[21] and are comparable for all measured H_2O_2 concentrations. At 5% H_2O_2 the mean velocities between the smooth and the rough particles diverge with R_1 (9 µm s^{-1}) and R_2 (5 µm s^{-1}) showing, respectively a 3 and a 1.5 fold increase over smooth particles S_1 (3 µm s^{-1}) and S_2 (2.5 µm s^{-1}). At 15% H_2O_2 particle R_1 propels at a mean speed of 13 µm s^{-1} compared to the 3 µm s^{-1} of particle S_1.

The mean squared displacements (Δr^2) as a function of the time interval (Δt) were analyzed for individual concentrations to obtain the speed and diffusion constant. 10 random trajectory were selected and mean squared displacement calculated from each of them were averaged to obtain Δr^2 as a function of lagtime(Δt). For time scales shorter than the rotational diffusion time (τ_r), Δr^2 can be approximated as[1, 22] (see Appendix 2.6 for details)

$$\Delta r^2 = 4\, D_{diff} \Delta t + V^2\, \Delta t^2, \qquad (1)$$

which is fitted for Δt =2s ($\Delta t << \tau_r$ = 50 s), where D_{diff} is the short term diffusion coefficient and V is the propulsion speed . The diffusion constant and velocity can be calculated from fitting Eq.1 to the data.

The translational diffusivities of the smooth particles S_1 and S_2 remain close to the theoretically calculated value 0.1 µm^{2}s^{-1} for a 5µm particle

$$D_{diff} = k_B T / 6\pi\eta R \qquad , \qquad (2)$$

where k_B is the Boltzmann constant, T is Temperature, η is the viscosity and R is the radius of the particle).

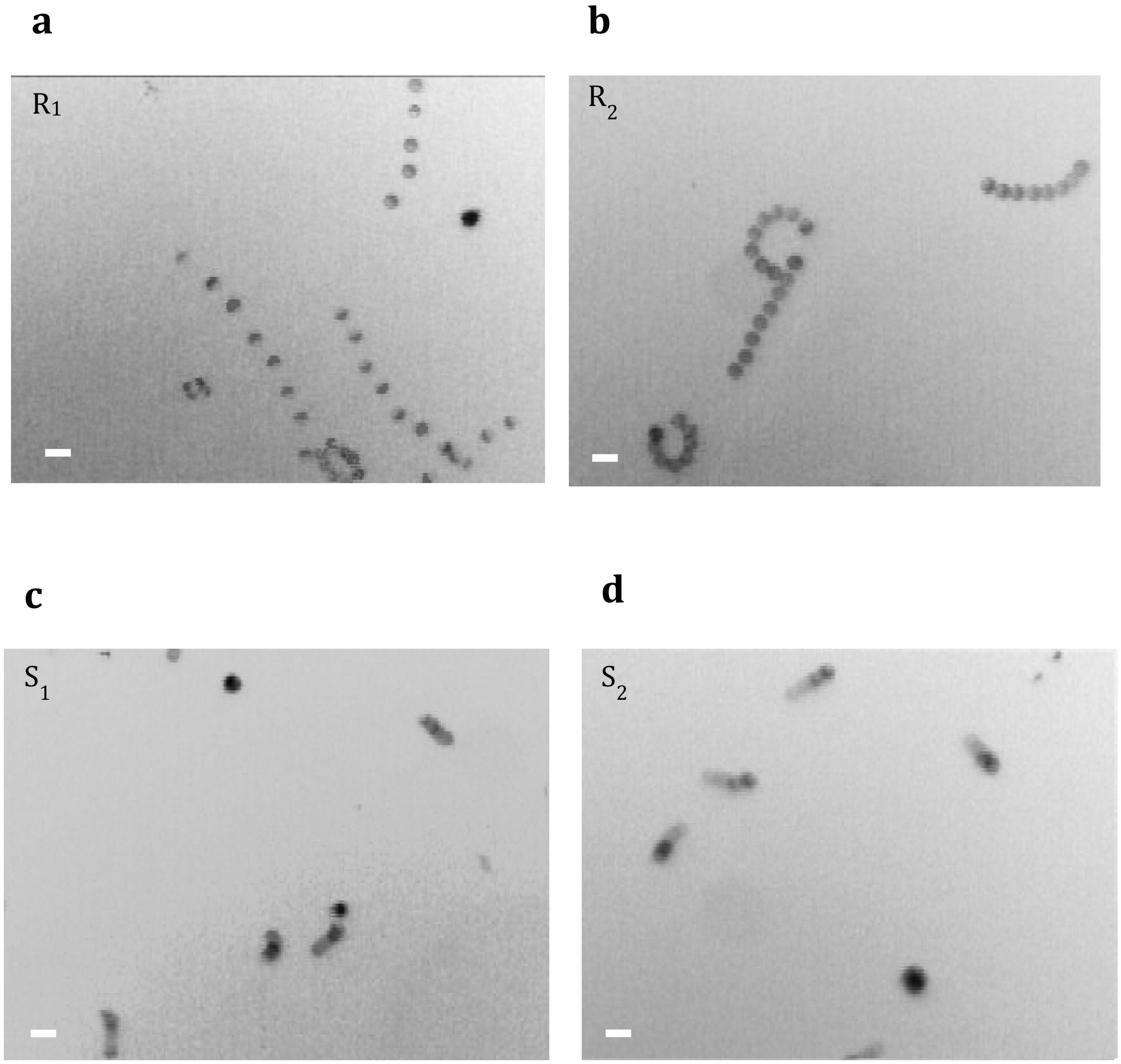

Figure 2.4: Overlay of movie frames separated by t=1s of Janus particles of type. a) R_1, b) R_2, c)S_1 and d) S_2 for 8s at 9% H_2O_2 concentration. Scale bar in the image is 10μm.

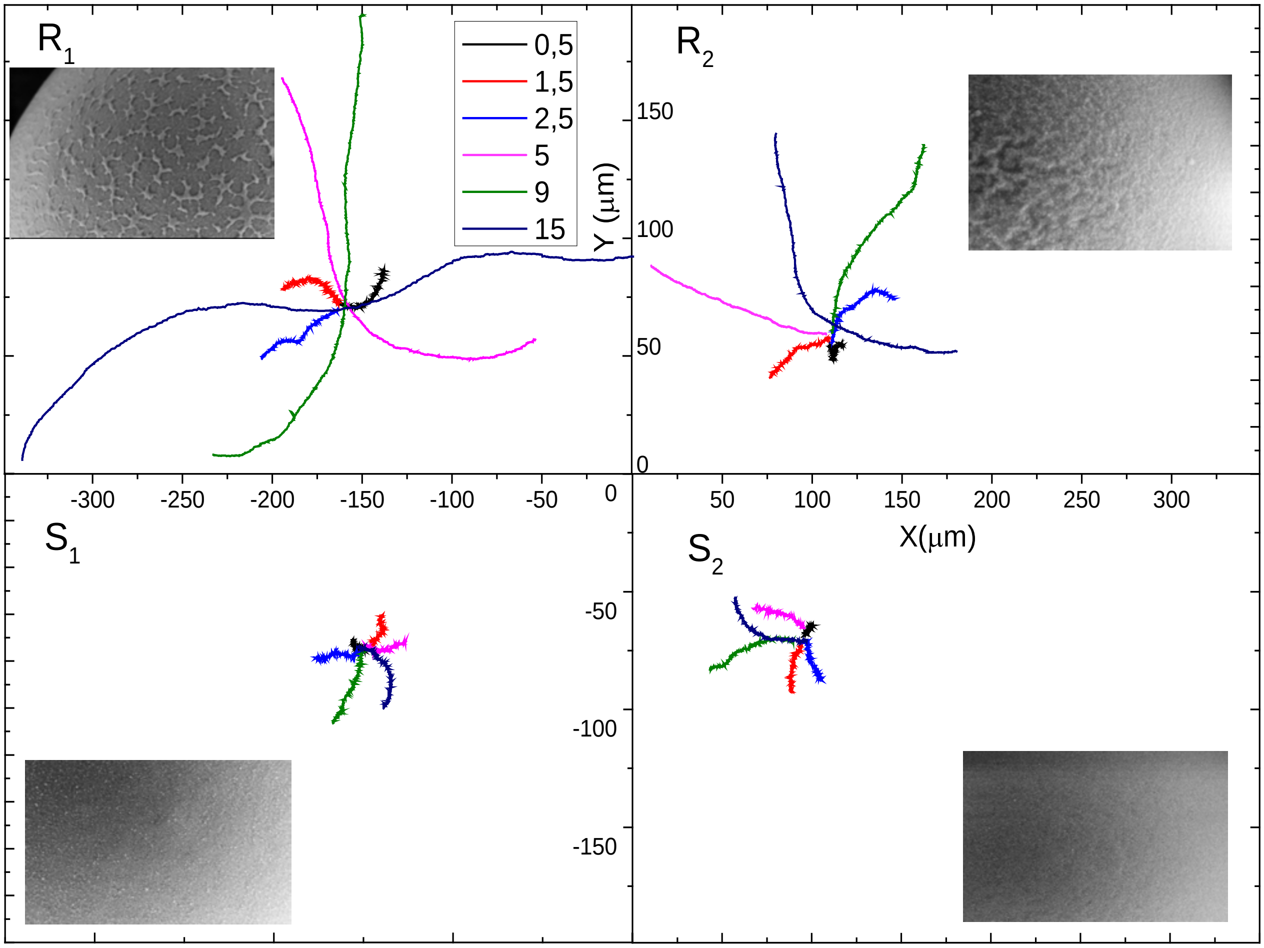

Figure 2.5 Examples of tracking trajectories of a single Janus particle of type R_1, R_2, S_1 and S_2 at different peroxide concentrations tracked for 20 s. Particle R1 in 15% H_2O_2 covers a correspondingly largest distance. Image taken from Ref 1.

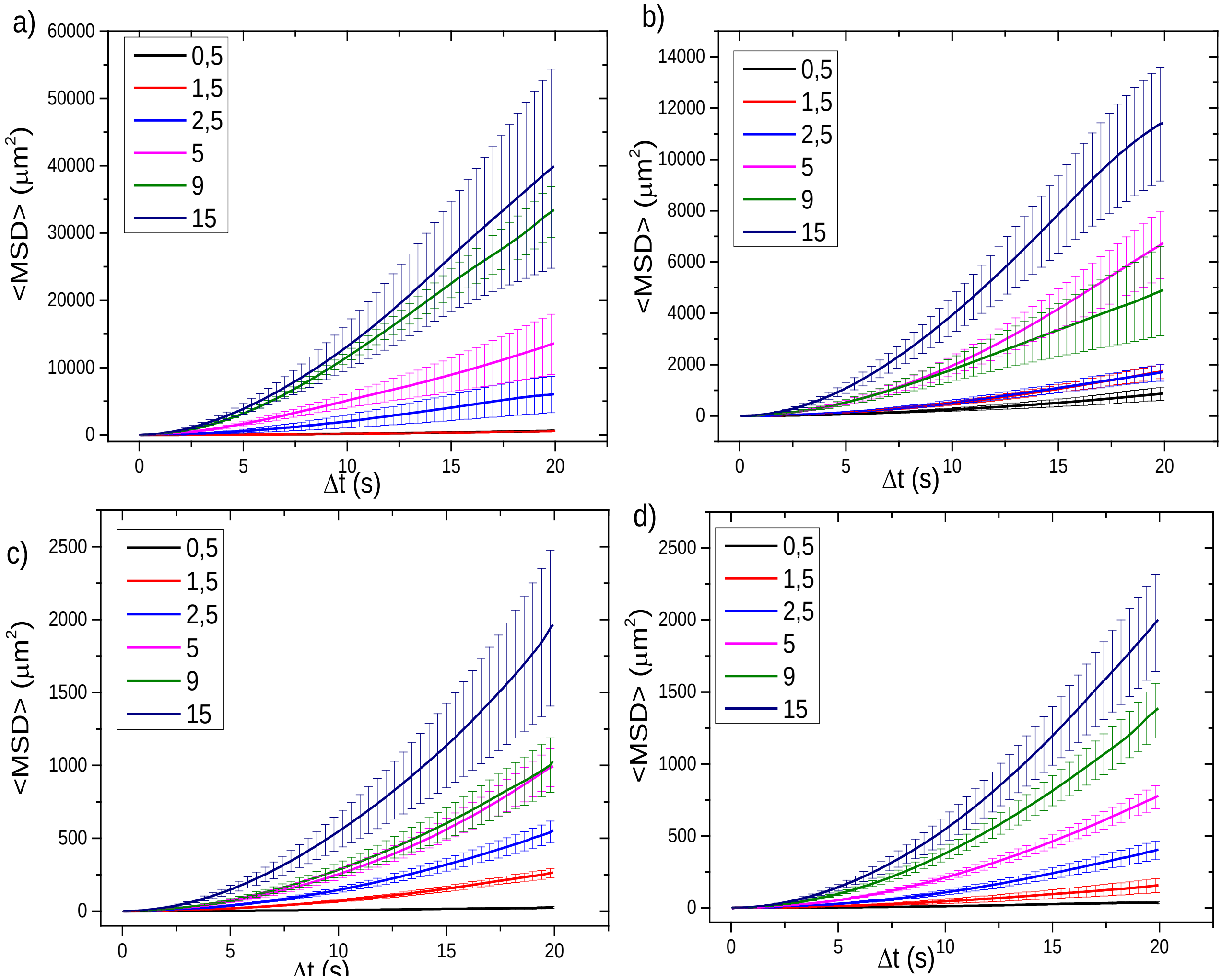

Figure 2.6: Mean Squared displacements of Janus motors at 0.5%, 1.5%, 2.5%, 5%, 9% and 15 % peroxide concentrations for a)R$_1$ b)R$_2$ c)S$_1$ and d)S$_2$ type motors. Image taken from Ref 1.

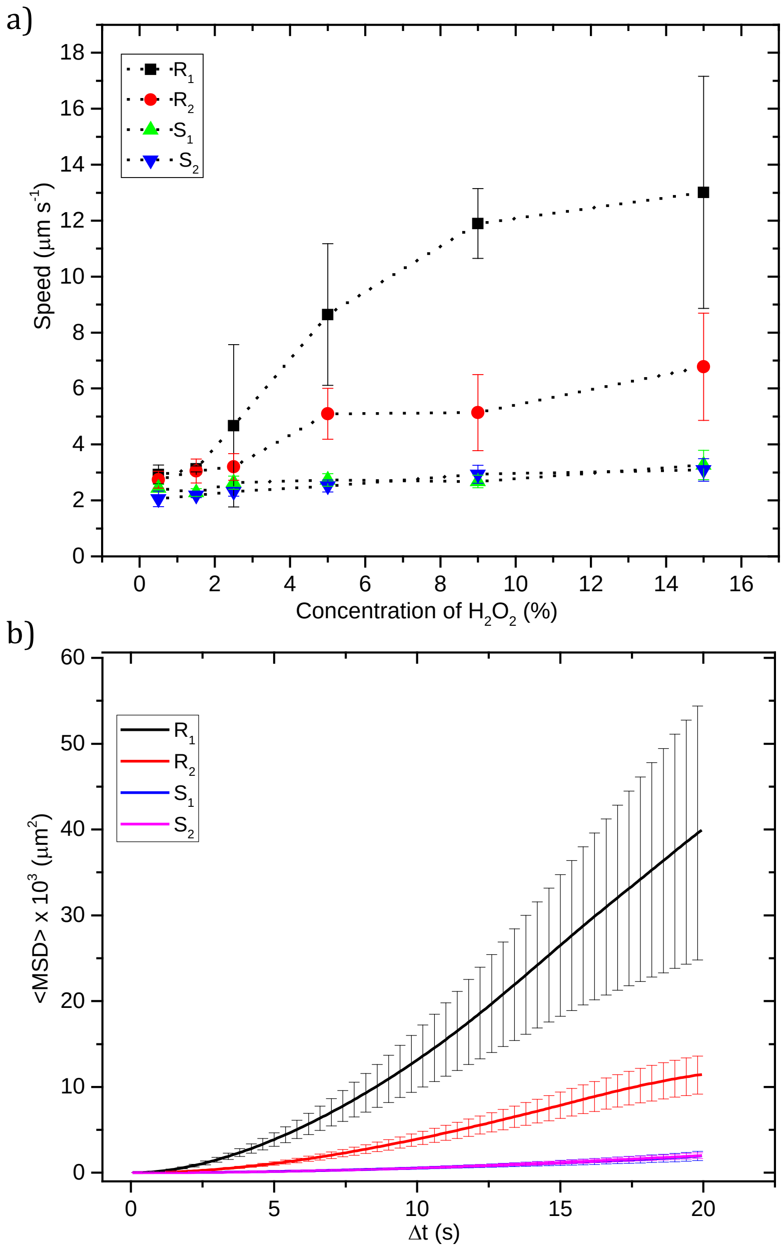

Figure 2.7 : a) Speed of Janus particles at different H_2O_2 concentrations. Smooth Particles S_1 and S_2 show a maximum mean speed of 3μm s^{-1} while particles R_1 and R_2 have a maximum mean speed of 7μm s^{-1} and 13 μm s^{-1}, respectively, for a 15% H_2O_2 concentration. Lines are plotted as guide to eye b) MSD plot with error bars for the 15 % H2O2 concentration for different particles. Image taken from Ref 1.

2.3.4 Theoretical fit to self-diffusiophoretic model

The self-diffusiophoretic speed can be expressed in terms of surface reaction rate k as[1]

$$V = \frac{3\pi}{2} k a \lambda^2, \tag{3}$$

where a is the hydrodynamic radius of the solute, k is the reaction rate and λ is the interaction zone between the solute and the particle.

The breakdown of H_2O_2 can be modeled as a two-step reaction with rate constants α_1 and α_2 as,[1, 21]

$$2\,H_2O_2 + Pt \xrightarrow{\alpha 1} Pt.(H_2O_2)_2 \xrightarrow{\alpha 2} 2H_2O + O_2 + Pt, \tag{4}$$

with,

$$k = \alpha_2 \frac{[H_2O_2]_{vol}}{[H_2O_2]_{vol} + \alpha_2/\alpha_1}, \tag{5}$$

The unknown reaction rate constants α_1 and α_2 as a function of the H_2O_2 concentration can be solved by fitting equation (3) and equation (5) to the speed of particles R_1, R_2, S_1 and S_2 in Figure 2.4a. Assuming, a = 1Å and λ = 5 Å,[1] and obtain the best fit line for Eqn. (3) to the speed data (see Fig 2.8). The experimentally determined reaction rates for different particles at 10% H_2O_2 concentrations are summarized in Table 1.

Table 1: Experimental reaction rates α_1 and α_2 for R_1, R_2, S_1 and S_2 Janus particles calculated by fitting Eqn. (3) and Eqn. (4) to the speed of the micromotors for 10% H_2O_2 concentration. a=1 Å and λ =5 Å was used to solve for α_1 and α_2.The reaction rate k calculated from Eqn. (4) at 10% H_2O_2 concentration to compare the surface reaction rate of the different micromotors.

	α_1 ($\mu m^{-2}s^{-1}$)	**α_2($\mu m^{-2}s^{-1}$)**	***k* at 10%($\mu m^{-2}s^{-1}$)**
R_1	2.49×10^{10}	1.6×10^{11}	9.75×10^{10}
R_2	2.42×10^{10}	6.40×10^{10}	5.06×10^{10}
S_1	1.19×10^{11}	2.57×10^{10}	2.51×10^{10}
S_2	9.32×10^{10}	2.50×10^{10}	2.43×10^{10}

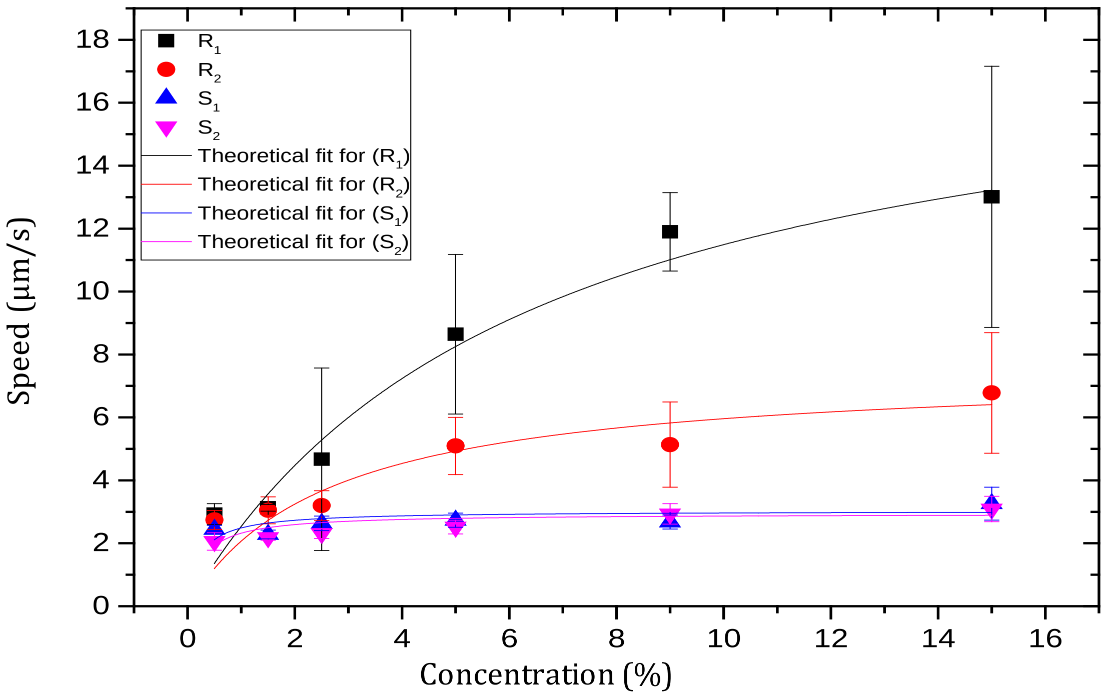

Figure 2.8 Theoretical fit of Equation 3 and Equation 5 to velocity of Particles R_1,R_2,S_1 and S_2 to obtain reaction rate constants k1 and k2 Image taken from Ref 1.

2.4 Discussion

Since the difference between the different particles is primarily due to a change in surface area, the change in reaction rate and speed can serve as an indirect measure for the surface area. Further, the speed as a function of the H_2O_2 concentration saturates at higher H_2O_2 concentrations.[1, 5] Therefore a concentration of 10% can be chosen to calculate the reaction rate and estimate the surface area enhancement effects from it. Furthermore, particle S_2 with a 80 nm Ti under-layer is of the same dimension as particles R_1 and R_2. Hence, it can be concluded that the increased reaction rate in particles R_1 and R_2 is caused by the surface roughness due to the nanoscale features introduced by the PVD process. From Figure 2.2, it is found that O_2 evolution for the rough Pt surface prepared using the deposition protocol for R_2 is three times higher than for the smooth surface prepared by the deposition protocol for S_1, suggesting that the surface area is also three times larger for the particle R_2

compared with the smooth particles S_1 and S_2. The reaction rate at 10% H_2O_2 concentration shows a similar increase of four and two times for particles R_1 and R_2, respectively, compared to particles S_1 and S_2. Further, from the Oxygen evolution test for smooth wafer surfaces, the rate of oxygen production was found to be 0.6 mmol cm^{-2} Pt min^{-1} , that translates to $6x10^{10}$ molecules $\mu m^{-2}s^{-1}$. This compares well with the reaction rate obtained for smooth surfaces (S_1 and S_2) which are both close to 2.5×10^{10} $\mu m^{-2}s^{-1}$. The surface coverage for smooth particles (S_1) can be calculated by $2\pi R^2 = 39$ μm^2. A direct comparison of the reaction rates yields the effective surface area for rough particles R_1 as 153 μm^2 and for particle R_2 as $(39 \times 5/2.5) = 78$ μm^2 . Quantitative direct comparisons are not possible since the geometry of the systems are not identical. The rates are expressed in units of $\mu m^{-2}s^{-1}$ to facilitate the comparison of surface reaction rates with turnover rates in homogeneous solutions. Thus, the increase in catalytic activity as observed *via* the speeds as well as the O_2 evolution tests on the rough surfaces are in agreement and of the same order of magnitude. This suggests that the increase in the effective surface area by the deposition of a SiO_2 under-layer applies both at the macroscopic wafer-scale and at the microscale of individual particles.

The difference in the speeds of R_1 and R_2 can be qualitatively explained by observing the morphology of the particles. While R_1 has random rough patches on its surface, R_2 has a more creased topology indicating denser growth of SiO_2 patches. Subsequently, the deposition of Ti and Pt under normal incidence yields larger coverage of the catalyst Pt on the patchy surface of R_1 than for R_2, since it is easier for the metal to diffuse uniformly on the patchy morphology of R_1, while self-shadowing only covers the tips of the structures in R_2. Hence, the effective area of the catalyst will be higher in R_1 than in R_2 which will lead to increased propulsion speed of R_1, as is experimentally observed

In conclusion, a fabrication scheme for making rough Pt surfaces on microsphere surfaces with PVD is presented. This results in a four-fold increase in the speed of the self-propelled particles compared to Janus particles that have a smooth Pt surface. Furthermore, the surface morphology of the rough spheres are characterized and theoretically estimated the increase of surface area of the particles fabricated by glancing angle growth. The simple fabrication strategy and a high increase in catalytic surface area and propulsion speed open up a new way to control the locomotion of micro-scale active swimmers. Further, this technique of introducing an oxide under-layer could be extended to electrochemistry to develop metal electrodes with higher surface area. It will be also interesting to apply these techniques to rolled-up tubular micromotors where the roughness may also facilitate the formation of bubbles.

2.5 References

1. Choudhury, U., Soler, L., G. Gibbs, J., Sanchez, S. & Fischer, P. Surface roughness-induced speed increase for active Janus micromotors. *Chem. Commun.* **51,** 8660–8663 (2015).
2. Howse, J. R. *et al.* Self-Motile Colloidal Particles: From Directed Propulsion to Random Walk. **99,** 048102 (2007).
3. Ebbens, S. J. & Howse, J. R. In pursuit of propulsion at the nanoscale. *Soft Matter* **6,** 726–738 (2010).
4. Sanchez, S., Soler, L. & Katuri, J. Chemically powered micro- and nanomotors. *Angew Chem Int Ed Engl* **54,** 1414–44 (2015).
5. Solovev, A. A., Mei, Y., Bermúdez Ureña, E., Huang, G. & Schmidt, O. G. Catalytic Microtubular Jet Engines Self-Propelled by Accumulated Gas Bubbles. *Small* **5,** 1688–1692 (2009).
6. Wang, J. Nanomachines: Fundamentals and Applications. (John Wiley & Sons, 2013).
7. Wang, W., Duan, W., Ahmed, S., Mallouk, T. E. & Sen, A. Small power: Autonomous nano- and micromotors propelled by self-generated gradients. *Nano Today* **8,** 531–554 (2013).
8. Lee, T.-C. *et al.* Self-Propelling Nanomotors in the Presence of Strong Brownian Forces. **14,** 2407–2412 (2014).
9. Loget, G., Roche, J. & Kuhn, A. True Bulk Synthesis of Janus Objects by Bipolar Electrochemistry. *Adv. Mater.* **24,** 5111–5116 (2012).
10. Sanchez, S. *et al.* The smallest man-made jet engine. *Chem. Rec.* **11,** 367–370 (2011).
11. Khim Chng, E. L., Zhao, G. & Pumera, M. Towards biocompatible nano/microscale machines: self-propelled catalytic nanomotors not exhibiting acute toxicity. *Nanoscale* **6,** 2119–2124 (2014).
12. Ibele, M., Mallouk, T. E. & Sen, A. Schooling Behavior of Light-Powered Autonomous Micromotors in Water. **48,** 3308–3312 (2009).
13. Carlsen, R. W., Edwards, M. R., Zhuang, J., Pacoret, C. & Sitti, M. Magnetic steering control of multi-cellular bio-hybrid microswimmers. *Lab. Chip* **14,** 3850–3859 (2014).
14. Zacharia, N. S., Sadeq, Z. S. & Ozin, G. A. Enhanced speed of bimetallic nanorod motors by surface roughening. *Chem. Commun.* 5856–5858 (2009). doi:Doi 10.1039/B911561g

15. Laocharoensuk, R., Burdick, J. & Wang, J. Carbon-Nanotube-Induced Acceleration of Catalytic Nanomotors. *ACS Nano* **2,** 1069–1075 (2008).
16. Wu, Z. *et al.* Self-Propelled Polymer-Based Multilayer Nanorockets for Transportation and Drug Release. **52,** 7000–7003 (2013).
17. Li, H. *et al.* A nanoporous oxide interlayer makes a better Pt catalyst on a metallic substrate: Nanoflowers on a nanotube bed. *Nano Res.* **7,** 1007–1017 (2014).
18. Chen, D. *et al.* Determining the Active Surface Area for Various Platinum Electrodes. *Electrocatalysis* **2,** 207–219 (2011).
19. Hawkeye, M. M. & Brett, M. J. Glancing angle deposition: Fabrication, properties, and applications of micro- and nanostructured thin films. *J. Vac. Sci. Technol. A* **25,** 1317–1335 (2007).
20. Mark, A. G., Gibbs, J. G., Lee, T.-C. & Fischer, P. Hybrid nanocolloids with programmed three-dimensional shape and material composition. *Nat. Mater.* **12,** 802–807 (2013).
21. Soler, L., Macanás, J., Muñoz, M. & Casado, J. Aluminum and aluminum alloys as sources of hydrogen for fuel cell applications. *J. Power Sources* **169,** 144–149 (2007).
22. Ebbens, S., Tu, M.-H., Howse, J. R. & Golestanian, R. Size dependence of the propulsion velocity for catalytic Janus-sphere swimmers. *Phys. Rev. E* **85,** 020401 (2012).

2.6 Appendix

2.6.1 Mean Squared Displacement of a spherical catalytic self-propelled colloid

Mean Squared displacement ($\Delta r^2(t)$) is a statistical measure of deviation of a particle's position from a reference position with respect to time

$$\Delta \mathrm{r}^2(\tau) = < [r(t+\tau) - r(t)]^2 >, \qquad \text{(A1)}$$

where, $r(t)$ is the position of the particle at time t, τ (or Δt) is the lag time between two particle position such that $\Delta r = r(t+\tau) - r(t)$. <..> is the time average of particle displacement over time t.

For a Brownian particle the mean squared displacement varies linearly with time

i.e. $$\Delta \mathrm{r}^2(\tau) = 4D\tau, \qquad \text{(A2)}$$

where D is the Brownian diffusion constant.

For self -propelled catalytically driven active colloid, with rotational diffusion time τ_{rot}, the mean squared displacement was derived by Howse *et al.* [1] as

$$\Delta \mathrm{r}^2(\tau) = 4D\tau + \frac{v^2 \tau_{\mathrm{rot}}^2}{2}\left(\frac{2\tau}{\tau_{rot}} + \mathrm{e}^{-2\tau/\tau_{\mathrm{rot}}} - 1\right), \qquad \text{(A3)}$$

For $\tau << \tau_{\mathrm{rot}}$, Equation (A3) can be simplified to

$$\Delta \mathrm{r}^2(\tau) = 4D_0\tau + v^2\tau^2 \qquad \text{(A4)}$$

Additional References

1. Howse, J. R. *et al.* Self-Motile Colloidal Particles: From Directed Propulsion to Random Walk. **99,** 048102 (2007).

3 : Active colloidal propulsion over a crystalline surface

This chapter is largely based on the journal paper "Active colloidal propulsion over a crystalline surface" Udit Choudhury, Arthur V Staube, Peer Fischer, John G. Gibbs and Felix Hofling in *New Journal of Phyics* **19,** 125010 (2017).[1]

The author performed the measurements, including video tracking and analysis. The author was assisted by Cornelia Miksh in preparing the surfaces. The theory underlying the experimental work of the author was developed by A.S. and F.H.

3.1 Introduction

The motion of self-propelled colloids differs from simple Brownian motion, because active particles interact hydrodynamically and chemically with each other and walls. For instance, the distribution of reaction products is affected by the presence of a wall, which breaks symmetry and directs the particle. It is therefore of interest to observe the dynamics of self-propelled particles near a complex boundary and the interaction with a more complicated topography is thus expected to play a major role to determine the dynamics of an active colloid. Here, a model system is considered and the dynamics of chemically self-propelled Janus colloids moving atop a two-dimensional crystalline surface is studied.

The surface is a hexagonally close-packed monolayer of colloidal particles of the same size as the mobile one. The dynamics of the self-propelled colloid reflects the competition between hindered diffusion due to the periodic surface and enhanced diffusion due to active motion. The propulsion strength determines which contribution dominates and can be systematically tuned by changing the concentration of a chemical fuel. The mean-square displacements (MSDs) obtained from the experiment exhibit enhanced diffusion at long lag times. The MSD describing the crossover from free Brownian motion at short times to active diffusion at long times are fitted to an approximate analytical model to describe the diffusion coefficients.

3.2 Motivation

The non-equilibrium behavior of active and passive particles ranging from microorganisms such as bacteria and artificial microswimmers to passive colloidal particles is an area of intense research in the last decade.[2–5] Biological microswimmers move by means of body shape changes driven by flagella and cilia. On the other hand, synthetic active particles are engineered to cause self-propulsion without any body shape changes.[6–9] Typically, they have a catalytic patch on their surface that can consume fuel present in the fluid.[10–15] This creates a local field gradient via a self-diffusiophoresis mechanism as has been discussed in Chapters 1 and 2 of this thesis.

Confining external potentials can substantially influence the dynamics of particles. For instance, the transport properties of passive particles changes when driven over one-and two-dimensional[16–23] spatially periodic or random potential landscapes[24–28] or in time-dependent potentials[29–32]. This manifests in control over speed of particles,[17,18,30,32] the strength of diffusion [16,21,22,25] and also in appearance of transport anomalies.[26–29,31] For active colloids, one also expects changes in their dynamics and indeed those confined by external potentials, behave similarly to passive particles with an elevated effective temperature[33,34] or subject to an effective potential.[35] Furthermore, simulation studies of microswimmers exploring a heterogeneous, random landscape suggest a rich phenomenology due to the interference of the landscape with the trajectory of the swimmer.[36,37]

Hydrodynamic coupling with a confining boundary can also significantly affect the motion of a particle moving through fluids. In case of a passive particle dragged or rotating near a plane wall, its mobility is significantly suppressed.[38] In case of active motion near plane,[39–47] the situation is, however, further complicated by swimmer–wall interaction forces.[5] For instance, the concentration of chemical fields near self-phoretic swimmers can be modified by the presence of a surface. Moreover, active colloids tend to accumulate at surfaces,[48] even in the absence of direct, e.g. attractive electrostatic interactions between the swimmer and the surface. In these cases a description based on an effective temperature is likely to be too simplistic.

In this study, the interplay of active propulsion and a periodic confining potential is investigated. Experimentally, active colloidal micro-spheres[11,49,50] are moving over a periodic surface realized as a hexagonal close-packed (HCP) monolayer of colloidal particles. The particles' activity is controlled by changing the concentration of a chemical fuel. Theoretically, the three-dimensional motion of an active colloid over the crystalline surface is treated as active Brownian motion in a two-dimensional energy landscape, while also accounting for the particles' rotational diffusion. An intricate interplay between confinement effects and active motion is observed which leads to non-trivial dependencies on the long-time diffusion coefficients and crossover timescales.

3.3 Results

3.3.1 Experimental setup

First, the experimental system and tuning of particle activity by changing the concentration of a chemical propellant[10,11,51] is described. An HCP monolayer consisting of spherical silica (SiO_2) microbeads (average diameter d = 2.07 μm with a coefficient of variation of 10%–15%, Bangs Laboratories) forms the periodic surface upon which the active colloids move. The lattice constant of the crystal is set by the particle diameter. The HCP monolayer was prepared with a Langmuir– Blodgett (LB) deposition technique[52] and covered an entire silicon wafer. A scanning electron microscope (SEM) image of the monolayer can be seen in Figure 3.1 b, and the actual topography of the surface is inferred from the atomic force microscope (AFM) image in Figure 3.1d. The silica microspheres were first functionalized with allyltrimethoxysilane, to facilitate LB deposition, then dispersed in chloroform. This colloidal suspension was then distributed over the air–water interface of an LB trough. A cleaned silicon wafer is dipped into the trough and, upon slowly pulling out the wafer, the monolayer is compressed to form a close-packed assembly. This process transfers the monolayer from the air–water interface to the silicon wafer. The wafer is then dried and treated with air plasma to remove any organic impurities before the experiments. While the LB technique yields large area HCP monolayers of silica beads, microscopic line defects can result from the lattice mismatch between adjacent self-assembled colloidal crystals. In order to ensure consistency of the underlying substrate topography, the lattice experiments were carried out on the same piece of wafer by varying the peroxide concentration for the same batch of particles. The active Janus colloids were fabricated by evaporating a 2 nm Cr adhesion layer followed by 5 nm of Pt onto microbeads of the same type as used for the monolayer; see Figure 3.1 a for an SEM image. The Janus spheres were then suspended into H_2O_2 and subsequently pipetted onto an HCP lattice surface (Figure 3.1c). The Pt on the Janus particle catalyzes the decomposition of hydrogen peroxide (H_2O_2) and gives rise to self-propulsion. The strength of the propulsion was altered by adding different concentrations of aqueous H_2O_2 to the colloidal suspension, covering concentrations between 0% and 6% (v/v). For each concentration, trajectories from 10 randomly chosen Janus particles were recorded for 100 s at a frame rate of 10 fps with a Zeiss AxioPhot microscope in reflection mode with a 20× objective coupled to a CCD camera (pixel size 5.5 μmx5.5μm, resolution 2048 × 1088).

3.3.2 Data Analysis

Time-averaged mean-square displacements (MSDs) of 10 trajectories for each H_2O_2 concentration were computed, and by averaging the MSDs at each lag time the averaged MSD and its standard error was obtained. Data fitting was performed with the software OriginLab (OriginLab Corp., Northampton, MA) using a Levenberg–Marquadt iteration algorithm. Due to the linearly spaced time grid, the data points accumulate in the double-logarithmic representation at large times. To account for the different density of data points at short and long lag times on logarithmic scales, a 1/t weighting factor was used. The fits to eqns. (2) and (4), respectively, were then performed simultaneously for all 10 data sets of each concentration such that the different scatter of the data points enters the error estimate of the fit parameters. The free diffusivity D_0 was fixed initially to its value for the passive particle moving over a smooth surface and was slightly adjusted afterwards for each H_2O_2 concentration to obtain the best match with the averaged MSD curves.

3.3.3 Height of the potential barrier

Under gravity the Janus particles settle onto the substrate; once settled and in the absence of any fuel, Brownian motion leads to effectively two-dimensional diffusion in the gravitational potential imposed by the surface. The potential exhibits a periodic, hexagonal structure of potential wells with adjacent energy minima separated by a distance $d/\sqrt{3}$. In the presence of fuel a series of ‘hops’ are observed between adjacent wells (energy minima), or in analogy to surface diffusion, adjacent ‘adsorption sites’. Figure 3.2a schematically demonstrates a single hop from one minimum to an adjacent one. A successful hop requires the Janus particle to overcome an energy barrier as depicted in Figure 3.2b . The gravitational potential *U(x)* = Δ*mgz(x)* is given by

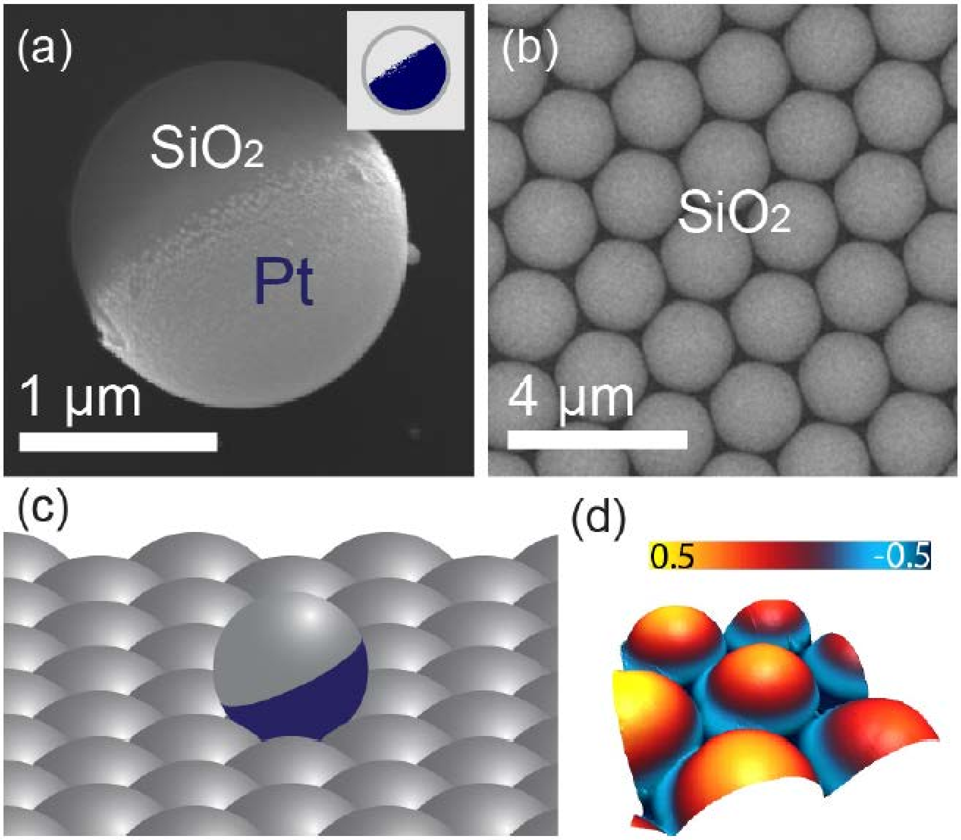

Figure 3.1 Experimental setup (a) Scanning electron microscope (SEM) image of a single half-coated Janus particle; inset: dark-blue shows the location of the Pt cap. (b) Top-view SEM image of an HCP monolayer of SiO2microbeads. (c) An oblique-view schematic of Janus particle situated on the periodic, two-dimensional lattice, giving a sense of the corrugated, periodic morphology of the surface. (d) Atomic force microscope (AFM) image exhibiting the topography of the surface, color indicates the height in µm. Image taken from Ref 1.

the buoyant mass Δm of the Janus particle, the acceleration g due to gravity, and the height profile $z(x)$ at the two-dimensional position x.

The energy barrier between adjacent potential minima is thus $E_a = \Delta m g \Delta z$, where Δz follows from elementary geometry as shown in Figure 3.2c for the configurations of maximal and minimal height. At the barrier maximum (left column of Figure 3.2 c), the centers of two substrate particles and the mobile one form an equilateral triangle. The Janus particle is thus elevated by $z_{max} = \sqrt{3}d/2$ above the centers of the substrate particles. If the Janus particle is found in a potential minimum, the centers of three substrate particles and the mobile one form a regular tetrahedron, thus $z_{min} = \sqrt{6}d/3$. For a successful hop, the particles must overcome a geometric barrier of height $\Delta z = z_{max} - z_{min} \approx d/20$, which evaluates to $\Delta z \approx 100$ nm for $d = 2$ µm. This is consistent with the surface's height profile obtained from AFM as shown in Figure 3.1d.

The second ingredient to the energy barrier E_a is the total force on the Janus particle, which results from the competition of gravity and buoyancy, i.e. the energy barrier is also a function of the material from which the Janus particle is made. Let us first consider a silica sphere without a metal coating. Then the buoyant mass is $\Delta m = \Delta\rho V_{SiO_2}$, where $\Delta\rho = \rho_{SiO_2} - \rho_{H_2O}$ is the difference in density between SiO_2 and H_2O, and $V_{SiO_2} = (4/3)\pi a^3$ is the volume of the fluid displaced by the particle of radius $a = d/2$. For a bare SiO_2 bead of 2 µm diameter, this yields $E_a = 1.7 k_B T$.

In the case of the Janus particle, the asymmetric distribution of the metallic coating needs to be taken into account. Even though the volume of the cap is small in comparison to that of the bead, it has a significant effect on E_a due to the higher density of Pt. Following Ref. [53] [53], the hemispherical cap was modeled as ellipsoidal in shape; the thickness Δa of the deposited metal is largest at the top of the sphere and tapers to zero at the equator. This assumption is justified from the deposition process, which delivers the atoms in the vapor plume ballistically to the top surface of the sphere while the sides along the equator remain shadowed and consequently have a thinner metal coating. The volume of the cap can be estimated as $V_{Pt} = [4/3\pi a^2(a + \Delta a) - 4/3\pi a^3]/2 = 2/3\pi a^2 \Delta a$ and with this, the buoyant mass of the Janus particle is $\Delta m = (\rho_{SiO_2} - \rho_{H_2O})\, V_{SiO_2} - (\rho_{Pt} - \rho_{H_2O})\, V_{Pt}$. Adopting a value of Δa =

5 nm as the maximal thickness of the Pt cap and using ρ_{Pt} =21.4 g/cm^3, one can estimate E_a = $\Delta m g \Delta z \approx 2.1 k_B T$ for the energy barrier of the Janus particle including the metal cap.

3.3.4 Distance from top of surface

For the Janus particle moving passively over a smooth plane, the translational diffusion constant D_0 is 0.13 μm^2/s $^{-1}$, which implies a translational (hereafter indicated by the subscript 'T') hydrodynamic friction of $\zeta_T = k_B T / D_0$=3.2x10^{-8}Pa-s-m at T=298K. As expected, the presence of a surface increases the hydrodynamic friction compared to unbounded motion: comparing with the Stokes friction $\zeta_T^{St} = 6\pi\eta a \approx$ 1.74x10^{-8} Pa-s-m in H_2O (η=0.89 mPa-s) , one finds $\zeta_T \approx 1.8\ \zeta_T^{St}$. For a planar surface, the friction coefficient ζ_T of a sphere of radius a dragged parallel to the surface at a distance h from the sphere center obeys Faxén's famous result[38,54]

$$\frac{\zeta_T^{St}}{\zeta_T} \approx 1 - \frac{9}{16}\frac{a}{h} + \frac{1}{8}\left(\frac{a}{h}\right)^3 - \frac{45}{256}\left(\frac{a}{h}\right)^4 - \frac{1}{16}\left(\frac{a}{h}\right)^5, a \ll h, \tag{1}$$

Inserting the above experimental value for ζ_T and solving for h with a = 1 μm , h ≈ 1.3 μm leaving a gap of h-a ≈ 0.3 μm between the two surfaces of the Janus particle and the planar substrate. Note that Faxén's calculation relies on a far-field expansion of the flowfield and is justified only for small ratios a/h. As can be seen *a posteriori*, a/h≈0.8, implying slow convergence. Indeed, truncating after the 3rd order in a/h yields an unphysical h<a , which is fixed by the 4th order term. The 5th order term contributes merely a relative correction of 2%, which suggests convergence of the series. Furthermore, this far-field estimate is compared with the predictions from lubrication theory[54] and a rigorous series expansion[55] accurate at all separations of the particle and the surface, including the singular limit of close approach. This cross-check shows that the present experimental situation is still outside the lubrication regime and equation (1) should provide very good estimates of the friction coefficient and the elevation h. In the following, it is assumed that the translational friction ζ_T does not change appreciably for the range of H_2O_2 concentrations used, although it may be modified for active motion due to altered boundary conditions at the colloid's surface.

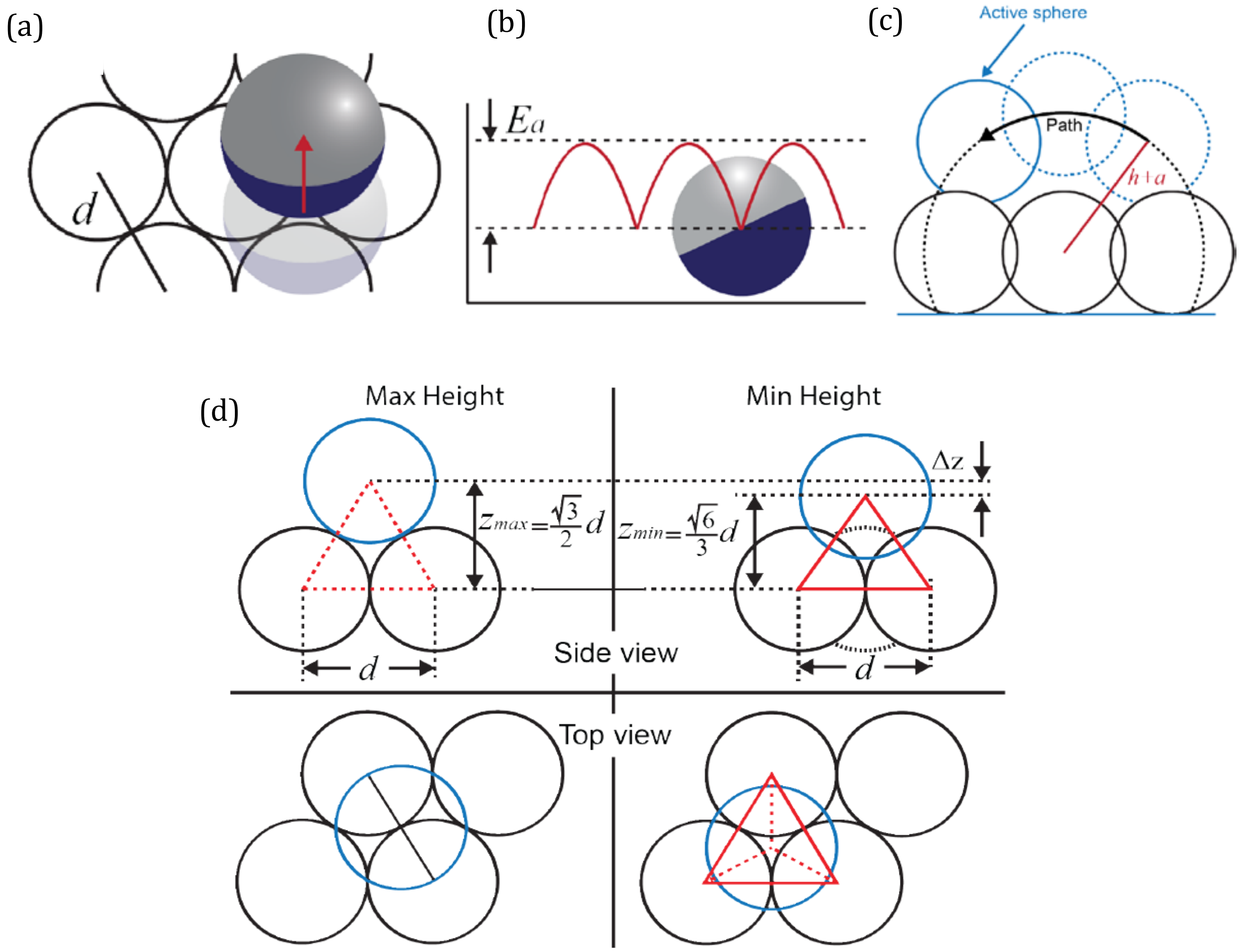

Figure 3.2 Topology of crystalline substrate. (a) Top-view schematic of a single hop from one potential well to an adjacent one. (b) Side-view schematic of an active particle situated in an energy minimum. (c) A cross-sectional representation of the Janus sphere traversing the energy barrier as it moves from one adsorption site to an adjacent one. The center of the sphere follows the black curved arrow, which is a section of a circle of radius $h+a$, where h is the "elevation" above the crystalline surface. The maximum position corresponds to the dashed light-blue circle in the top-center portion of the figure. (d) Geometry of the barrier between adjacent potential wells due to the HCP lattice substrate. Top row: side-view of the mobile particle (blue circle) at its highest and lowest out-of-plane positions, *z*max and *z*min on the left and right columns, respectively. Bottom row: corresponding top-views, representing the in-plane positions of the mobile particle with respect to the location of the substrate particles (black circles).Image taken from Ref. 1

3.3.5 Active motion on a plane and enhanced diffusion

In order to control the activity, the H_2O_2 concentration dependence of active motion as previously seen in catalytic chemical self-propulsion is utilized. On a flat, planar surface, the MSD after a lag time t is given by [11]

$$\Delta R_{a,p}^2(t) = 4\left(D_0 + \frac{v^2\tau_{\mathrm{rot}}}{2}\right)t + 2v^2\tau_{\mathrm{rot}}^2\left(\mathrm{e}^{-t/\tau_{\mathrm{rot}}} - 1\right), \qquad (2)$$

which follows upon assuming independence of translational diffusion of the colloid center and rotational diffusion of the Pt cap orientation; here D_0 is the diffusion coefficient for passive Brownian motion over a smooth plane, v the root-mean-square propulsion velocity in the plane, and t_{rot} the persistence time of the propulsion direction. The subscripts '*a*', *o*' are used to distinguish between the active and passive motion and '*p*' refers to the case of planar surface. Qualitatively, equation (2) implies that the active colloid undergoes passive diffusion for $t \ll \tau_0 = 4D_0/v^2$; ballistic motion for $\tau_0 \ll t \ll \tau_{rot}$, and enhanced diffusion for $t \gg \tau_{\mathrm{rot}}$. In the latter regime, the MSD grows linearly with time with an increased diffusion coefficient $D_{a,p} = D_0 + v^2\tau_{\mathrm{rot}}/2$. Thus at long times, the motion of the active particle displays an enhanced diffusion relative to the motion of the passive particle ($v = 0$).

Figure 3.3 shows the experimental results for active motion on a smooth, planar surface for the six H_2O_2 concentrations investigated, from which the enhanced diffusion was obtained. The solid curves in Figure 3.3 are fits to equation (2), following the procedure in section 1.3.2, with the obtained parameters given in Table 3.1. In the inset of Figure 3.3, the MSD is rectified by dividing by the time lag t. This way, the crossover from Brownian diffusion D_0 at short times to enhanced diffusion $D_{a,p}$ at long times can be inferred more easily, and this representation serves also as a sensitive test of the fit quality. The short-time diffusivity D_0 was varied between 0.14 $\mu m^2/s$ and 0.18 $\mu m^2/s$ to obtain the best match with the averaged MSD curves. The small variability of the background diffusivity may be attributed to the sparseness of data points at short timescales, but it may also reflect possibly altered boundary conditions at the surface due to the catalytic reaction. The propulsion velocity v measured this way (Table 3.1) increases monotonically with the H_2O_2 concentration c.

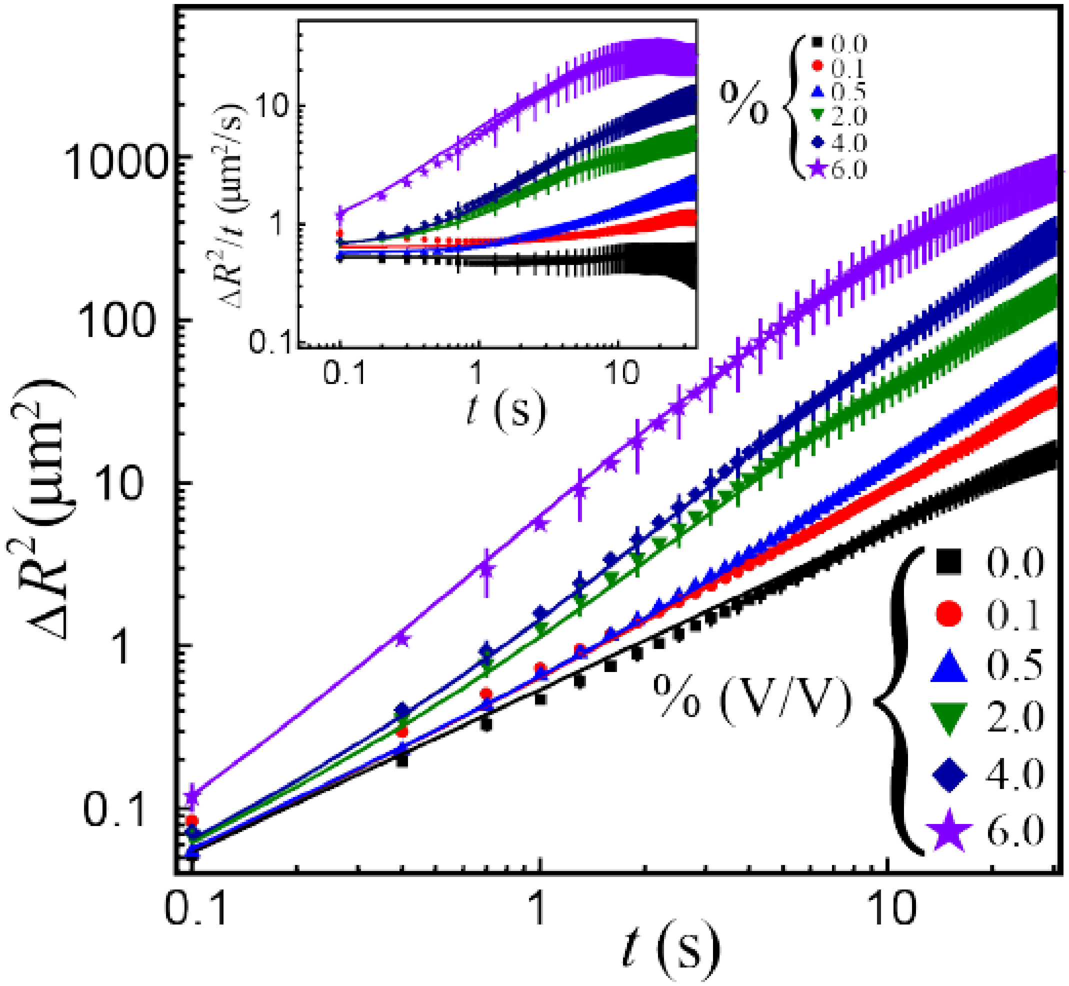

Figure 3.3: Experimental MSDs of the active particles moving over a planar surface for six H_2O_2 concentrations. Solid lines are fits to eq. (2). Inset: rectification plot of the same data showing $\Delta R_{a,p}^2(t)/t$ vs. t in order to more clearly expose the crossover from Brownian to enhanced diffusion. It also serves as a test of the fit quality. between adjacent energy minima, or in analogy to surface diffusion, adjacent 'adsorption sites'. Image taken from Ref 1.

Table 3.1. Parameters obtained from fitting eq. (2) to the MSD data for active motion atop a planar substrate, shown in Figure 3.3. The long-time diffusion coefficient $D_{\mathrm{a,p}}$ was calculated from $D_{\mathrm{a,p}} = D_0 + v^2\tau_{\mathrm{rot}}/2$. The indicated uncertainties are standard errors of mean as obtained from the fitting procedure.

c(%v/v)	**$D_{0,p}$(μm^2/s)**	**$D_{a,p}$(μm^2/s)**	**τ_{rot}(s)**	**v(μm/s)**
0	0.13	$0.13_{\pm0.0}$		0
0.1	0.16	$0.35_{\pm0.1}$	$11_{\pm3}$	$0.18_{\pm0.0}$
0.5	0.14	$0.7_{\pm0.2}$	$12_{\pm3}$	$0.30_{\pm0.0}$
2	0.16	$1.4_{\pm0.5}$	$4.2_{\pm0.7}$	$0.77_{\pm0.0}$
4	0.15	$3.6_{\pm0.8}$	$7.9_{\pm1.2}$	$0.93_{\pm0.0}$
6	0.14	$8.0_{\pm1.6}$	$2.3_{\pm0.6}$	$2.6_{\pm0.3}$

The long-time diffusivity $D_{\mathrm{a,p}}$ also grows progressively with an increase in c and is enhanced over D_0 for all concentrations $c>0$ studied, in accordance with equation (2). Further, since v and $D_{a,p}$ for c = 6% v/v are significantly larger than the corresponding values for c=4% v/v, suggesting that additional effects become important for the propulsion mechanism at this high concentration. Finally, a large, non-monotonic variation of t_{rot} is observed signifying that the rotational motion is non-trivially altered by the activity. This may be attributed to imperfections in the Janus particle, causing deviations from axisymmetric symmetry and thus the possibility of a residual active angular velocity on the particle.

3.3.6 Active motion on crystalline surface

Figure 3.4a shows the averaged MSD data of Janus particles being actively propelled atop the crystalline surface for six H_2O_2 concentrations. As expected, increasing the H_2O_2 concentration leads to higher observed propulsion speeds and higher long-time diffusion. The latter can be directly inferred from the rectification $\Delta R^2_{a,c}(t)/t$ displayed in the inset of Figure 3.4a. The data suggest further a monotonic dependence on time, either decreasing or increasing depending on the concentration of fuel, which can be interpreted as a competition of the suppression of diffusivity due to the potential landscape with the enhancement due to active motion. The mean squared displacement of an active colloid on crystalline surface can be derived as (See Appendix 3.6)

$$\Delta R_{a,c}^2 \quad = 4\left(D_{0,\mathrm{p}} - \Delta D_c + \frac{v^2\tau_{\mathrm{rot}}}{2}\right)t - 4\,\Delta D_c\,\tau_{\mathrm{s}}\left(\mathrm{e}^{-t/\tau_c} - 1\right) + 2v^2\tau_{\mathrm{rot}}^2\left(\mathrm{e}^{-t/\tau_{\mathrm{rot}}} - 1\right). \qquad (3)$$

Fitting Eqn.(3) to the experimental MSD data would, in principle, provide an estimate for the parameters ΔD_c, v, τ_c, τ_{rot}. Following this approach, it turned out all of the parameters depend on the H_2O_2 concentration. Specifically, fixing the values of v and τ_{rot} to those from the experiments with the planar surface does not produce satisfying fits. Further, the four-parameter fits suggest similar values for τ_c and τ_{rot}, which motivated us to merge both timescales into a single parameter, τ. This is consistent with the absence of any minimum or maximum at intermediate lag times in the data for $\Delta R_{a,c}^2(t)/t$, which would be supported by Eqn.(3). However, $\tau_c \approx \tau_{rot}$ implies that the parameters ΔD_c and v are no longer independent, merely the combination $\Delta D = \Delta D_c - v^2\tau/2$ can be obtained. Thus, Eqn.(3) reduces to a simplistic, effective model of the MSD of a self-propelled particle atop a periodic surface,

$$\Delta R_{a,c}^2(t) \approx 4D_{a,c}t + 4(D_{a,c} - D_0)\,\tau\left(\mathrm{e}^{-\frac{t}{\tau}} - 1\right). \qquad (4)$$

By construction, this result has the same form as Eqn.(2) but the interpretation of the parameters is different in each case. For long times ($t >> \tau_c,, \tau_{rot}$), the MSD increases linearly, and the combination $D_{a,c} = D_0 - \Delta D_c - D + v^2\tau/2$ is the long-time diffusion coefficient on the crystalline surface. Eqn.(4) is used to fit the MSD data with D_0, $D_{a,c}$, and τ as free parameters. The results obtained for each concentration are given in Table 3.2 and the fits shown as solid curves in Figure 3.4 provide a consistent description of the data. A slight variability of D_0 is obtained and a strong dependence of τ on the H_2O_2 concentration.

The enhancement of the long-time diffusivity $D_{a,c}$ with increasing H_2O_2 concentration is much less pronounced compared to the case of a planar surface ($D_{a,p}$ in Table 3.1), which is a direct consequence of the trapping potential.

Figure 3.4b shows effective diffusion coefficients on the crystalline and plane surfaces, $D_{\mathrm{a,c}}$ and $D_{\mathrm{a,p}}$, respectively, against the fuel concentration c. Strong deviations from one another at high concentrations are observed. At low concentrations of fuel, the particles move over the periodic surface by a hopping mechanism, probing the shape of the potential wells. Essentially, it appears there is a transition from a periodic landscape of high potential barriers at low concentration to a free particle system without any barrier, and therefore, the motion is similar to what is seen for a free active particle on a planar surface, but with a reduced diffusion coefficient. The experimental values for the ratio $D_{a,c}$ to $D_{a,p}$ vary between 0.7 and 0.19 and suggest a decrease towards higher concentrations c.

Table 3.2. Parameters estimates from fitting eq. (4) to the MSD data shown in Figure 3.4a $D_{0,\mathrm{p}}$ is the Brownian diffusion coefficient at short times, $D_{\mathrm{a,c}}$ is the long-time diffusion coefficient of the self-propelled particle moving atop the crystalline surface, and $\tau \approx \tau_{\mathrm{c}} \approx \tau_{\mathrm{rot}}$ is a single crossover timescale.

c(%v/v)	**$D_{0,p}$(μm²/s)**	**$D_{a,c}$(μm²/s)**	**τ (s)**	**$D_{a,c}/D_{a,p}$**
0	$0.14_{\pm 0.0}$	$0.05_{\pm 0.0}$	$0.4_{\pm 0.0}$	0.38
0.1	$0.17_{\pm 0.0}$	$0.25_{\pm 0.0}$	$6.3_{\pm 2.9}$	0.71
0.5	$0.18_{\pm 0.0}$	$0.29_{\pm 0.0}$	$5.4_{\pm 2.2}$	0.41
2	$0.14_{\pm 0.0}$	$0.56_{\pm 0.0}$	$2.3_{\pm 0.4}$	0.4
4	$0.14_{\pm 0.0}$	$0.8_{\pm 0.5}$	$3.2_{\pm 0.1}$	0.22
6	$0.14_{\pm 0.0}$	$1.5_{\pm 0.4}$	$1.5_{\pm 0.4}$	0.19

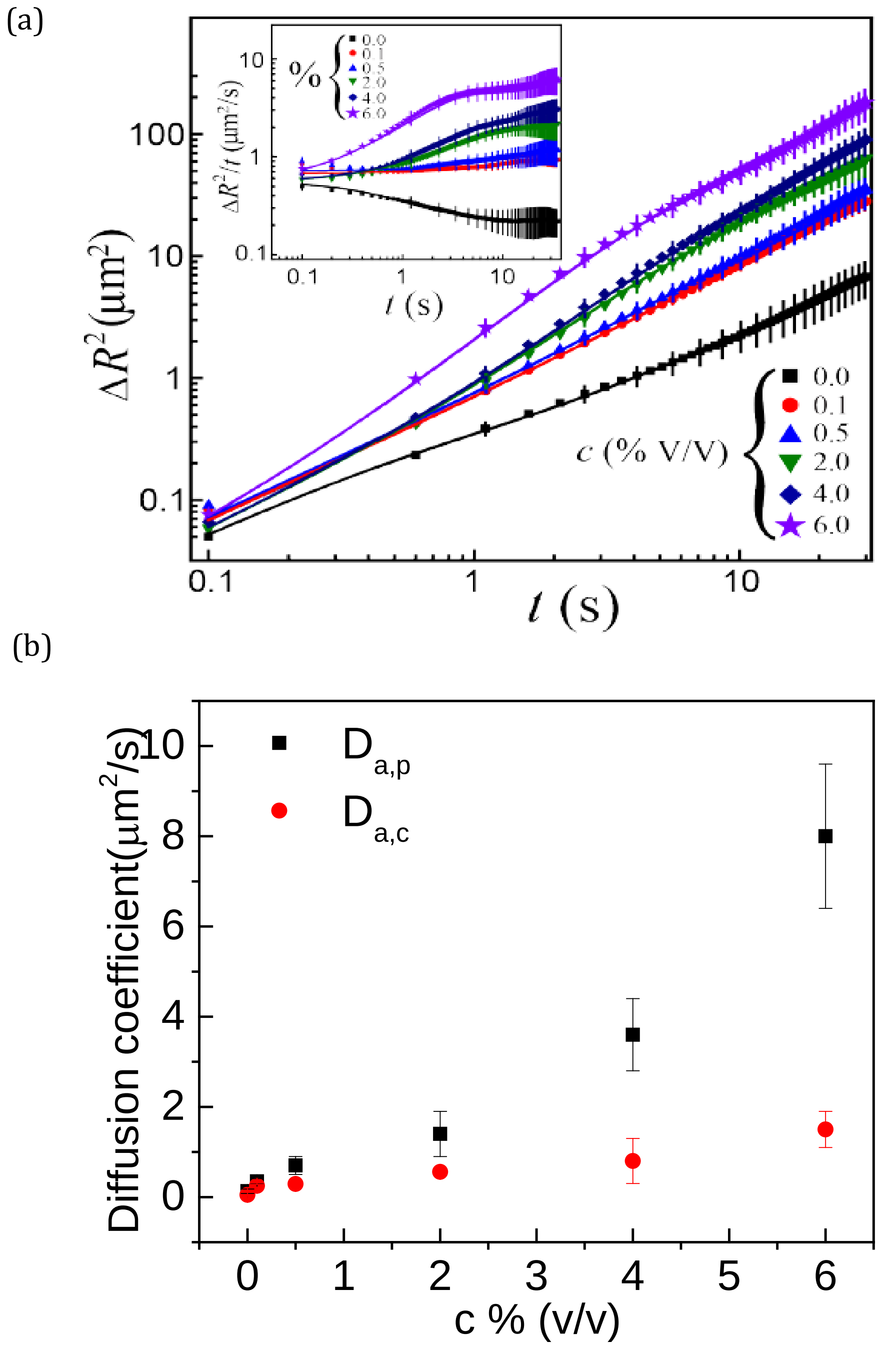

Figure 3.4 Active diffusion on a crystal surface. a) MSDs of the active particles moving atop the crystalline surface for six H_2O_2 concentrations. The solid lines are fits to eq. (4). Inset: rectification of the same data by plotting $\Delta R_{a,c}^2(t)/t$ vs t. b) Longtime diffusion coefficients on plane ($D_{a,p}$) and lattice ($D_{a,c}$) from Table 3.1 and Table 3.2 plotted against H_2O_2 concentrations. Image 3.4a taken from Ref 1.

This observation becomes more transparent when looking at lag times $t \ll \tau_{\mathrm{rot}}$. Under these conditions, the propulsion direction is essentially fixed, and the active motion can be absorbed into an effective potential, $U_{\mathrm{eff}}(x) = U(x) - \zeta_T \boldsymbol{v}.\boldsymbol{x}$ which attains the shape of a tilted washboard. In this case and specializing to one dimension, Eqn. (4) reduces to a stochastic Adler equation, similar to the case of paramagnetic colloids driven over a periodic potential by a constant force[17,18]. At relatively small velocities, $v < v_{\mathrm{c}}$, the particle can escape the periodic minima of $U_{\mathrm{eff}}(x)$ only by diffusion, and these minima vanish for velocities above a critical value, $v > v\mathrm{c} = E\mathrm{a}/\pi\zeta_{\mathrm{T}}L \approx 1$ µm/s, assuming a period length $L = d/\sqrt{3}$ of $U(x)$. This can be compared to an active colloidal particle on plane that propels with a velocity of 0.93 µm/s in a concentration of 4% H_2O_2 (see Table 3.1).

3.4 Discussions

The problem of propulsion of an active colloidal particle above a crystalline surface by a combination of experiment and theory, was studied in this chapter. The experimental system consists of catalytically driven colloidal Janus spheres sedimenting due to gravity on top of a periodic substrate. The strength of self-propulsion is controlled by changing the concentration of the chemical fuel, H_2O_2. Due to a relatively heavy cap, the center of mass of the nearly spherical active particle is slightly displaced from its center, which makes it bottom heavy. The substrate is realized by an HCP colloidal monolayer made of passive stationary colloidal particles of similar size and material. MSD of the Janus particle were investigated and parameters were extracted characterizing different regimes of motion. In particular, the behavior long-time diffusion coefficient was investigated showing how it changes relative to the free diffusivity and how it develops from the Brownian motion at short timescales. Two limiting cases were considered, which permit comparably simple interpretations, and finally their interplay was studied. First, active propulsion above a planar surface was studied, which shows an enhanced long-time diffusion constant and is in agreement with previously known results. Fitting the full time dependence of the MSDs provides additional details on how activity modifies the rotational diffusion. Second, the case of passive diffusion above a crystalline surface was investigated, which plays the role of a trapping potential and results in the suppression of the particle diffusivity. Third, the interplay of these two factors was studied, which have opposite effects on the diffusion constant. It was found that depending on the strength of the activity relative to the strength of the trapping potential, the long-time diffusion constant can be either lower (weak activity) or higher (strong activity) relative to free diffusion. In all instances studied, the diffusion constant of an active particle remains larger than that of a passive particle. These findings are expected to apply to a broad class of self-propelled colloids and microswimmers moving on complicated topography where hydrodynamic coupling phenomena in the lubrication regime[48] are relevant. Further, analogies with this model colloidal system with adatom diffusion on surfaces can also be investigated.

3.5 References

1. Choudhury, U., Straube, A. V., Fischer, P., Gibbs, J. G. & Höfling, F. Active colloidal propulsion over a crystalline surface. *New J. Phys.* **19,** 125010 (2017).
2. Lauga, E. & Powers, T. R. The hydrodynamics of swimming microorganisms. *Rep. Prog. Phys.* **72,** 096601 (2009).
3. Aranson, I. S. Active colloids. *Phys.-Usp.* **56,** 79 (2013).
4. Bechinger, C. *et al.* Active particles in complex and crowded environments. *Rev. Mod. Phys.* **88,** 045006 (2016).
5. Zöttl, A. & Stark, H. Emergent behavior in active colloids. **28,** 253001 (2016).
6. Löwen, H. Colloidal soft matter under external control. *J. Phys.: Condens. Matter* **13,** R415 (2001).
7. Ghosh, A. & Fischer, P. Controlled Propulsion of Artificial Magnetic Nanostructured Propellers. *Nano Lett.* **9,** 2243–2245 (2009).
8. Dobnikar, J., Snezhko, A. & Yethiraj, A. Emergent colloidal dynamics in electromagnetic fields. *Soft Matter* **9,** 3693–3704 (2013).
9. Tierno, P. Recent advances in anisotropic magnetic colloids: realization, assembly and applications. *Phys. Chem. Chem. Phys.* **16,** 23515–23528 (2014).
10. Paxton, W. F. *et al.* Catalytic Nanomotors: Autonomous Movement of Striped Nanorods. **126,** 13424–13431 (2004).
11. Howse, J. R. *et al.* Self-Motile Colloidal Particles: From Directed Propulsion to Random Walk. **99,** 048102 (2007).
12. Jiang, H.-R., Yoshinaga, N. & Sano, M. Active Motion of a Janus Particle by Self-Thermophoresis in a Defocused Laser Beam. **105,** 268302 (2010).
13. Buttinoni, I. *et al.* Dynamical Clustering and Phase Separation in Suspensions of Self-Propelled Colloidal Particles. **110,** (2013).
14. Klapp, S. H. L. Collective dynamics of dipolar and multipolar colloids: From passive to active systems. *Current Opinion in Colloid & Interface Science* **21,** 76–85 (2016).
15. Kroy, K., Chakraborty, D. & Cichos, F. Hot microswimmers. *Eur. Phys. J. Spec. Top.* **225,** 2207–2225 (2016).

16. Evstigneev, M. *et al.* Diffusion of colloidal particles in a tilted periodic potential: Theory versus experiment. *Phys. Rev. E* **77,** 041107 (2008).
17. Straube, A. V. & Tierno, P. Synchronous vs. asynchronous transport of a paramagnetic particle in a modulated ratchet potential. *EPL* **103,** 28001 (2013).
18. Juniper, M. P. N., Straube, A. V., Aarts, D. G. A. L. & Dullens, R. P. A. Colloidal particles driven across periodic optical-potential-energy landscapes. *Phys. Rev. E* **93,** 012608 (2016).
19. Pelton, M., Ladavac, K. & Grier, D. G. Transport and fractionation in periodic potential-energy landscapes. *Phys. Rev. E* **70,** 031108 (2004).
20. Kim, M., Anthony, S. M. & Granick, S. Activated Surface Diffusion in a Simple Colloid System. *Phys. Rev. Lett.* **102,** 178303 (2009).
21. Ma, X., Lai, P.-Y. & Tong, P. Colloidal diffusion over a periodic energy landscape. *Soft Matter* **9,** 8826–8836 (2013).
22. Ma, X., Lai, P.-Y., J. Ackerson, B. & Tong, P. Colloidal transport and diffusion over a tilted periodic potential: dynamics of individual particles. *Soft Matter* **11,** 1182–1196 (2015).
23. Su, Y. *et al.* Colloidal diffusion over a quasicrystalline-patterned surface. *The Journal of Chemical Physics* **146,** 214903 (2017).
24. Evers, F. *et al.* Particle dynamics in two-dimensional random-energy landscapes: Experiments and simulations. *Phys. Rev. E* **88,** 022125 (2013).
25. Su, Y., Ma, X., Lai, P.-Y. & Tong, P. Colloidal diffusion over a quenched two-dimensional random potential. *Soft Matter* **13,** 4773–4785 (2017).
26. Skinner, T. O. E., Schnyder, S. K., Aarts, D. G. A. L., Horbach, J. & Dullens, R. P. A. Localization Dynamics of Fluids in Random Confinement. *Phys. Rev. Lett.* **111,** 128301 (2013).
27. K. Schnyder, S., Spanner, M., Höfling, F., Franosch, T. & Horbach, J. Rounding of the localization transition in model porous media. *Soft Matter* **11,** 701–711 (2015).
28. Leitmann, S. & Franosch, T. Time-Dependent Fluctuations and Superdiffusivity in the Driven Lattice Lorentz Gas. *Phys. Rev. Lett.* **118,** 018001 (2017).
29. Tierno, P., Sagués, F., Johansen, T. H. & Sokolov, I. M. Antipersistent Random Walk in a Two State Flashing Magnetic Potential. *Phys. Rev. Lett.* **109,** 070601 (2012).

30. Martinez-Pedrero, F. *et al.* Bidirectional particle transport and size selective sorting of Brownian particles in a flashing spatially periodic energy landscape. *Physical Chemistry Chemical Physics* **18,** 26353–26357 (2016).
31. Tierno, P. & Reza Shaebani, M. Enhanced diffusion and anomalous transport of magnetic colloids driven above a two-state flashing potential. *Soft Matter* **12,** 3398–3405 (2016).
32. Brazda, T., July, C. & Bechinger, C. Experimental observation of Shapiro-steps in colloidal monolayers driven across time-dependent substrate potentials. *Soft Matter* **13,** 4024–4028 (2017).
33. Palacci, J., Cottin-Bizonne, C., Ybert, C. & Bocquet, L. Sedimentation and Effective Temperature of Active Colloidal Suspensions. *Phys. Rev. Lett.* **105,** 088304 (2010).
34. Geiseler, A., Hänggi, P. & Schmid, G. Kramers escape of a self-propelled particle. *Eur. Phys. J. B* **89,** 175 (2016).
35. Pototsky, A. & Stark, H. Active Brownian particles in two-dimensional traps. *EPL* **98,** 50004 (2012).
36. Schirmacher, W., Fuchs, B., Höfling, F. & Franosch, T. Anomalous Magnetotransport in Disordered Structures: Classical Edge-State Percolation. *Phys. Rev. Lett.* **115,** 240602 (2015).
37. Zeitz, M., Wolff, K. & Stark, H. Active Brownian particles moving in a random Lorentz gas. *Eur. Phys. J. E* **40,** 23 (2017).
38. Happel, J. & Brenner, H. Low Reynolds number hydrodynamics: with special applications to particulate media. (Springer Netherlands, 1983).
39. Palacci, J., Sacanna, S., Steinberg, A. P., Pine, D. J. & Chaikin, P. M. Living Crystals of Light-Activated Colloidal Surfers. **339,** 936–940 (2013).
40. Zöttl, A. & Stark, H. Hydrodynamics Determines Collective Motion and Phase Behavior of Active Colloids in Quasi-Two-Dimensional Confinement. *Phys. Rev. Lett.* **112,** 118101 (2014).
41. Dunstan, J., Miño, G., Clement, E. & Soto, R. A two-sphere model for bacteria swimming near solid surfaces. *Physics of Fluids* **24,** 011901 (2012).
42. Schwarz-Linek, J. *et al.* Phase separation and rotor self-assembly in active particle suspensions. *PNAS* **109,** 4052–4057 (2012).

43. Ma, X., Hahn, K. & Sanchez, S. Catalytic Mesoporous Janus Nanomotors for Active Cargo Delivery. *J. Am. Chem. Soc.* **137,** 4976–4979 (2015).
44. Das, S. *et al.* Boundaries can steer active Janus spheres. **6,** 8999 (2015).
45. Uspal, W. E., Popescu, M. N., Dietrich, S. & Tasinkevych, M. Self-propulsion of a catalytically active particle near a planar wall: from reflection to sliding and hovering. *Soft Matter* **11,** 434–438 (2014).
46. Simmchen, J. *et al.* Topographical pathways guide chemical microswimmers. **7,** 10598 (2016).
47. Nourhani, A., Brown, D., Pletzer, N. & Gibbs, J. G. Engineering Contactless Particle–Particle Interactions in Active Microswimmers. *Adv. Mater.* n/a-n/a doi:10.1002/adma.201703910
48. Schaar, K., Zöttl, A. & Stark, H. Detention Times of Microswimmers Close to Surfaces: Influence of Hydrodynamic Interactions and Noise. *Phys. Rev. Lett.* **115,** 038101 (2015).
49. Gao, W. & Wang, J. Synthetic micro/nanomotors in drug delivery. *Nanoscale* **6,** 10486–10494 (2014).
50. Choudhury, U., Soler, L., Gibbs, J. G., Sanchez, S. & Fischer, P. Surface roughness-induced speed increase for active Janus micromotors. **51,** 8660–8663 (2015).
51. Gibbs, J. G. & Zhao, Y. Self-Organized Multiconstituent Catalytic Nanomotors. **6,** 1656–1662 (2010).
52. Bardosova, M., Pemble, M. E., Povey, I. M. & Tredgold, R. H. The Langmuir-Blodgett Approach to Making Colloidal Photonic Crystals from Silica Spheres. *Advanced Materials* **22,** 3104–3124
53. Ebbens, S. *et al.* Electrokinetic effects in catalytic platinum-insulator Janus swimmers. **106,** 58003 (2014).
54. Goldman, A. J., Cox, R. G. & Brenner, H. Slow viscous motion of a sphere parallel to a plane wall—I Motion through a quiescent fluid. *Chemical Engineering Science* **22,** 637–651 (1967).
55. Perkins, G. S. & Jones, R. B. Hydrodynamic interaction of a spherical particle with a planar boundary: II. Hard wall. *Physica A: Statistical Mechanics and its Applications* **189,** 447–477 (1992).

3.6 Appendix

The following derivation is from Ref [1] and was provided by Prof. Felix Höfling (TU Berlin). It has been included in the thesis for the benefit of the reader. Please refer to Ref [1] for further details.

3.6.1 Mean-square displacement of a self-propelled particle atop a crystalline surface

Active motion on a periodic potential can be modelled by overdamped Langevin equations as

$$\dot{\mathbf{x}}(t) = \boldsymbol{v}(t) - \zeta^{-1}\nabla U\big(\mathbf{x}_c(t)\big) + \sqrt{\frac{2kT}{\zeta}}\,\boldsymbol{\eta}(t), \qquad \text{(A1)}$$

Here ***x(t)*** and ***v(t)*** are particle position and velocities projected on to the plane of crystalline surface, $\boldsymbol{\eta}(t)$ is two dimensional Gaussian white noise with zero mean and unit co-variance to describe passive Brownian motion on a plane where the diffusion constant is D_0=kT/ζ.

Diffusion in a periodic surface potential is described by the Langevin equation [Eq. (A1) and setting $\mathbf{v} = 0$]

$$\dot{\mathbf{x}}_c(t) = -\zeta^{-1}\nabla U\big(\mathbf{x}_c(t)\big) + \sqrt{\frac{2kT}{\zeta}}\,\boldsymbol{\eta}(t), \qquad \text{(A2)}$$

the solution of which is well approximated by [2,3]

$$\Delta R_s^2(t) = 4(D_0 - \Delta D_c)t - 4\,\Delta D_c\,\tau_c\big(e^{-t/\tau_c} - 1\big). \qquad \text{(A3)}$$

This equation describes a crossover from free diffusion with $D_0 = kT/\zeta$ at short times to diffusion at long times with reduced diffusion constant $D_0 - \Delta D_c$, where ΔD_c is the reduction of longtime diffusion constant due to crystalline surface. The crossover occurs at the time scale τ_c, after which the particle has explored a single potential minimum. The inverse τ_c^{-1} may be interpreted as the attempt rate for escaping from the minimum. The corresponding velocity autocorrelation function is given by

$$Z_c(t) = \frac{1}{4}\frac{\mathrm{d}^2}{\mathrm{d}t^2}\Delta R_\mathrm{c}^2(t) = D_0\delta(0) - \frac{\Delta D_\mathrm{c}}{\tau_c}\mathrm{e}^{-t/\tau_\mathrm{c}}. \qquad \text{(A4)}$$

Combining Eq. (A4) with the active motion [Eq. (A1)] simply adds the autocorrelation of the propulsion velocity,

$$Z(t) = Z_c(t) + \tfrac{1}{2}\langle \mathbf{v}(t)\cdot\mathbf{v}(0)\rangle, \qquad \text{(A5)}$$

Assuming, the diffusive motion in the potential is independent from the propulsion velocity, i.e., $\boldsymbol{\eta}(t)$ and $\mathbf{v}(t)$ are independent random increments. Modelling the persistence of the propulsion directions by $\langle \mathbf{v}(t)\cdot\mathbf{v}(0)\rangle = v^2\mathrm{e}^{-t/\tau_\mathrm{rot}}$ (e.g., due to rotational diffusion) immediately yields the MSD after integration:

$$\Delta R_{a,c}^2(t) = 4\int_0^t (t-s)\ Z(s)\ \mathrm{d}s \qquad \text{(A6)}$$

$$\Delta R_{a,c}^2 \ = 4\left(D_{0,\mathrm{p}} - \Delta D_c + \frac{v^2\tau_\mathrm{rot}}{2}\right)t - 4\ \Delta D_c\ \tau_\mathrm{s}\left(\mathrm{e}^{-t/\tau_c} - 1\right) + 2v^2\tau_\mathrm{rot}^2\left(\mathrm{e}^{-t/\tau_\mathrm{rot}} - 1\right). \qquad \text{(A7)}$$

Additional References

1. Choudhury, U., Straube, A. V., Fischer, P., Gibbs, J. G. & Höfling, F. Active colloidal propulsion over a crystalline surface. *New J. Phys.* **19,** 125010 (2017).
2. Risken, H. & Vollmer, H. D. Correlation functions for the diffusive motion of particles in a periodic potential. *Z Physik B* **31,** 209–216 (1978).
3. Fulde, P., Pietronero, L., Schneider, W. R. & Strässler, S. Problem of Brownian Motion in a Periodic Potential. *Phys. Rev. Lett.* **35,** 1776–1779 (1975).

4 : Nanodiamonds that Swim

This chapter is largely based on the journal paper “Nanodiamonds that swim” Ji-Tae Kim, Udit Choudhury, Hyeon-Ho Jeong and Peer Fischer , which has appeared in *Advanced Materials* **29** (30), 1701024, (2017)[1]

The author together with J.K., built the microwave-antenna containing chamber, optical setup for Nitrogen Vaccancy(NV) center sensing, fabricated the thermophoretic samples, performed the measurements, and analyzed the data.

4.1 Introduction

So far this thesis has discussed the motion of chemically-propelled active colloids. In Chapter 2 the “free” diffusion has been considered. In Chapter 3 the motion of a self-propelled colloid subject to Bownian and chemically-propelled diffusion atop a structured durface. Here, the question is asked if the activity can be controlled and used, for instance to improve existing sensors. This question is addressed by examining what can be gained in finding ways to propel and orient colloidal nanosensors, like nanodiamonds.

Nanodiamonds (ND) are emerging as nanoscale quantum probes for bio-sensing and imaging. Generally, they are placed in the vicinity of biological material and then imaged. A nitrogen-vaccancy defect in the diamond lattice causes spin-dependent fluorescence, which is sensitive to outside fields and perturbations. By developing methods that can be used to accurately manipulate the nanodiamond’s position and orientation in aqueous solutions, spatial sensing of local fields could be carried out.

This chapter describes, what is believed to be the first propelled colloidal NDs. For this a ND crystal containing nitrogen vacancy (NV) center is coupled to a light-driven self-thermophoretic colloid. A 532 nm green laser is used to illuminate a ND-containing Janus swimmer. This heats up metal patch on the colloid and creates a local temperature gradient. Consequently, the colloid swims by self-thermophoresis. By designing the shape of the colloid with glancing angle physical vapor deposition, its locomotion - from translational to rotational motion is shown to be controllable by shape-dependent hydrodynamic interactions. The same 532 nm laser is then used to excite the NV center fluorescence and through optical readout of the electron spin resonance spectrum, an external magnetic field can be sensed and measured. Thus, by using active motion at the nanoscale new sensing capabilities are demonstrated, where a self-propelled particle could be used as a carrier for nano-sensors to spatially scan an area and map out local field distributions.

4.2 Motivation

Nanodiamonds containing nitrogen vacancy (NV) centers have emerged as a promising material system for room-temperature quantum information processing,[2] quantum optics,[3] and nanoscale metrology including the detection of magnetic fields,[4,5] electric fields,[5] as well as micron-scale temperature fields.[6] The strong photostable fluorescence of NV centers in the near infrared (600 - 850 nm) and the biocompatibility of NDs have facilitated diverse applications in bio-sensing and imaging.[7–11] To fully utilize the information of the NV electron spins for applications in bioscience and in complex fluids, individual NDs must be positioned and oriented.[12,13]

To this end, an atomic force microscope (AFM) tip has been used for positioning a NV center on a target substrate.[4,14–16] Although the scanning-probe provides nanometer scale spatial resolution, the AFM cantilever geometrically restricts manipulation of the NV's spin orientation and thus makes operation in biological media difficult. To realize the manipulation in fluids, some elegant trapping methods have been designed. Optical tweezers and anti-Brownian electrokinetic (ABEL) traps have been previously used to trap and manipulate the position of photoactive nanodiamonds.[17–20] Optical tweezers are advantageous for precise manipulation, but they are not easily used in a complex heterogeneous environment. ABEL traps allow the localization of individual NDs in a microfluidic platform,[21] but cannot be used to control the orientation of the NDs (NV centers) precisely. Previously, NDs have thus far only been manipulated using "passive approaches". The challenge lies in devising a means to provide the NDs with a "handle" that can be used to manipulate the nanodiamonds, which because of their size are difficult to manipulate.

Since the readout of NV centers in nanodiamonds requires light, the same excitation source can also be used to power the swimming motion of NDs. N this chapter it is shown that light-driven self-thermophoresis can be used to manipulate the position and orientation of NV centers in fluids, when the ND is attached to a colloid. The self-thermophoretic micromotor containing the ND crystal is fabricated by a scalable shadow growth physical vapor deposition process.[22,23] No additional external forces or torques are applied to the swimmer. Precise locomotion patterns can be used to control the spatial position of the NV fluorescence in a fluidic medium, and the hybrid ND-colloids can be used to perform self-driven vector magnetometry.

4.3 Results

4.3.1 Design of ND swimmers

Figure 4.1 depicts the design of the active ND swimmers. The swimmers consist of three parts: (head) a 40 nm ND crystal with a NV center, (body) a microparticle with programmed shape, and an active platinum (Pt) pad. The propulsion mechanism of the swimmers is light-driven self-thermophoresis.[24–26] The local temperature gradient ∇T near the Pt pad is produced by the absorption of the same light source that is used to excite the NV fluorescence (532 nm laser with wide-field illumination). No chemical fuel is used. This asymmetric temperature profile establishes a thermoosmotic flow along the surface of the swimmer, driving the self-propulsion. Pt was chosen rather than gold[27] or carbon[28] as it has a lower absorption at 532 nm, which means that the swimmers move more slowly at the light levels used to excite the NV centers (< 100 mW, an incident laser power into the microscope) such that their electron spin resonance signal (ESR) can be stably observed. To drive the motion of the swimmers, a more intense illumination (> 300 mW) is applied for a short period. The shape of the body and the position of the Pt pad were specifically programmed for controlling, respectively, the translational and rotational motion of the swimmer. Figure 4.1a shows a 2 μm polystyrene (PS) Janus particle half-coated with Pt that exhibits enhanced self-thermophoretic translational motion under laser illumination. A different shape of colloid (Figure 4.1b) gives rise to rotation without any translation. The rotary swimmer consists of a 2 μm PS bead attached to a 4 μm TiO_2 arm that is coated with a small Pt patch. The temperature gradient ∇T causes it to rotate with an angular velocity ω

due to the asymmetric shape of the swimmer's body.[29] Each type of the swimmer emits a strong NV fluorescence signal as shown in the insets of Figures 4.1a and 4.1Figure 4.b.

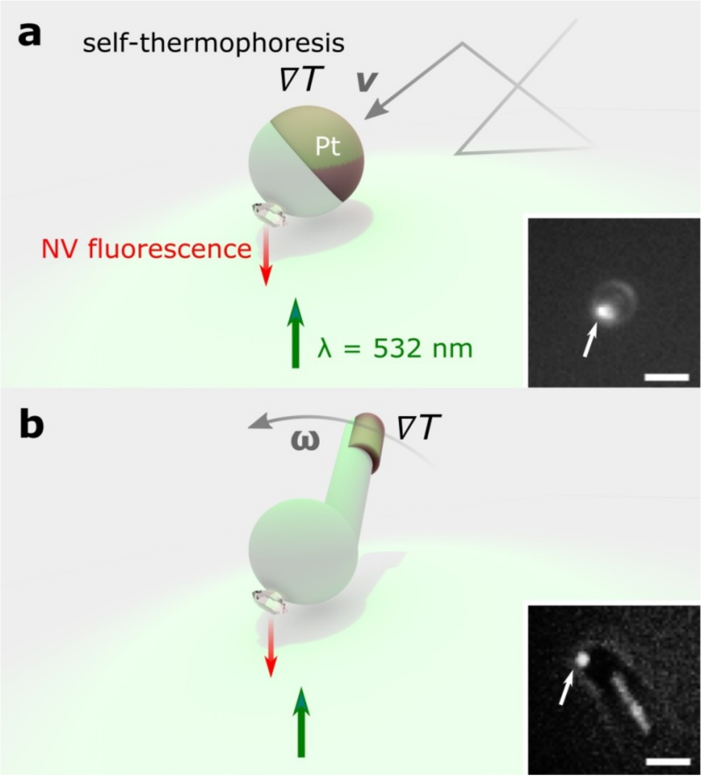

Figure 4.1: Design of self-thermophoretic active nanondiamond (ND) swimmers. a,b) The swimmers consist of three parts: (head) an ND with nitrogen vacancy (NV) centers attached to a microparticle (body) with programmed shape (tail) that contains platinum (Pt) pad at a location. Illumination by a (532 nm) laser excitation creates a local temperature gradient ∇T near the Pt pad, which causes the swimmer to self-propel by thermophoresis. The same laser is used to simultaneously excite and observe the NV electron spin resonance by its fluorescence. Each swimmer body is designed for (a) translational (v) or (b) rotational (ω) motion. Inset: Fluorescence images of ND swimmers where the NV center is clearly visible (scale bar: 2 μm). Image taken from Ref.1.

4.3.2 Fabrication of ND swimmers

To couple a single ND crystal to a micromotor, the NDs need to be well-separated when they are deposited onto a substrate. This was achieved by exploiting the electrostatic interactions between NDs and the substrate to obtain a well-dispersed monolayer. Figure 4.2a shows individually deposited NDs on a silicon (Si) substrate. Carboxylated-NDs (forming surface bound carboxylate anions in aqueous solution) were deposited onto an amine functionalized Si substrate (positively charged surface) by spin-coating. The density of the deposited NDs was optimized by dilution of the ND stock solution (1:5) with deionized water (see Figure 4.2b and Figure 4.2c). After removing any residual chemical species on the ND-deposited substrate with an O_2 plasma treatment, PS (2 μm diameter) beads were deposited onto the ND-coated wafer (Figure 4.2b) by Langmuir-Blodgett deposition. The low glass transition temperature of the PS spheres ($T_g \sim 94^{O}C$) and the superior thermal conductivity of the diamonds provide a simple way to bond an ND crystal to a micromotor by heating. Figure 4.3 shows contact of a PS sphere on a Si wafer for different heating times at $90^{O}C$. As the heating times increase, the contact angle with the wafer decreases and the bead adheres more tightly on the wafer. By optimizing heating time times, it was found that heating to $90^{O}C$ for 20 s softens the PS beads such that the ND just fuses with the PS matrix. A rapid cooling step ensures that the NDs remain tightly adhered to the PS spheres without any significant deformation of the PS beads (Figure 4.4b). This simple protocol for the ND dispersion and fusion to colloids forms a general platform from which a wide range of ND-containing material systems can be readily formed in large numbers.

To manipulate and enhance the translational diffusion, the colloids are now transformed into Janus particle swimmers. As shown in Figure 4.4c, 50 nm of Pt is coated on top of the PS spheres by electron-beam evaporation at normal incidence. A FE-SEM picture of a ND crystal and a PS-Pt Janus sphere is also shown in Figure 4.4c. To fabricate rotational swimmers, 4 μm TiO_2 rods was deposited onto the PS spheres by GLAD shadow growth at an angle of 85^{O} with substrate rotation. The deposition angle promotes growth of rods due to the self-shadowing effect of adjacent structures. After depositing TiO_2 rods, the substrate was tilted back to 0^0 and 15 nm of Pt was deposited to coat one side of the arm. The final swimmer structure is shown in Figure 4.4d. Fabrication on a three-inch wafer produces about 10^9 ND swimmers (Fig.A1).

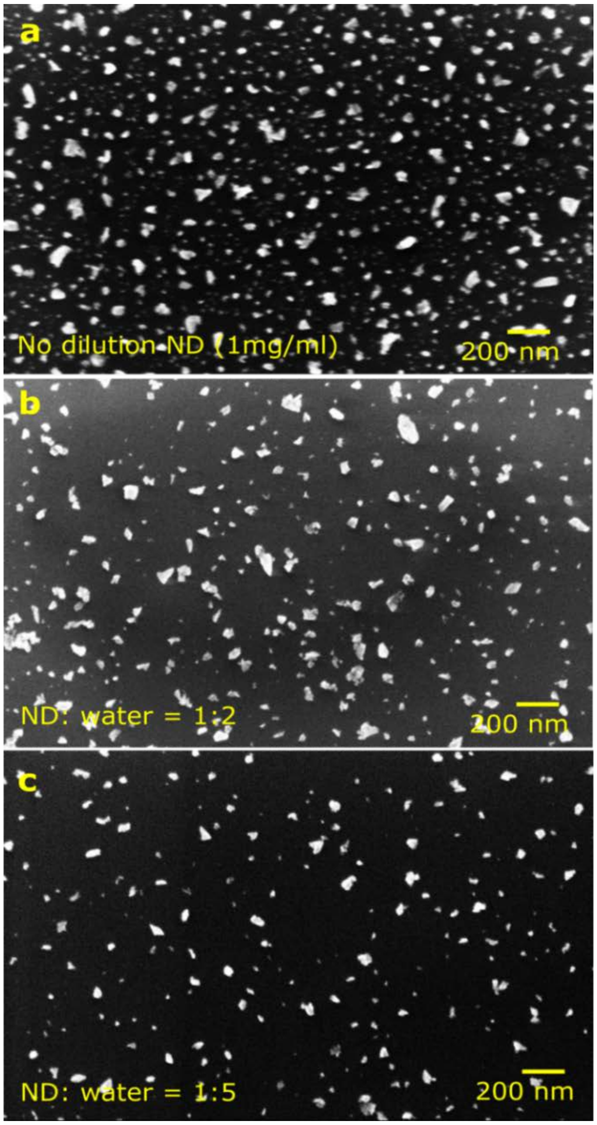

Figure 4.2 : Nanodiamond distribution a) ND dispersion on amine functionalized Si wafer; b) ND dispersion at 1:2 dilution; c) ND dispersion at 1:5 dilution. Image taken from Ref.1.

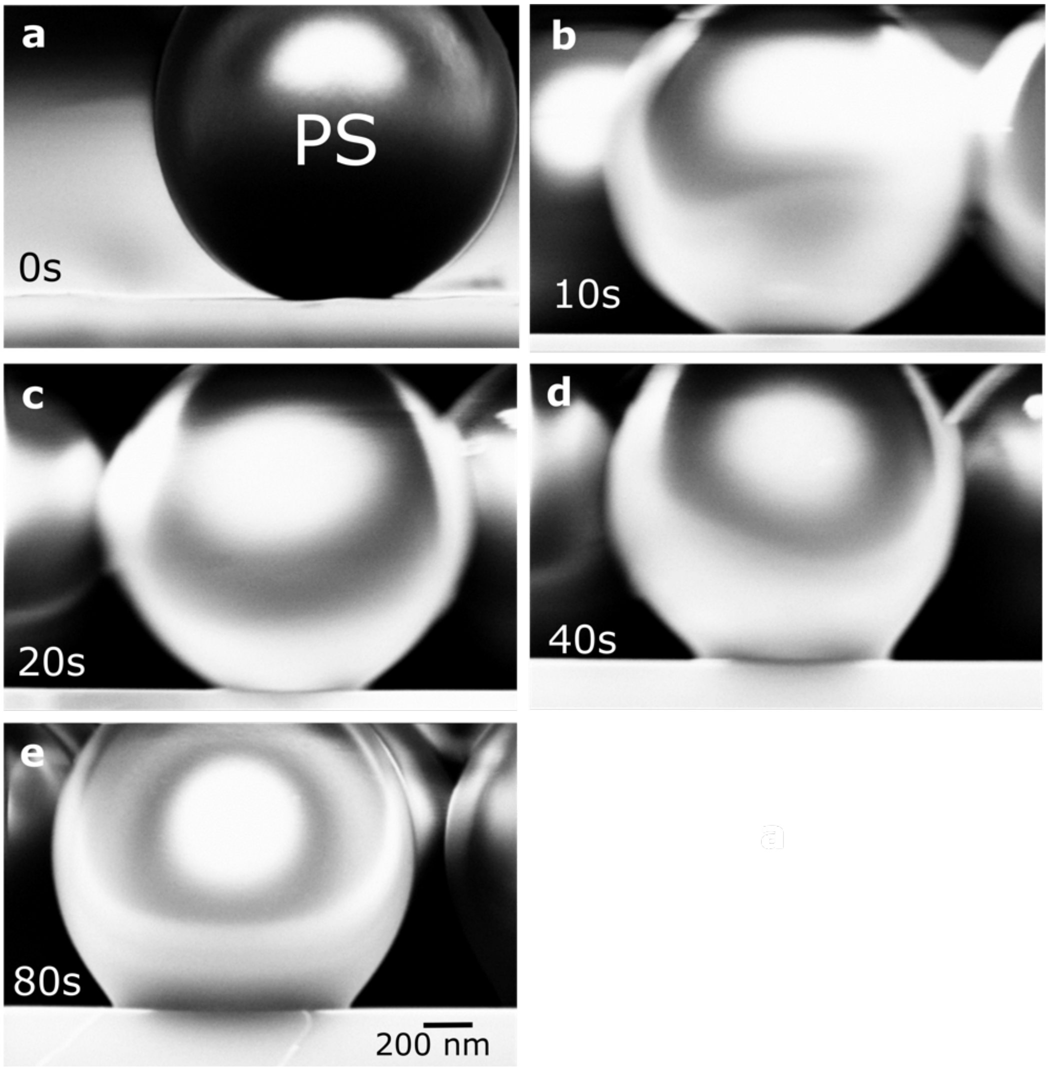

Figure 4.3 : Contact angle of Polystyrene beads on Si wafer for annealing time of a) 0s, b) 10s, c) 20s, d) 40s, e) 80s. Image taken from Ref.1.

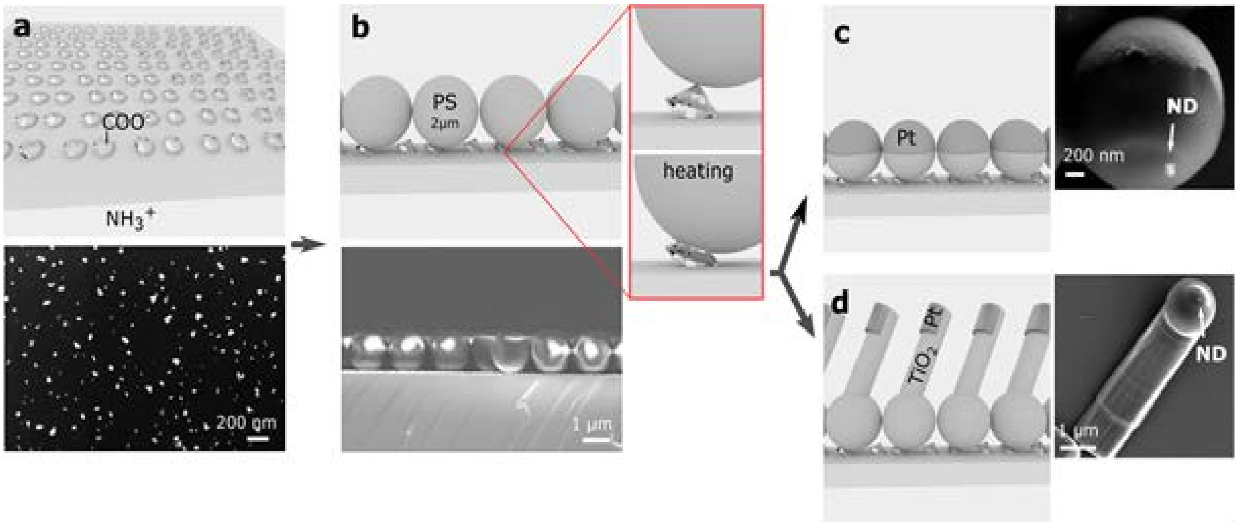

Figure 4.4 Fabrication of ND swimmers. a) Electrostatic deposition of NDs on a Si wafer. Carboxylated NDs (ND-COOH) are spin-coated on an amine-functionalized Si wafer. The NDs assemble with an average distance of ≈100 nm separation. b) Monolayer of 2 μm polystyrene (PS) beads is deposited onto the ND-decorated Si wafer in a Langmuir–Blodgett method. Subsequent heating to 90 °C for 20 s softens the PS beads and causes the NDs to attach to the PS beads (inset). c) For microswimmers that show strongly enhanced translational motion, the Pt is coated on the PS bead, resulting in a Janus sphere. d) To produce rotational swimmers, a TiO_2 arm with a length of 4 μm is deposited on a PS sphere and subsequently 15 nm of Pt is coated at one side of the arm using shadow deposition. Image taken from Ref.1.

4.3.3 Motion of ND swimmer

Figure 4.5 shows the motion of two representative types of ND swimmers in a 1:20 water-glycerol solution ($\eta \sim 0.366\ Ns/m^2$). A thin quartz glass chamber with a photo-lithographically patterned 5 μm spacer was used for this study. The two-dimensional (2D) trajectory of the ND attached to a PS-Pt Janus sphere under wide-field laser illumination is shown in Figure 5a. As the laser power is increased from 0, to 100, to 200 mW, the swimmer moves faster and its motion transforms from random Brownian motion to ballistic linear motion. Since, rotational diffusion of the swimmer is much suppressed in the high viscosity medium, the swimmer has a longer persistence length and moves in a linear trajectory on the timescale of the experiment. Based on the above data, mean square displacements (MSD) of the moving swimmer is calculated. The dependence of the MSD for different laser powers is shown in the graph of Figure 4.5b. The slope of the MSD increases with the illuminated laser power, as expected. The two-dimensional MSD of a self-thermophoretic swimmer[13] (Equation A2, Appendix 4.7) can be approximated as

$$\mathrm{MSD} = 4\mathrm{D}t + v^2t^2 \qquad (1)$$

Where D is diffusion constant, t is time, and v is self-propelling speed. Because v is proportional to ∇T, v in Figure 4.5c is seen to depend linearly on the laser power (here changed from 0 to 400 mW). This result implies that translational speed of the ND swimmers can be directly controlled by the laser power.

Next, the dynamics of the rotational swimmers is studied. Figure 4.5d show a rotational motion of an ND swimmer consisting of an ND crystal, a PS sphere (2 μm diameter), and a Pt-coated TiO_2 tail (4 μm length). The geometry of the asymmetric swimmer ensures a constant rotation under laser illumination. The angular speed ω can be controlled in the range of 0.5 to 5 degree/sec by changing the laser power from 100 to 600 mW, as shown in Figure 4.5e. Above the laser power of 300 mW acting as threshold, the ω increases linearly with the laser power. This rotational motion enables one to manipulate the orientation of NV electron spins, which are fixed in the diamond lattice. Control of the orientation is essential for vector magnetometry. Sensing experiments were carried out at optical powers below 100 mW, while rotational manipulation of the swimmers was performed at powers of more than 300 mW. The two power levels ensure that thermal drift is minimized whilst the spectrum is recorded. Figures 4.6 a, b, c and d shows frames of rotary motion of a nanodiamond swimmer. Thus, an active vector magnetometer in fluids that does not require a mechanical contact can be realized.

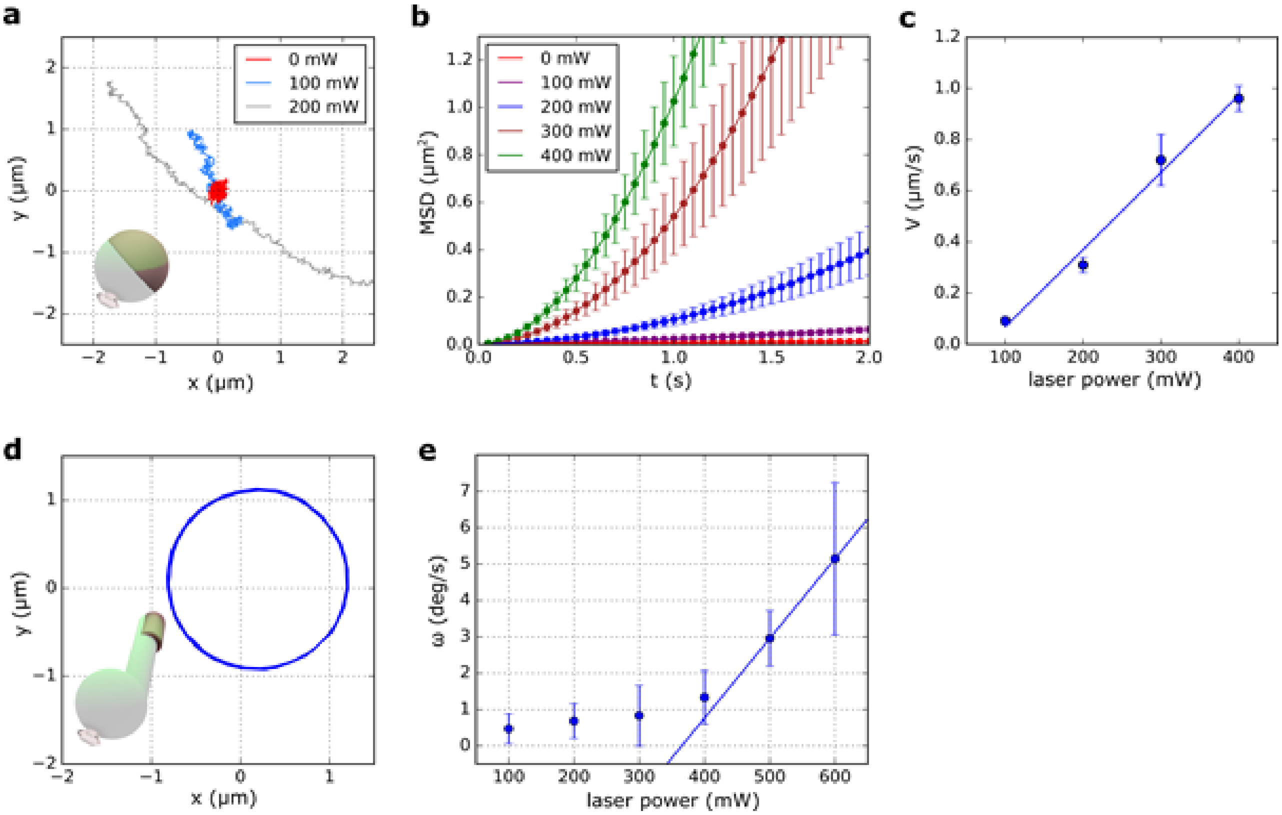

Figure 4.5: Trajectories of ND swimmers that show (a)–(c) controlled translational diffusion and (d) and (e) rotational diffusion. a) 2D trajectory of an ND attached to a PS-Pt Janus sphere (2 µm diameter, Pt thickness: 15 nm) for different laser powers at λ = 532 nm (red = 0 mW, blue = 100 mW, and gray = 200 mW). b) Corresponding mean square displacements (MSDs) and c) associated translational velocities *v* as a function of the laser power (from 0 to 400 mW). d) 2D trajectory of an ND attached to a rotational swimmer composed of a 2 µm PS bead, a 4 µm TiO_2 arm, and a 15 nm thick Pt pad. e) Dependence of angular speed, ω, as function of the laser intensity. Image taken from Ref.1.

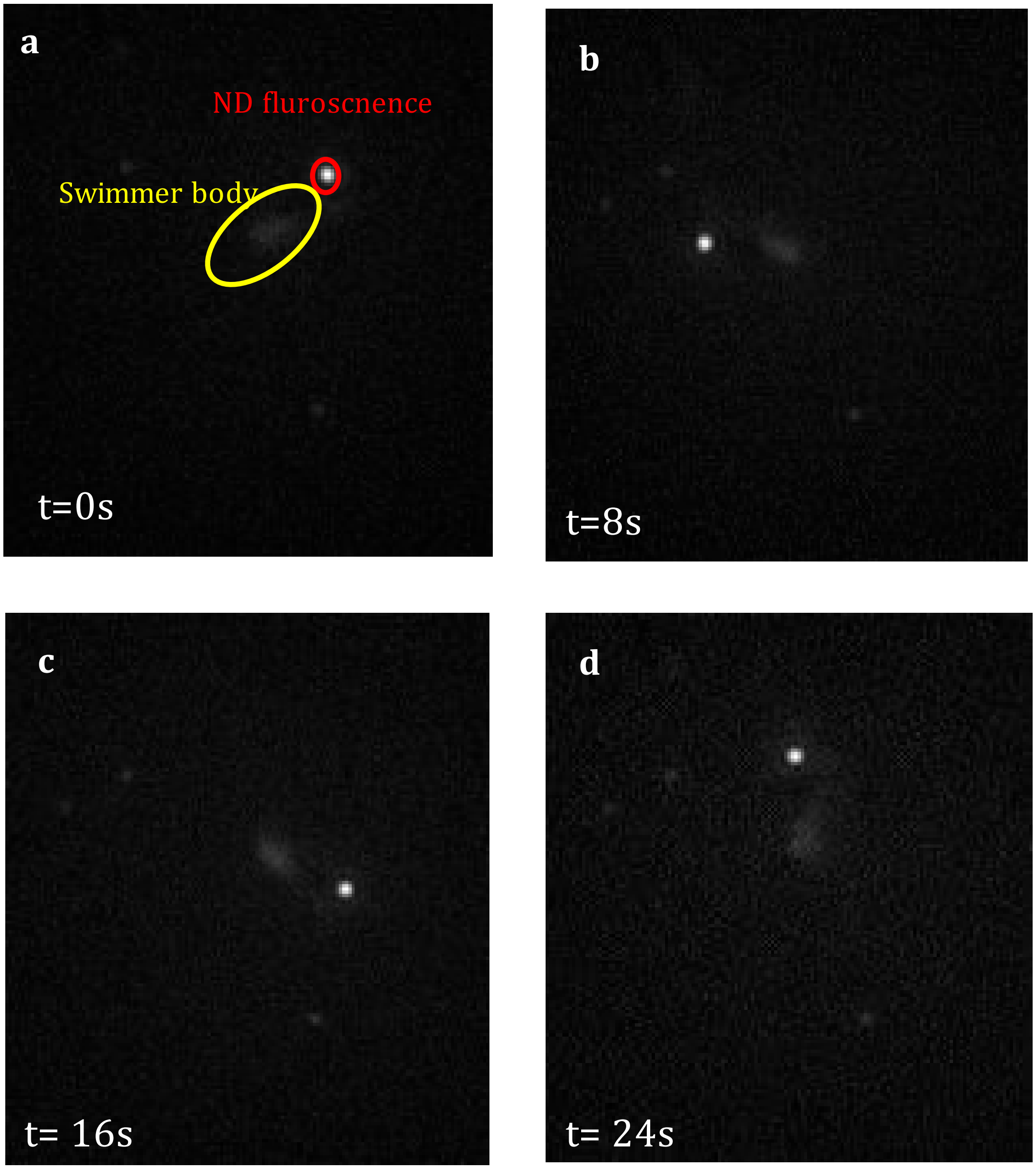

Figure 4.6. Motion of a rotary nanodiamond swimmer. a) Initial position of swimmer at t=0s. Consecutive positions at b) t=8s, c)t=16s and d)t=24s.

4.3.4 Electron spin resonance of ND swimmers

NV centers are point defects in the diamond lattice that consists of a substitutional nitrogen atom adjacent to a vacancy site. Since, the defect is within the diamond lattice, it remains protected with remarkable photo-stability and can be conveniently used in any fluid. The optical properties of NV centers can be described with the energy level diagram (Fig. 4.7).[7] It consists of 3 electronic levels, with triplet ground state $^3A_2$ and excited state ^3E and a metastable singlet state of $^1E_1$ and $^1A_1$.The ground to excited state transition can be excited with wavelength 532nm. It then emits fluorescence in the range of 637nm-800nm. By filtering out the excitation wavelength, the fluorescence can be observed. The spin triplet states are further split into three sublevels $m_s=0$ and $m_s=\pm1$ states. The $m_s= \pm1$ states are degenerate and the energy difference between the sublevels is 2.87 GHz with $m_s=0$ being energetically lower. External magnetic field splits the $m_s=\pm1$ states and they shift in opposite directions with an energy separation of $2\gamma_{NV}B$, where γ_{NV} is the electron gyromagnetic ratio and B_z is the externally applied magnetic field.

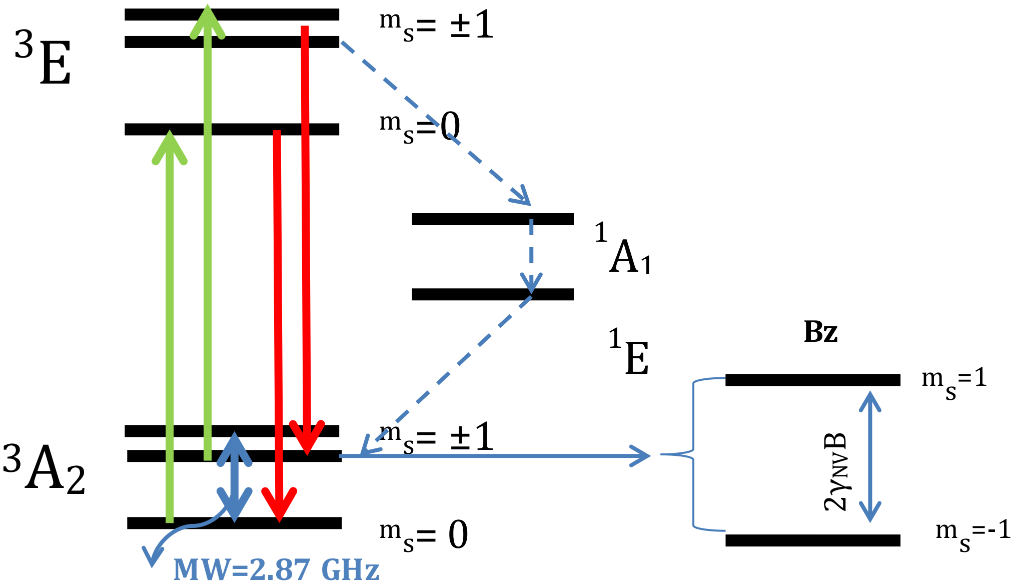

Figure 4.7 : Energy level diagram of NV center. Image adapted from Ref. 7

To validate the feasibility of sensing in liquid environments, electron spin resonance (ESR) measurements on the rotational ND swimmer was performed in a viscous water-glycerol mixture (1:50). A customized quartz chamber with a lithographically patterned microwave antenna was used. No significant motion of the swimmers even at a laser power of 250 mW was observed. Stable ESR signals could thus be recorded with suppressed thermal fluctuations, which demonstrate the ND sensor's functionality in fluids. The scanning range was set from 2.75 GHz to 3 GHz. The decrease of fluorescence intensity at 2.87 GHz confirmed the presence of a NV center defect in the diamond crystal (Figure 4.8a). Then, to check functionality of the NV center, the swimmer was set into motion and the microwave field was switched on and off at 2.87 GHz while the swimmer was rotating. It was found that due to small variations in the z-position during rotation, the swimmer's intensity followed an oscillatory path. When the microwave field was turned on, the intensity decreased due to a decrease in fluorescence intensity and on turning off the microwave field the amplitude returned to its original level (Figure 4.8b). This proved that the NV center is functional in a rotary swimmer and can be used for vector magnetometry. Further, for testing the functionality of the NV center for multiple cycles, the microwave field at 2.87 GHz was switched on and off multiple times and the fluorescence intensity was recorded. Figure 4.8c shows that the fluorescence intensity follows the microwave input signal.

Based on the rotational dynamics of the swimmers, a protocol to sense external magnetic fields was developed. The fabrication method produced samples with both single and multiple NDs attached to the swimmer. About, one in five swimmers contained a single ND. Since the fabrication method produces billions of swimmers on a single wafer, enough particles with a single ND for ESR measurements could easily be obtained. Optical powers lower than 100 mW were used to ensure that the swimmer remains stable during ESR measurements in the presence of a magnetic field. The beam spot of the laser was also reduced by an iris to illuminate the NV center without heating the metallic part. For the manipulation of the motion, the beam was expanded and the laser power was increased to rotate the swimmer.

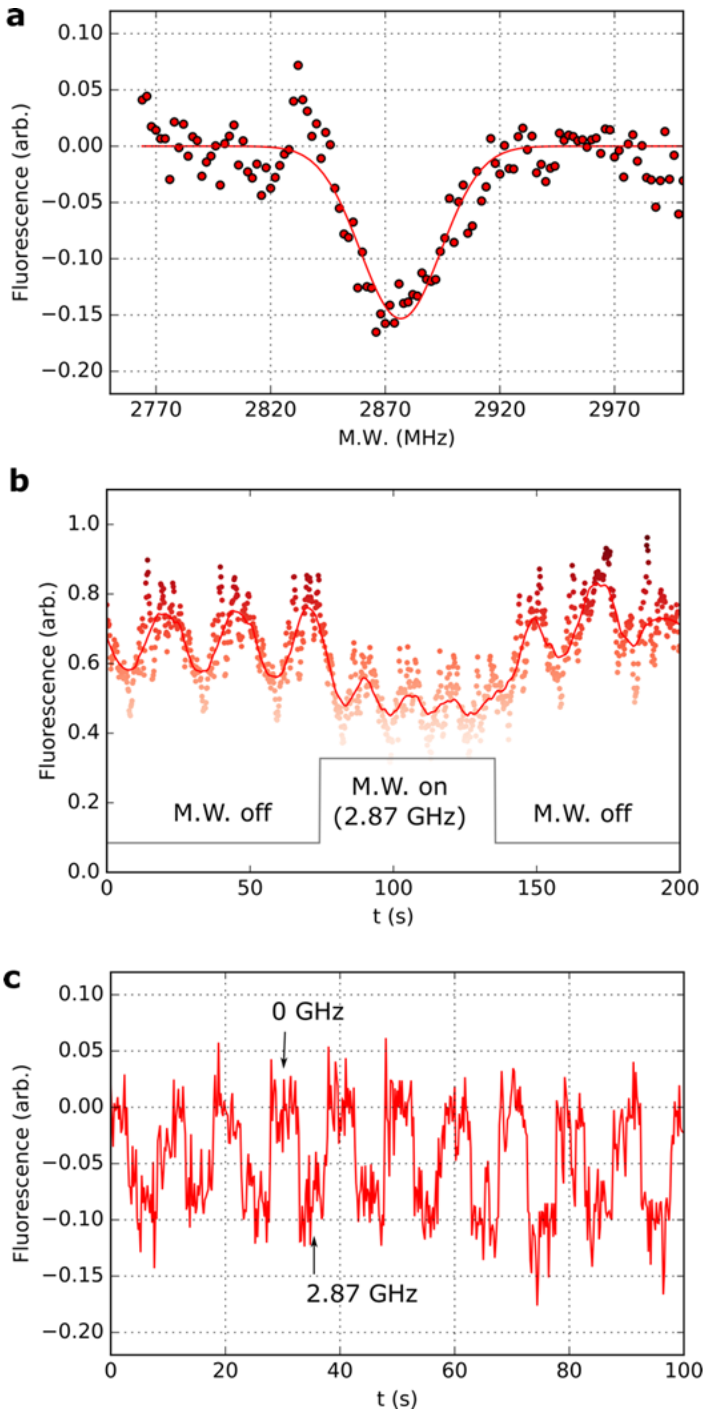

Figure 4.8: Electron spin resonance of ND swimmer a) ESR resonance in 1:50 glycerol b) Swimming motion of rotary swimmer in ND swimmer in 1:20 glycerol solution. Microwave field at 2.87 GHz turned on between 80s to 140s. c) Fluorescence intensity variation as function of microwave field on/off sequence at 2.87 GHz frequency. Image taken from Ref.1.

Figure 4.9 shows the optically detected magnetic resonance (ODMR) spectra of the ND swimmers. The extinction of the NV fluorescence with microwave excitation at 2.87 GHz is shown. The microwave scanning was done between 2.8 GHz and 2.95 GHz to reduce the scanning time for measurements. Figure 4.9a shows the response of a static swimmer without a magnetic field. When a magnetic field (B-field) of 8 G (0.8 mT) was applied along the y-axis as shown in the schematic (Figure 4.9b), two resonance peaks with a splitting of 33 MHz were observed (Figure 4.9c) from the ND swimmer of orientation as shown in Figure 4.10a. After the laser-induced swimmer's rotation with $\Delta\varphi = 52^0$(Figure 4.10b, θ is constant), the width of the splitting decreased to 21 MHz as shown in Figure 4.9d. Further, the component of the B-field along the NV-spin axis can be deduced as $B_{eff} = B \cos(\varphi) \sin(\theta)$ and the Zeeman splitting is proportional to $2\gamma B_{eff}$.[30] From the two measurements in Figures 4.9 c and d the angular orientations $\varphi = -1.5^0$ and $\theta = 47.8^0$ were obtained. This demonstration clearly shows an effective procedure of active vector-magnetometry by the ND swimmers.

4.4 Discussion

In this work, a simple procedure to obtain billions of complex ND-containing colloids was developed to demonstrate the first self-phoretic ND swimmers. Glancing angle deposition was used to control and design the shape of the colloids. The motion and sensing was performed with the same 532 nm laser. By using different power level for each, these two functionalities were decoupled. Electron spin resonance measurements on the NV center of the ND confirmed the possibility of detecting external magnetic fields. Further, self thermophoretic motion of the colloids demonstrated the ability to move the NV-sensors and scan a two-dimensional geometry. Thus, ND swimmers enable new possibilities for nanoscale metrology in biological systems.[31,32] Possible applications include parallel vector-magnetometry, temperature sensing, and integrated sensing-therapy systems combined with cargo-delivery. However, for biomedical applications, thorough biocompatibility tests of the ND swimmers would be required. Pt and TiO_2 are known as biocompatible and inert materials[33] and the biocompatibility of PS could potentially be improved by surface modification.[34] It will also be important to ensure optical access and reduce the required optical intensities.

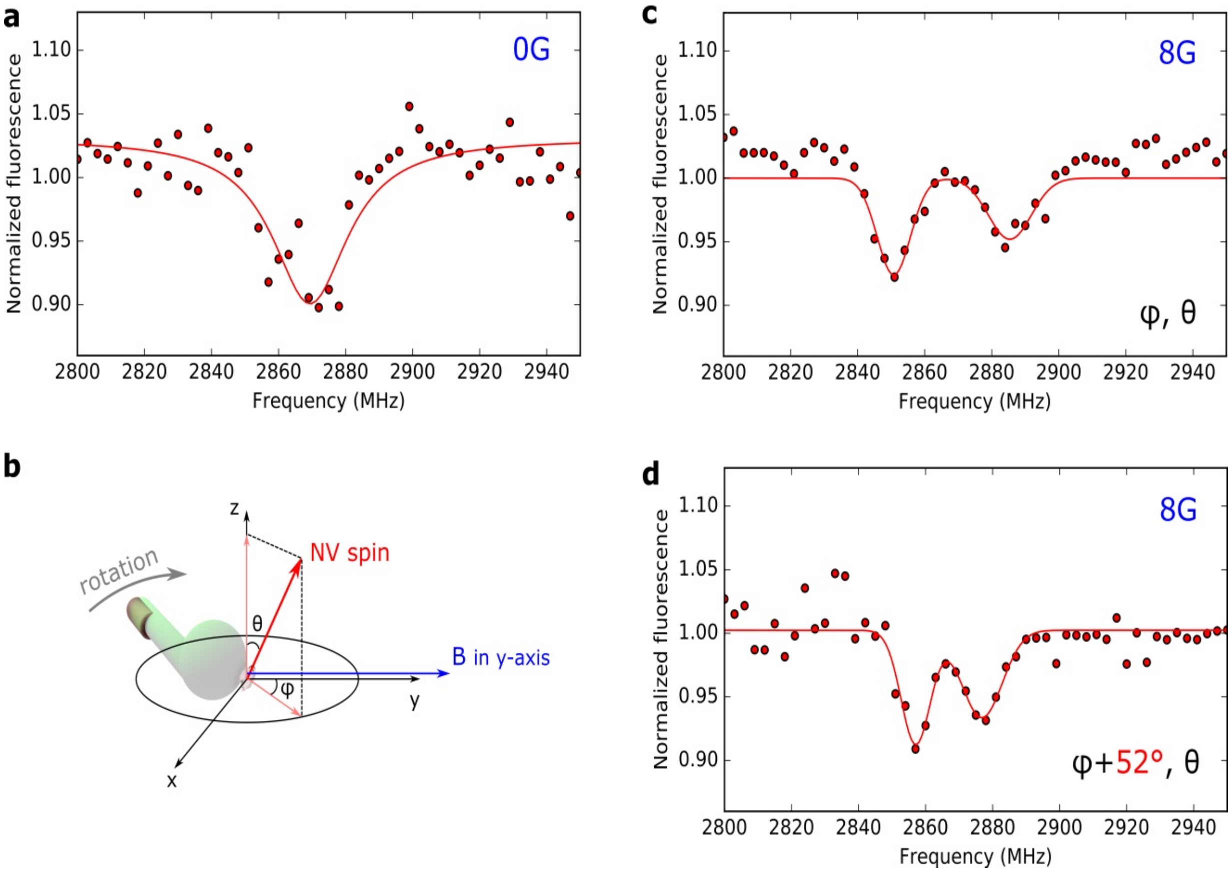

Figure 4.9 Electron spin resonance (ESR) of active ND swimmers. a) Optically detected fluorescence of an ND swimmer (532 nm laser illumination of 100 mW) as a function of the microwave excitation, and associated electron spin resonance (ESR). b) Schematic of NV spin orientation in 3D. c) An ESR signal with a magnetic field of 8 G field applied along the y-axis. d) ESR signal after rotation of same swimmer in same field by 52° in the x–y plane. Image taken from Ref.1.

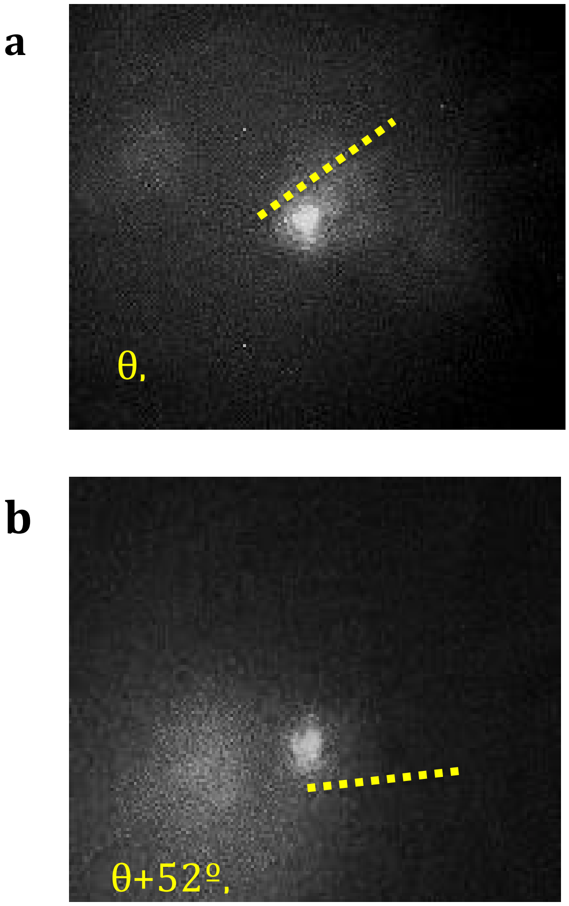

Figure 4.10: Fluorescence images of a ND swimmer with an applied magnetic field of 0.8 mT a) at a given angle of θ and φ with the NV-spin axis and b) after rotation of $\Delta\theta = 52^{0}$.The swimmer orientations in Figures 4.9a and b correspond to ESR peak splits in Figure 4.8 a (33 MHz) and 8b(21 MHz) respectively. Image taken from Ref 1.

4.5 Experimental Section

4.5.1 Sample preparation

Nanodiamonds (40 nm diameter, approx.1 to 4 NV centers) functionalized with carboxylic groups were purchased from Adámas Nanotechnologies. Silicon wafers were piranha cleaned and then functionalized with an amine-silane to impart a positive surface charge. A diluted nano-diamond suspension was spin-coated on the wafer and then dried. Polystyrene (PS) particles were subsequently deposited using a Langmuir-Blodgett trough. The wafer with PS beads was etched with an air-plasma to increase the distances between each PS spheres. The wafer was then loaded in an e-beam evaporator to form anisotropic particles by depositing the microposts onto the colloids using glancing angle deposition (GLAD). After the shadow growth step,[35] the wafer was heated to 90^{0} C for 20 seconds to soften the PS such that the beads bond the underlying ND seeds. Finally, the wafer was sonicated for 10 seconds to release the swimmers into an aqueous solution.

4.5.2 Fluroscence Imaging

A green laser (532 nm) illuminated the sample with a ×100, 1.45 NA oil immersion objective. An iris was placed in the path of the laser to control the diameter of the wide-field laser spot. The fluorescence signal from the NV centers was passed through 637 nm long wave pass filter and collected by an EMCCD. ESR scan was performed by obtaining intensity of the nanodiamond for 1.5 seconds at each scan frequency. A schematic of the setup is shown in Figure 4.11.

4.5.3 Signal processing and tracking

The detected signal from the EMCCD was extracted by fitting a Gaussian function to the ND fluorescence signal and computing the area under the Gaussian curve. A customized MATLAB code extracts the intensity signal and tracks the position of the NDs in successive frames. For the ESR measurements, the raw data from three measurements at the same orientation and magnetic field were first averaged prior fitting.

4.5.4 RF circuit integration

The sample chamber was formed by sandwiching a 1 mm thick quartz slide (top) and a 0.2 mm thick quartz slide (bottom). An antenna was fabricated on the top slide by depositing 50 nm titanium and 1000 nm copper through a 100 μm wide shadow mask. Positive photoresist Ma-P 1205 was coated with a thickness of 5 μm onto the slide and a 1 cm sample chamber was patterned on it. The microwave field was generated with the help of an RF generator, amplified and fed onto the antenna *via* an SMA cable. After transferring a small volume containing the microswimmers, the chamber was sealed at the sides to prevent evaporation.

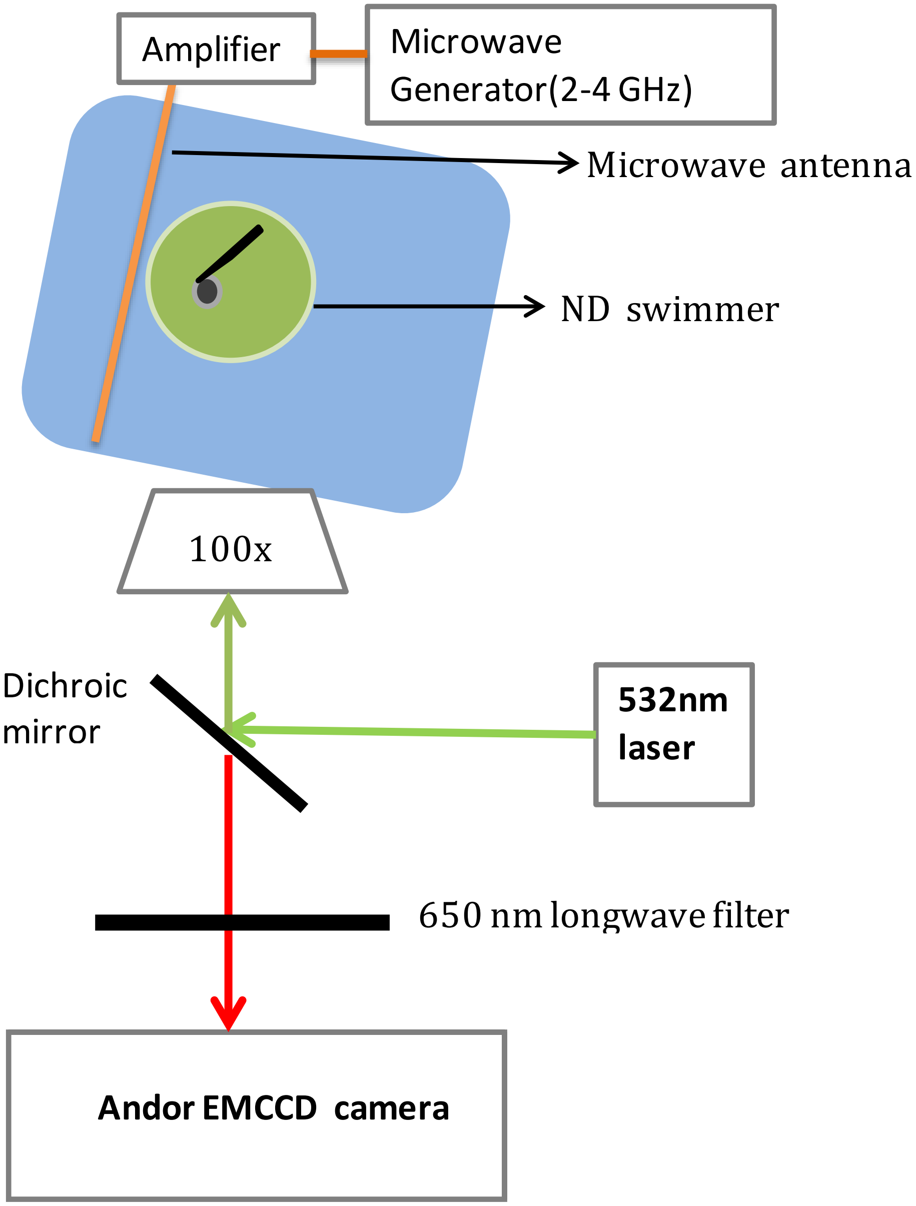

Figure 4.11: Schematic of experimental setup to measure ND swimmer fluorescence.

4.6 References

1. Kim, J. T., Choudhury, U., Jeong, H.-H. & Fischer, P. Nanodiamonds: Nanodiamonds That Swim (Adv. Mater. 30/2017). *Adv. Mater.* **29,** (2017).
2. Neumann, P. *et al.* Quantum register based on coupled electron spins in a room-temperature solid. *Nat. Phys.* **6,** 249–253 (2010).
3. Babinec, T. M. *et al.* A diamond nanowire single-photon source. *Nat. Nanotechnol.* **5,** 195–199 (2010).
4. Balasubramanian, G. *et al.* Nanoscale imaging magnetometry with diamond spins under ambient conditions. *Nature* **455,** 648-U46 (2008).
5. Dolde, F. *et al.* Electric-field sensing using single diamond spins. *Nat. Phys.* **7,** 459–463 (2011).
6. Kucsko, G. *et al.* Nanometre-scale thermometry in a living cell. *Nature* **500,** 54-U71 (2013).
7. Schirhagl, R., Chang, K., Loretz, M. & Degen, C. L. Nitrogen-Vacancy Centers in Diamond: Nanoscale Sensors for Physics and Biology. *Annu. Rev. Phys. Chem. Vol 65* **65,** 83–105 (2014).
8. Igarashi, R. *et al.* Real-Time Background-Free Selective Imaging of Fluorescent Nanodiamonds in Vivo. *Nano Lett.* **12,** 5726–5732 (2012).
9. Haziza, S. *et al.* Fluorescent nanodiamond tracking reveals intraneuronal transport abnormalities induced by brain-disease-related genetic risk factors. *Nat. Nanotechnol.* (2016). doi:10.1038/nnano.2016.260
10. Manus, L. M. *et al.* Gd(III)-Nanodiamond Conjugates for MRI Contrast Enhancement. *Nano Lett.* **10,** 484–489 (2010).
11. Gong, J. X., Steinsultz, N. & Ouyang, M. Nanodiamond-based nanostructures for coupling nitrogen-vacancy centres to metal nanoparticles and semiconductor quantum dots. *Nat. Commun.* **7,** (2016).
12. Neugart, F. *et al.* Dynamics of diamond nanoparticles in solution and cells. *Nano Lett.* **7,** 3588–3591 (2007).
13. Andrich, P. *et al.* Engineered Micro- and Nanoscale Diamonds as Mobile Probes for High-Resolution Sensing in Fluid. *Nano Lett.* **14,** 4959–4964 (2014).

14. Tetienne, J. P. *et al.* Scanning Nanospin Ensemble Microscope for Nanoscale Magnetic and Thermal Imaging. *Nano Lett.* **16,** 326–333 (2016).
15. Ampem-Lassen, E. *et al.* Nano-manipulation of diamond-based single photon sources. *Opt. Express* **17,** 11287–11293 (2009).
16. Rondin, L. *et al.* Stray-field imaging of magnetic vortices with a single diamond spin. *Nat. Commun.* **4,** (2013).
17. Horowitz, V. R., Alemán, B. J., Christle, D. J., Cleland, A. N. & Awschalom, D. D. Electron spin resonance of nitrogen-vacancy centers in optically trapped nanodiamonds. *Proc. Natl. Acad. Sci.* **109,** 13493–13497 (2012).
18. Geiselmann, M. *et al.* Three-dimensional optical manipulation of a single electron spin. *Nat. Nanotechnol.* **8,** 175–179 (2013).
19. Ropp, C. *et al.* Manipulating Quantum Dots to Nanometer Precision by Control of Flow. *Nano Lett.* **10,** 2525–2530 (2010).
20. Kayci, M., Chang, H.-C. & Radenovic, A. Electron Spin Resonance of Nitrogen-Vacancy Defects Embedded in Single Nanodiamonds in an ABEL Trap. *Nano Lett.* **14,** 5335–5341 (2014).
21. Kayci, M. & Radenovic, A. Single florescent nanodiamond in a three dimensional ABEL trap. *Sci. Rep.* **5,** (2015).
22. Mark, A. G., Gibbs, J. G., Lee, T.-C. & Fischer, P. Hybrid nanocolloids with programmed three-dimensional shape and material composition. *Nat. Mater.* **12,** 802–807 (2013).
23. Gibbs, J. G. *et al.* Nanohelices by shadow growth. *Nanoscale* **6,** 9457–9466 (2014).
24. Jiang, H.-R., Yoshinaga, N. & Sano, M. Active Motion of a Janus Particle by Self-Thermophoresis in a Defocused Laser Beam. **105,** 268302 (2010).
25. Kroy, K., Chakraborty, D. & Cichos, F. Hot microswimmers. *Eur. Phys. J. Spec. Top.* **225,** 2207–2225 (2016).
26. Schachoff, R. *et al.* Hot Brownian motion and photophoretic self-propulsion. (2015).
27. Maggi, C., Saglimbeni, F., Dipalo, M., De Angelis, F. & Di Leonardo, R. Micromotors with asymmetric shape that efficiently convert light into work by thermocapillary effects. *Nat. Commun.* **6,** (2015).
28. Buttinoni, I. *et al.* Dynamical Clustering and Phase Separation in Suspensions of Self-Propelled Colloidal Particles. **110,** (2013).

29. Gibbs, J. G. & Zhao, Y. Self-Organized Multiconstituent Catalytic Nanomotors. **6,** 1656–1662 (2010).
30. Lai, N. D., Zheng, D., Treussart, F. & Roch, J.-F. Optical determination and magnetic manipulation of a single nitrogen-vacancy color center in diamond nanocrystal. *Adv. Nat. Sci. Nanosci. Nanotechnol.* **1,** 015014 (2010).
31. Sattayasamitsathit, S. *et al.* Fully Loaded Micromotors for Combinatorial Delivery and Autonomous Release of Cargoes. *Small* **10,** 2830–2833 (2014).
32. Gao, W. & Wang, J. Synthetic micro/nanomotors in drug delivery. *Nanoscale* **6,** 10486–10494 (2014).
33. Karpagavalli, R., Zhou, A., Chellamuthu, P. & Nguyen, K. Corrosion behavior and biocompatibility of nanostructured TiO2 film on Ti6Al4V. *J. Biomed. Mater. Res. A* **83A,** 1087–1095
34. Chen, Y. *et al.* Surface modification and biocompatible improvement of polystyrene film by Ar, O2 and Ar+O2 plasma. *Appl. Surf. Sci.* **265,** 452–457 (2013).
35. Hawkeye, M. M. & Brett, M. J. Glancing angle deposition: Fabrication, properties, and applications of micro- and nanostructured thin films. *J. Vac. Sci. Technol. A* **25,** 1317–1335 (2007).

4.7 Appendix

4.7.1 Mean squared displacement of a self- thermophoretic swimmer

For a spherical self-thermophoretic Janus swimmer with gold coated half, illuminated by a defocused 532 nm laser, the mean squared displacement was derived by Sano et.al.[1] as

$$MSD = 4D\tau_k\left(1 - e^{-\frac{t}{\tau_k}}\right) - \frac{2V^2\bar{\tau}}{\tau_k^{-1}+\tau_r^{-1}} e^{-\frac{t}{\tau_r}} + \frac{2V^2\tau_k}{\tau_k^{-1}+\tau_r^{-1}}\left(1 + \frac{\bar{\tau}}{\tau_r} e^{-\frac{t}{\tau_k}}\right) \qquad \text{(A1)}$$

where $\bar{\tau} = \frac{1}{\tau_k^{-1}-\tau_r^{-1}}$, D is the Brownian diffusion constant and V is the self-propulsion velocity, τ_r is the rotational diffusion time of the colloid, k is the spring constant of the optical confinement and $\tau_k = k_B T/Dk$ is the time constant due to harmonic potential of the laser beam. For time scales much smaller than τ_r and τ_k, the equation can be approximated as

$$MSD = 4Dt + V^2t^2, \qquad \text{(A2)}$$

Equation A2 has been used in the chapter to fit the mean squared displacement between t=0 to 2s.

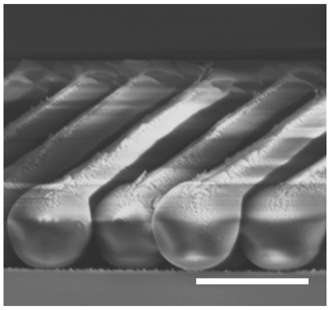

Figure A1. SEM image of GLAD fabricated rotary swimmers on wafer, Scale bar in the image is 1µm.

Additional References

1.Jiang, H.-R., Yoshinaga, N. & Sano, M. Active Motion of a Janus Particle by Self-Thermophoresis in a Defocused Laser Beam. **105,** 268302 (2010).

5 : Chemical nanomotors at the gram scale form a dense active opto-rheological medium

This chapter has been submitted as a manuscript for publication as "Chemical nanomotors at the gram scale form a dense active opto-rheological medium" by Udit Choudhury, Dhruv P.Singh, Tian Qiu and Peer Fischer.[57]

The author performed the microrheology and the macrorheology as well as all particle tracking measurements and analyzed the data. The author was assisted by D.S. in tuning the chemical fuel for the active colloids and by T.Q. in the bulk rheology measurements.

5.1 Introduction

Single particle behaviour and their applications were previously explored in this thesis. The dynamics of individual self-propelled particles and their applications in local sensing was investigated. However, the behaviour of a collection of many such colloids remains largely unexplored experimentally. Theory predicts interesting collective properties could emerge out of interactions between such self-propelled colloids, especially if the suspension in dense. This chapter investigates how the collective behaviour of many such active colloids can influence the bulk properties of the colloid-fluid suspension, for instance the viscosity of the suspension. The rheological properties of a colloidal suspension are a function of the concentration of the colloids and their interactions. While suspensions of passive colloids are well studied and have been shown to form crystals, gels, and glasses, examples of energy-consuming "active" colloidal suspensions are still largely unexplored. Active suspensions of biological matter, such as motile bacteria or dense mixtures of active actin-motor-protein mixtures have, respectively, revealed superfluid-like and gel-like states. An attractive inanimate system for active matter are chemically self-propelled particles. It has so far been challenging to use these swimming particles at high enough densities to affect the bulk material properties of the suspension. Here, photo-chemically propelled shape assymetric titanium dioxide nanomotors, obtained in large quantities, and are demonstrated to self-organize to make an active medium. Further, the active particles can be obtained in very large quantities, as they are no longer Janus particles, and the suspension shows an activity-dependent 10-fold reversible change in its bulk viscosity.

5.2 Motivation

A characteristic feature of living systems is the presence of non-equilibrium assembly as a route to self-organize. For example bacterial colonies can self-organize into rotating swarms[1], and microtubule–motor protein systems form aster like formations.[2] These processes are driven by the dissipation of a chemical fuel, such as ATP, to gain motility and induce structural changes.[3–6] This permits the system to evolve into different non-equilibrium states as a function of the fuel consumption. Such a system is, in the case of a fluid-like medium, known as an "active" or "living" suspension.[7] A key feature of these active systems is that they can give rise to interesting collective effects that arise due to interactions between the active units as well as through hydrodynamics at high density.[8,9] For instance, the collective motility of a bacterial suspension can change the bulk viscosity of the suspension,[10,11] and ATP-driven actin-myosin systems show changes in the microstructural phase and its rheological properties that control the mechanical properties of cells.[12,13] Examples of such large scale collective behaviors in synthetic active colloids have been experimentally demonstrated at the macroscale in electrically powered Quincke “rollers”[9,14] and metal-coated colloidal particles[8,15] or by magnetic colloids[16,17]. However, it has been challenging to realize bulk active systems at high density with artificial chemically active particles. Further, recent theoretical studies have predicted more complex properties in active colloids at high density, such as the reentrant phase behavior, dynamic pattern formation, active turbulence that have the potential to form new active materials, but there have been very few suitable experimental systems that permit one to observe these phenomena[18–22]. Moreover, most of the conventional active colloidal systems are either confined to two dimensions or are operated at low densities, and hence are unable to drive changes in bulk. Here, it is demonstrated that inorganic chemically-active nanomotors can be used to prepare a dense, bulk active medium, whose viscosity can be controlled by the activity of its constituents. This is, to the best of our knowledge, a first demonstration of collective behavior of synthetic active matter giving rise to a change in bulk material property. Thus a novel opto-rheological medium and a route for truly large-scale applications of synthetic active chemical motors is realized.

Inorganic chemically active colloids or nanomotors convert fuel available in the solvent to self-propel. [23,24] Their behavior at a single particle level has been intensely studied in the literature in the last decade.[25,26] Recent experimental and theoretical studies have also demonstrated how multiple particles can interact and thereby influence each other's behavior.[21,27,28] Under non-equilibrium conditions the dynamics, particle-interactions and structural rearrangements are expected to play a crucial role in determining the bulk properties of the suspension. While several model synthetic active systems are known, including catalytically active Janus particles,[23,28–36] it has thus far been difficult to obtain truly large numbers of chemical motors to form an active medium and operate them stably for an extended period of time.[37]

Here in this study, it is experimentally demonstrated that titanium dioxide (TiO_2) powders, which can readily be obtained in large quantities, form active nanomotors[38] by virtue of their inherent shape-anisotropy and in addition give rise to collective self-organization. A biocompatible fuel that scavenges oxygen (a reaction product) is used and makes the reaction system stable at high particle densities. The photo-catalytic activity of the TiO_2 gives rise to local concentration gradients around the nanoparticles that produce diffusiophoretic effects, which makes them self-propel as well as induce attraction to other nearby particles. Further, microstructural rearrangements of the active suspension are found to underlie the change in its viscosity and consequently the bulk viscosity of the active suspension can be changed reversibly with light by an order of magnitude.

5.3 Results

Most self-propelling motors that move due to chemical reactions rely on Janus particles, that have a reactive and non-reactive material on each of the particle's two faces[12]. Physical vapor deposition (PVD) and electro-chemical anodic aluminum oxide (AAO) templated synthesis are commonly used to fabricate Janus particles,[29,30,35,39] but the overall yield is always low. PVD requires a monolayer of colloidal particles, which limits the quantity of colloids that can be fabricated to milligrams. Electrodeposition growth in an anodic aluminum oxide (AAO) template offers an alternative, however, the choice of materials is limited to a few conducting materials. Since the growth occurs on a thin membrane, it is similarly limited in the amount it can produce. In addition, pickering emulsion or biphasic electrochemistry based techniques had been used for bulk synthesis of Janus colloids.[40,41]

Here, a simpler alternate strategy to obtain large numbers of catalytically active self-propelling particles is employed. The natural shape anisotropy found in the irregularly shaped-powder particle gives rise to self-phoresis.[38,42] Commercially available anatase TiO_2 powder particles (Figure 5.1a) possess the shape anisotropy and self-propel in the presence of a reactive fuel. The anatase TiO_2 colloids used herein have an irregular shape (Figure 5.1b) and a median diameter of 400nm (Figure 5.1c). As a fuel, an aqueous mixture of TEMPOL (4-hydroxy-2,2,6,6-tetramethylpiperidin-1-oxyl)[34,43] is used. Unlike, the fuels hydrogen peroxide, hydrazine, or quinone, which are unstable and hazardous chemicals, Tempol can be handled in large scales and is biocompatible.[44] Since Tempol is also an oxygen scavenger it suppresses the formation of gaseous bubbles and keeps the reaction mixture stable for long periods of time. On illuminating the suspension with UV light, TiO_2 produces electron-hole pairs. The holes react with hydroxide ions to produce hydroxyl radicals. TEMPOL reacts with the radicals and is converted to TEMPONE (4-oxo-hydroxy-2,2,6,6-tetramethylpiperidin-1-oxyl). Oxygen is consumed in the reaction.[45] Since, the reaction takes place at the surface of the TiO_2 particle, any asymmetry in the particles' shape[38] creates a asymmetric local chemical gradient across the colloid and causes self-phoresis (Figs. 5.1d and 5.1e).[12,46,47] It is seen that without light (UV 365 nm), that is in the absence of activity the particles exhibit Brownian motion (Fig. 5.1d) and then upon illumination they start to self-propel (Fig. 5.1e). The corresponding enhanced diffusivity under UV illumination is plotted in Figure 5.1f and a particle speed of 3.2 μm/s is measured. This result establishes that the powder particle is "active" and a chemical motor.

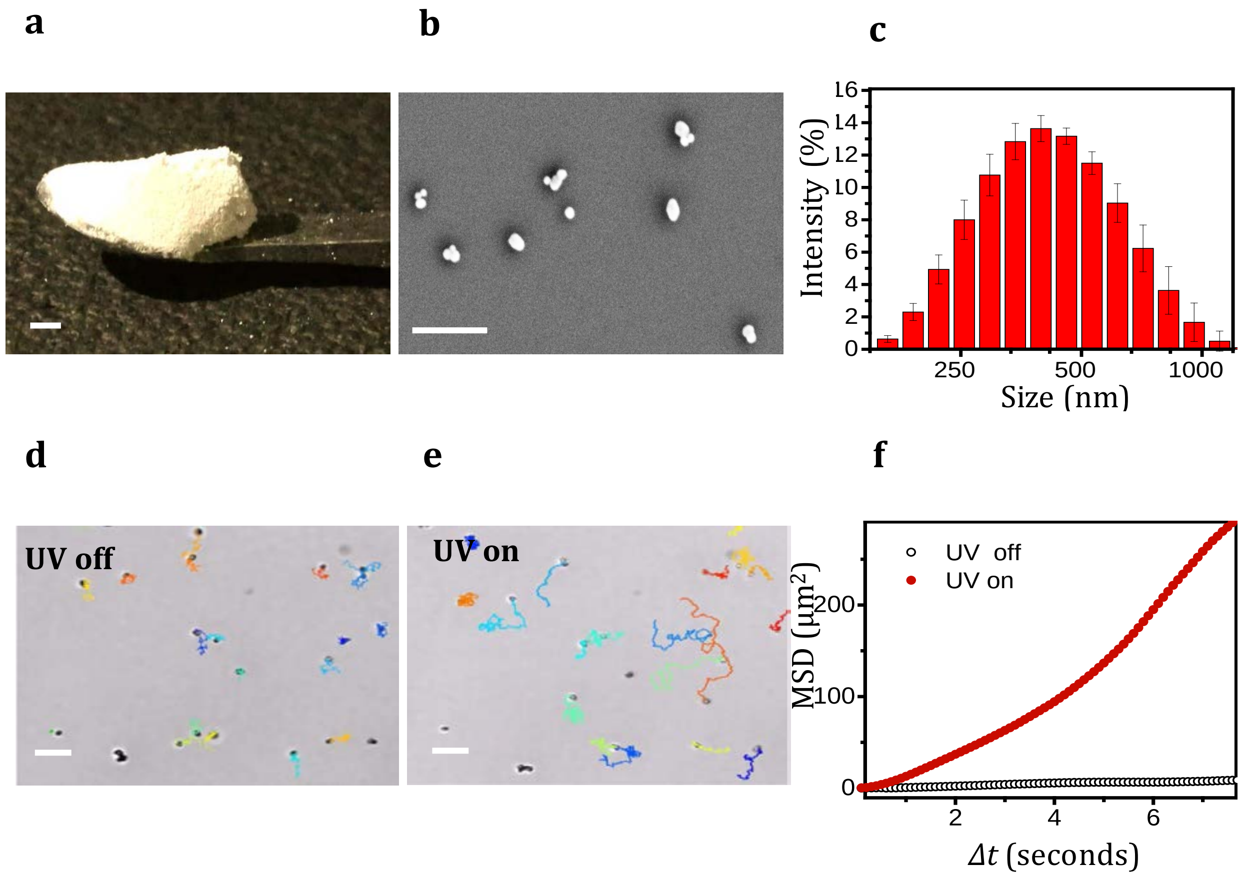

Figure 5.1: Motion of shape asymmetric TiO_2 colloids. a) Image of anatase commercial TiO_2 powder. Scale bar is 1 mm. b) SEM image of TiO_2 colloids showing the asymmetric shape of the colloids. Scale bar is 1μm. c) Dynamic Light scattering (DLS) measurement of the colloidal size distribution. d) Brownian motion without UV illumination. e) Active motion of colloids on illumination by UV light. Scale bar is 5μm. Colored lines indicate trajectory of particles for 20s. f) Mean Squared Displacement (MSD) of colloids with and without activity. Image taken from Ref. 57

5.3.1 Non-equilibrium micro-structural evolution

In addition to the motion, the TiO_2 particles, once active, experience attractive interactions.[28] The origin of interactions can be phoretic in nature[21] where continuous dissipation of fuel makes a chemical sink that leads to the clustering of the particles. These lead to reversible dynamic aggregates that can be tuned by the light intensity[47](Figure 5.2). In order to increase the base viscosity of the suspension, fumed silica is added. The active TiO_2 colloids do not interact with fumed silica and move freely in the suspension. Fumed silica also helps in slowing sedimentation, which is important for bulk-rheological measurements. The activity and dynamic clustering of the TiO_2 colloids depends on the light intensity. Figure 5.3 shows the behavior of the active TiO_2 colloids and fumed silica mixtures in 500 mM Tempol solutions under low (20mW/cm^2, Figures 5.3 a and b) and high (200 mW/cm^2, Figures 5.3 c and d) UV illumination. It is observed that at low UV intensity (Figures 5.3 a and b), and hence low activity and interparticle interactions, the mixture shows dynamic clustering behavior with unstable aggregates that dynamically form and dissociate. The small unstable aggregates form a fluctuating dispersed medium. The same mixture at a higher light intensity forms larger stable aggregates that self-organize towards an arrested network of colloids (Figured 5.3 c and d). On switching off the activity (turning the UV light off) all mixtures return to their nascent state (Figure 5.4).

Differential dynamic microscopy (DDM)[48–51]was used to study the dynamics with bright-field microscopy and extract the structural evolution from the videos. Assuming that the local density of the particles, to be related to the detected intensity distribution, the dynamic image structure function $D(q,\Delta t)$ for the wave vector of magnitude q and the lag time Δt is calculated from the radially averaged Fourier transform of the difference images $\Delta I(\boldsymbol{x},\Delta t)$ separated by a lag time Δt

$$D(q,\Delta t) = \langle \left| \Delta \hat{I}(\boldsymbol{q},\Delta t) \right|^2 \rangle \qquad (1)$$

$\Delta \hat{I}(\boldsymbol{q},\Delta t)$ is the Fourier transform of difference image $\Delta I(\boldsymbol{x},\Delta t)$. The intermediate scattering function $f(q,\Delta t)$ can be extracted from $D(q,\Delta t)$ (see methods for details).

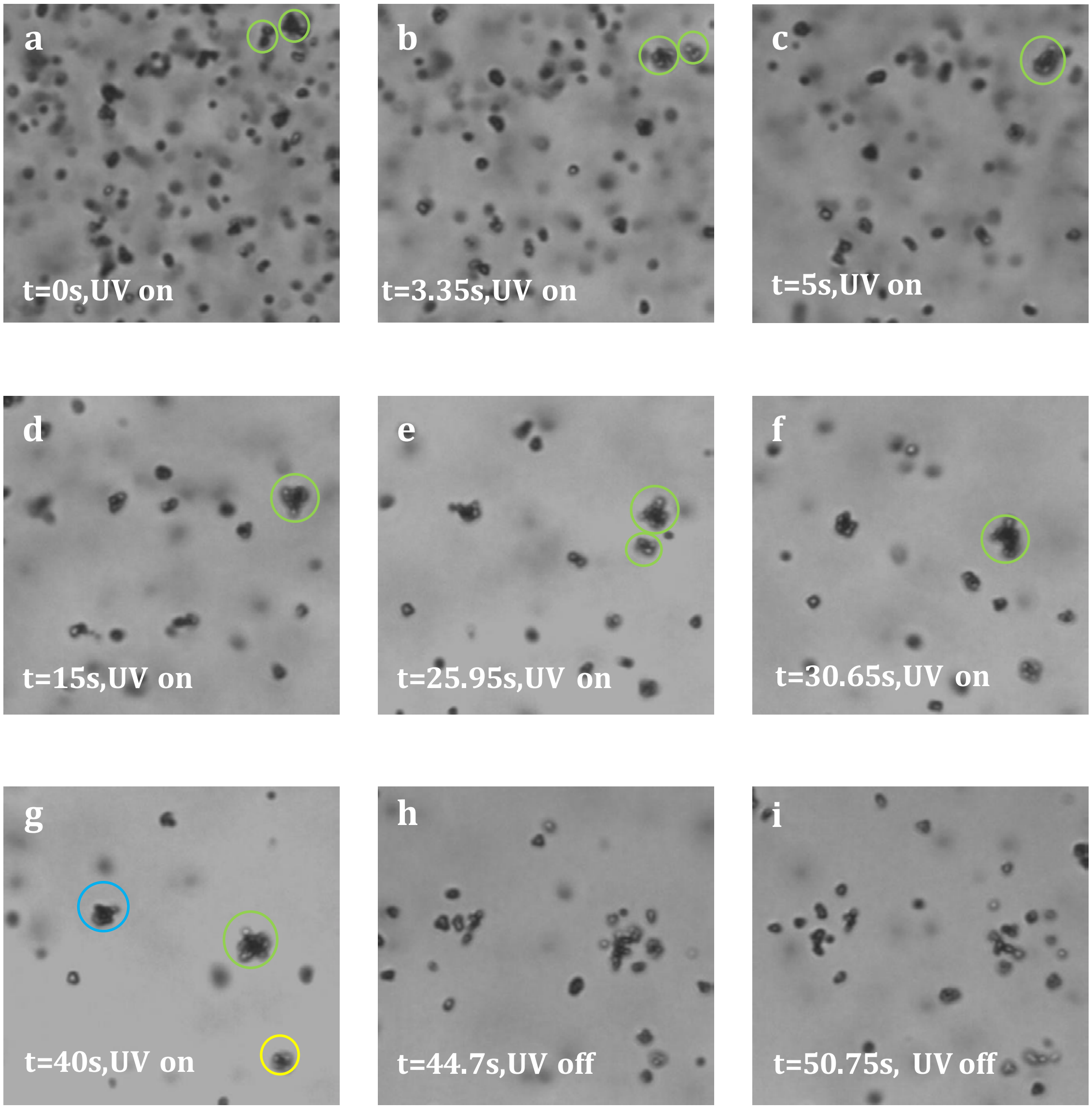

Figure 5.2 : Reversible clustering of Titania nanomotors in aqueous fuel. a-g) shows cluster formation. Green circle tracks growth of an individual cluster by collecting more particles through time. g) Similar neighboring clusters circled in blue and yellow. h,i) Upon turning UV off, the clusters break as the particle loses its activity and returns to Brownian state.

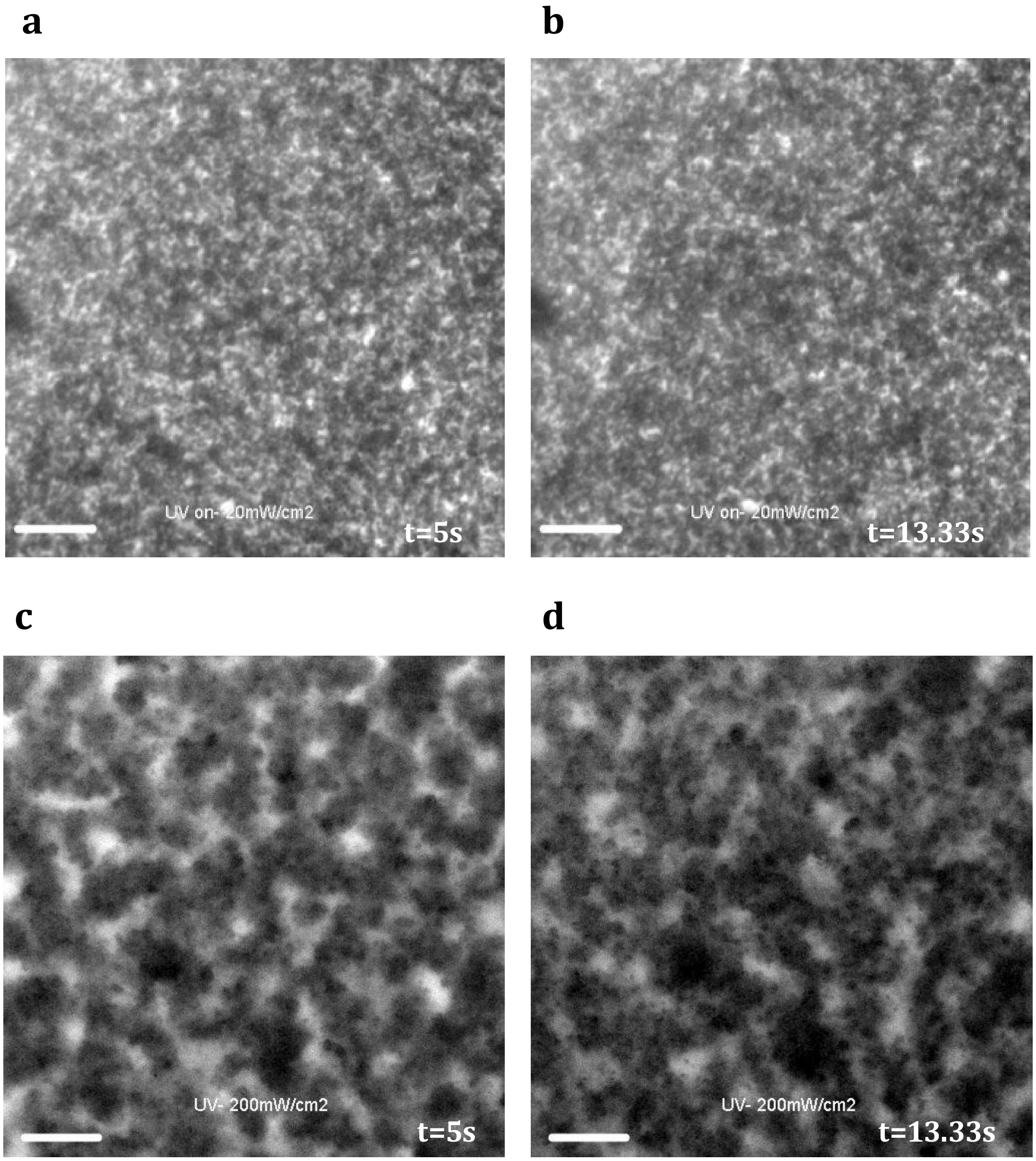

Figure 5.3 : Optical images of 3.5% fumed silica with 2.5% TiO_2 in 500mM Tempol. a and b) shows images at low light intensity (UV 20mW/cm^2). A dispersed phase with small aggregates is observed. c and d) shows images at high light intensity (UV -200mW/cm^2). A clustered network phase is observed, Scale bar is 5 μm.

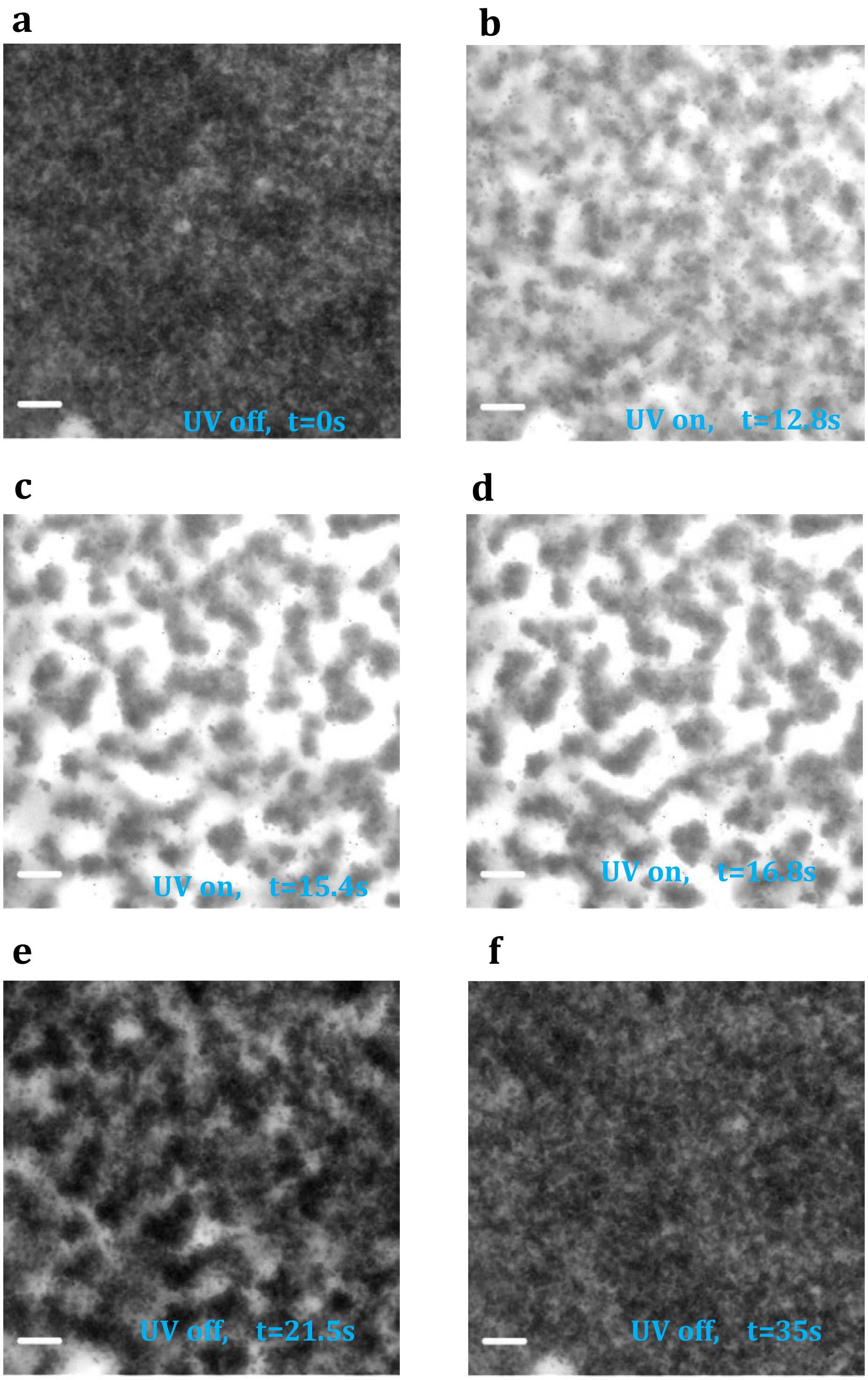

Figure 5.4: Reversible phase change. a) Brownian dispersed state of mixture . b-e) UV on between from 12.8s to 21.5s . Clustered network forms f) Mixture goes back to nascent state on turning off UV.

The function $f(q, \Delta t)$ describes the particle configuration in the images separated by lagtimes Δt and thus can be related to the motion of the particles on length scales of 2π/q. Videos of 10s at 100fps are recorded and the decay dynamics of $f(q, \Delta t)$ for q=4.8 μm^{-1} is compared. As shown in Figure 5.5c , the decay of $f(q, \Delta t)$ is faster at low light intensity (I=20 mW/cm^2) than for higher light intensity (I=200 mW/cm^2). Decay of $f(q, \Delta t)$ with a larger slope indicates faster particle rearrangements. At lower light intensities with dynamic clustering, the structure loses its integrity and relaxes faster. At higher intensity with larger inter-particle attractive interactions the structure progresses towards a clustered arrested-like state which is maintained for longer lag times. Hence, $f(q, \Delta t)$ decays with a smaller slope. The dynamics at lower density of active particles was also investigated. A suspension of 3.5% (v/v) fumed silica with 1.25% (v/v) TiO_2 was prepared. A dispersed phase remains at lower light intensities (Figure 5.6a), while at high light intensity, small isolated cluster phase emerges due to competition between[10,50] attraction and self-propulsion (Figure 5.6b).

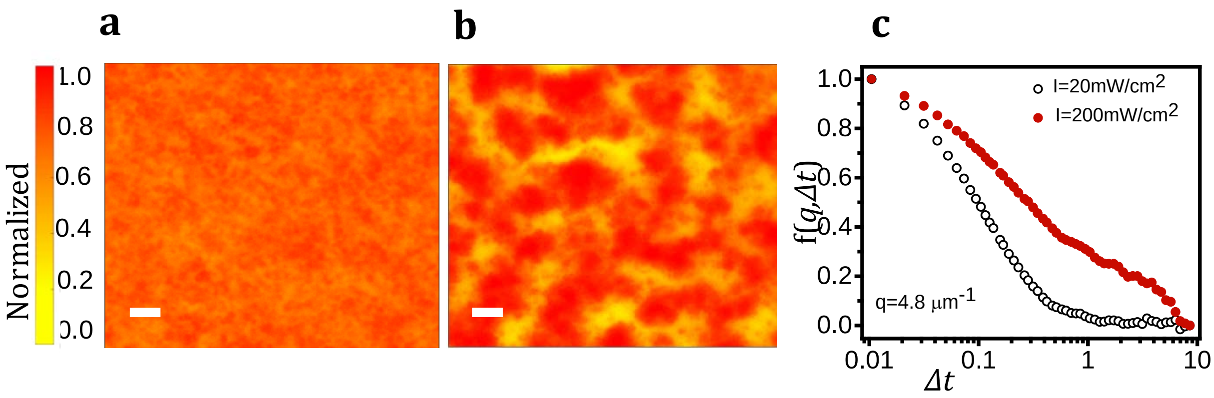

Figure 5.5: Phase behavior of mixtures of 3.5% (v/v) fumed silica with 2.5% (v/v) TiO_2 in 500mM Tempol. Microscope image of the mixture at a) low (20mW/cm^2) and b) high (200 mW/cm^2) light intensity. Scale bar is 5μm in both figures. c) Corresponding relaxation of the intermediate scattering function $f(q, \Delta t)$ at q=4.8 μm^{-1}. Image taken from Ref. 57.

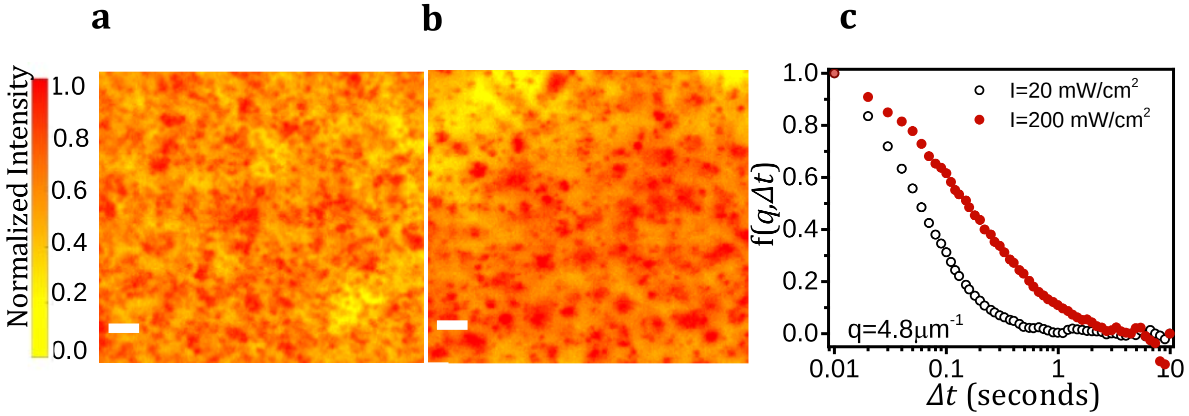

Figure 5.6: Phase behavior of mixtures. Microscope image of mixture of 3.5% (v/v) fumed silica with 1.25% (v/v) TiO$_2$ in 500mM Tempol at a) low (20mW/cm^2) and b) high (200 mW/cm^2) light intensity. Scale bar is 5μm in both Figures 2a and 2b. c) Corresponding relaxation of the intermediate scattering function $f(q,\Delta t)$ at q=4.8μm^{-1} . Image taken from Ref. 57.

From these measurements, it is clear that the microstructural dynamics of this active colloidal suspension can be controlled by tuning the activity (by adjusting the UV light intensity). Further, in the absence of activity the suspension reverts to its Brownian state. It is expected that this change will be reflected in the micro-structure and viscosity of the suspension.

5.3.2 Micro-rheology of an active suspension

The network strength of the active suspension as a function of activity (light intensity) can be elucidated by magnetic micro-rheology.[10,52] Figure 5.7 shows a magnetic microprobe rotating in an applied field at 0.5Hz, while the UV light is on. As the microstructure changes with time from a dispersed to an arrested phase, the microprobe gets jammed, slows down and ultimately stops. A constant torque τ rotates the magnetic microprobe

$$\tau = m \times \boldsymbol{B}, \tag{2}$$

where, m is the magnetic moment of the micro stir-bar and $\boldsymbol{B}$ is the applied magnetic field. The viscous drag

$$\tau_{drag} = X|\eta^*|\Omega, \tag{3}$$

acts on the bar, where $|\eta^*|$ is the viscosity, X is the shape factor and Ω the angular velocity of the stir-bar. Here m, X is predetermined by the dimensions and magnetization, while $|\eta^*|$ can be determined from the measurement istelf. When the two torques balance, then the bar rotates at the same frequency as the applied magnetic field. Here, magnetic-micro-rheology is used to investigate the change in viscosity in the active suspension. After the UV light was on for 30 seconds, the magnetic micro stir-bar is rotated at 0.5 Hz and the amplitude of the applied magnetic field that is needed to rotate the bar at a particular light intensity is determined.

Figure 5.8 shows a schematic of the setup, and an image of the magnetic microprobe (see Methods for fabrication details) in the suspension. $|\eta_o^*|$ is the magnitude of viscosity of the passive suspension. The ratio of active to passive local viscosity ($|\eta^*|/|\eta_o^*|$) is plotted as a function of light intensity (activity). It is seen that the local viscosity increases with light intensity and then tends to saturate. With activity, the interparticle interaction forces increase and the tendency of the particles to form a stable clustered network will therefore also increase. This is reflected in the increased torque required to rotate the microprobe. Consequently, the local viscosity of the suspension increases and is observed to change 8-fold as a function of light intensity.

From these measurements, it follows that activity can locally induce a microstructural change, which has been theoretically predicted for active media, but has thus far not been observed[20]. Because of the nature of our active particles, now, it is easy to scale up the volume of the suspension to examine bulk effects.

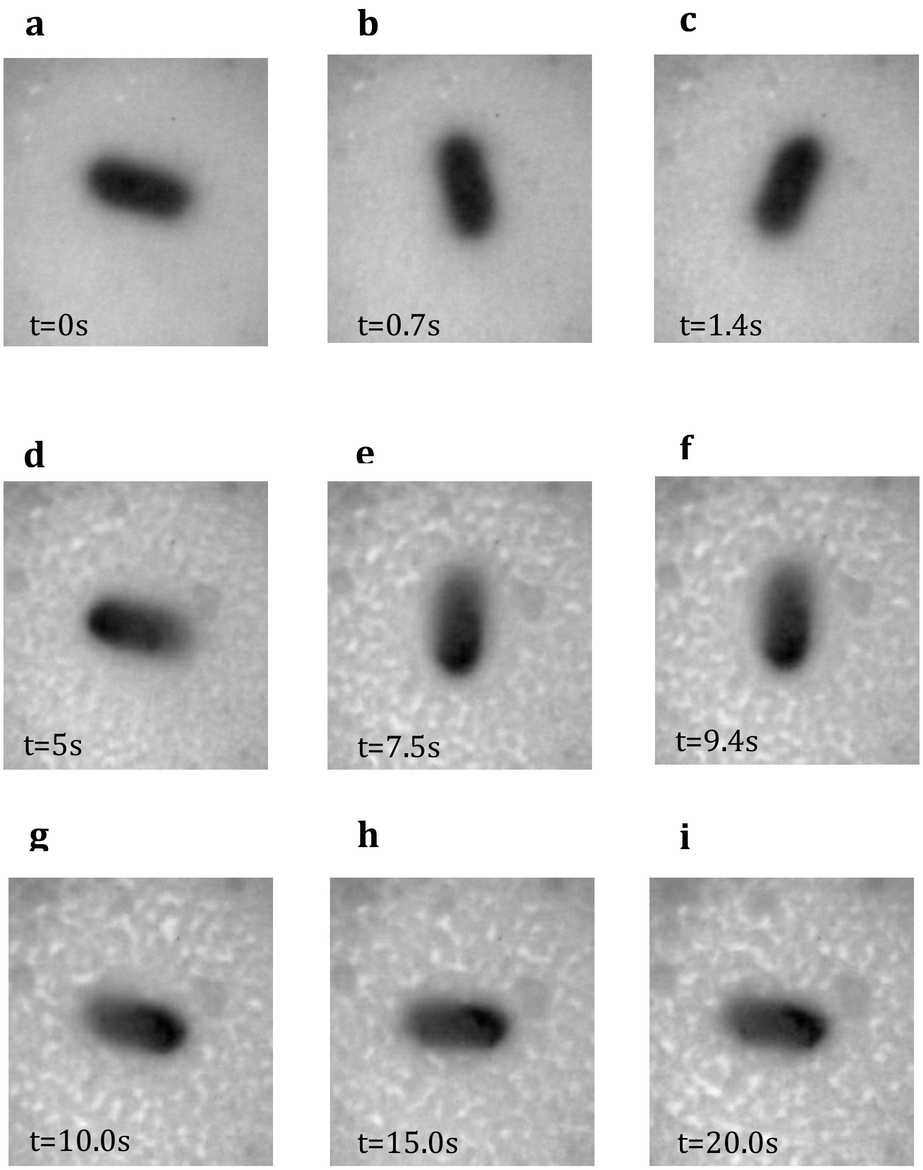

Figure 5.7: Rotation of magnetic micro probe. A suspension of 3.5% fumed silica with 2.5% TiO_2 and 500 mM Tempol is illuminated through the objective with the magnetic probe positioned in the center of the coil setup. a-g) The position of the probe at different points of time. g-i) The bar stops moving after t=10.0s as it gets jammed in the network. UV is on throughout the experiment. The phase change from dispersed to arrested could be seen in the background.

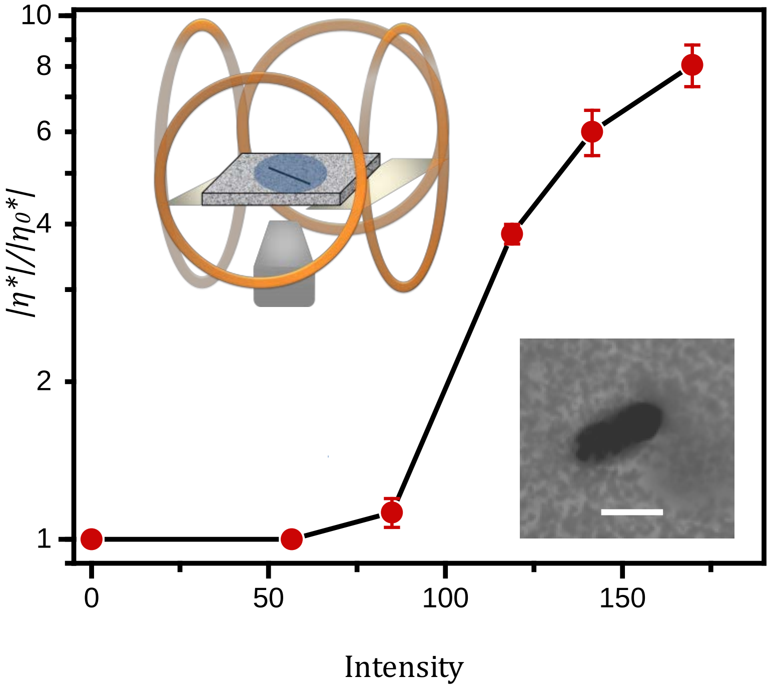

Figure 5.8: Micro-rheology. Schematic of the Helmholtz coil setup used to drive the magnetic micro stir-bar. The local viscosity increases with light intensity. Inset shows magnetic microprobe as observed through microscope. Scale bar is 50µm. Image taken from Ref. 57.

5.3.3 Bulk rheology of an active suspension

Firstly, with long time 200s oscillatory strain experiments, it was confirmed that sedimentation does not play a major role during the course of the measurements (Figure 5.9). Next, to ensure that the structural change does occur throughout the suspension, images at different heights inside the sample where the particles are far away from the walls were recorded. In order to facilitate imaging, the particle density was lowered to 0.6% (v/v) TiO_2. The illumination from below provides an additional upward force[46] on the active colloids due to self-shadowing effect of the colloids. Figure 5.10a shows positions of local clusters after illumination for 180s at different heights.

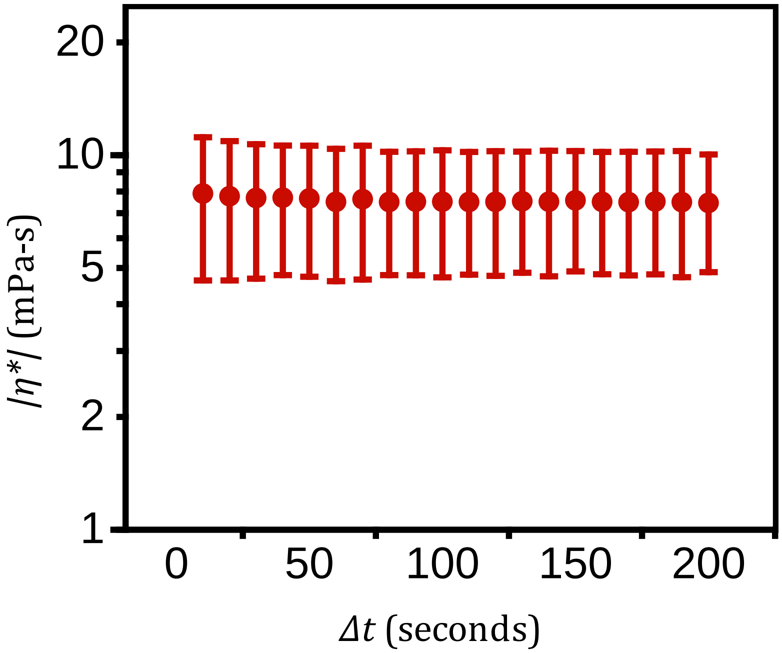

Figure 5.9 : Rheology of the passive suspension. Control experiment with oscillation strain test with UV light off for 200 seconds. The viscosity of the suspension remains constant with time, as expected. Image taken from Ref. 57.

A commercial rheometer with a 35mm parallel plate geometry was then used in its oscillation mode to measure the bulk rheological properties. A custom made UV LED array (see Methods) illuminates the sample through a glass window from the bottom. The spatial arrangement of the LED array is designed to ensure uniform illumination in the measurement area. The same suspension (3.5% fumed silica with 2.5% TiO_2 with 500mM TEMPOL) as in the micro-rheological measurements was used for bulk rheology. First, an oscillatory strain amplitude (γ) sweep at a frequency of 1 Hz was conducted for both active (with UV) and passive (without UV illumination) suspensions (see Figure 5.10b). The passive suspension shows a low viscosity. The slight decrease in the viscosity at higher strain rates could be due to a slight loss in internal structure as the entangled fumed silica particles get pulled apart.[53] In contrast, a much more dramatic effect is seen when the suspension is active under UV illumination.

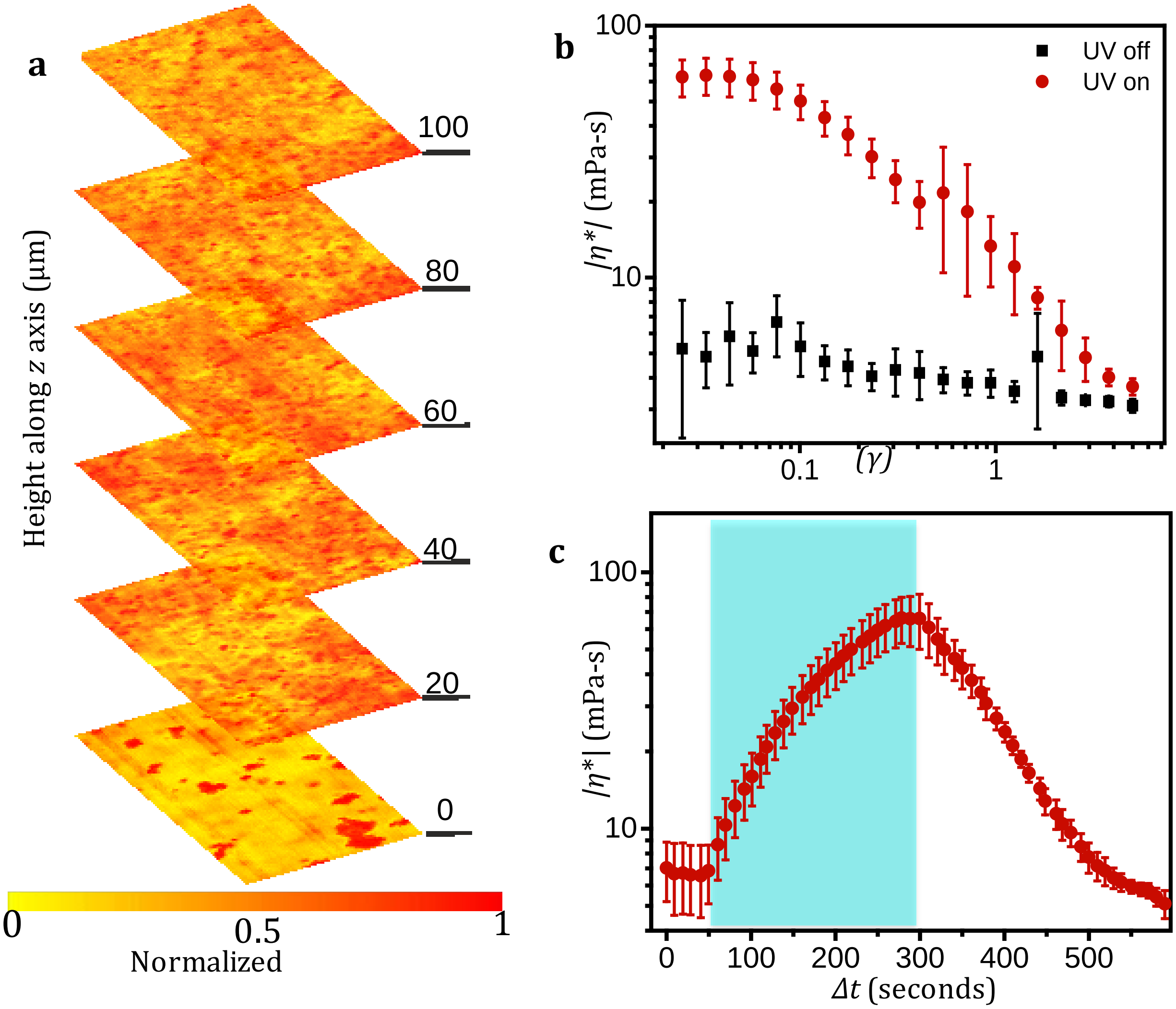

Figure 5.10: Bulk rheology measurements. a) Optical images (35μm x 50μm) at different positions in the suspension. b) Strain amplitude sweep at 1 Hz for active (solid red) and passive suspensions (solid black) measured in a 100μm thick fluid layer. c) Viscosity as a function of time measured with a strain of 0.1, at a frequency of 1Hz in a 100μm gap. The blue shaded zone indicates the illumination time. UV intensity in a and b is 200 mW/cm^2. Image taken from Ref. 57.

At low strain amplitudes the viscosity of the suspension increases by an order of magnitude. At higher strain amplitudes, the viscosity decays to the viscosity of the passive mixture. From our microrheological observations, one understands that the dispersed TiO_2 colloids form local clusters that provide additional structural stability to the suspension. This results in a viscosity increase at low strain amplitudes. At large amplitudes the networks break and the viscosity approaches that of the passive suspension. Up to γ=0.1, i.e. 10% strain, the viscosity remains independent of the strain amplitude. In order to show that the active state is fully reversible, measurements at a fixed strain amplitude γ=0.1 and constant frequency of 1 Hz was performed and the UV light was switched on for a period of time. Figure 5.10c shows that the viscosity is low in the initial 70 seconds without activity (UV illumination) and then sharply increases as the system is active. As the light is switched off the activity ceases and the viscosity returns to its nascent state. The viscoelastic modulus |G*| also follows a similar trend as can be seen in Figure 5.11.

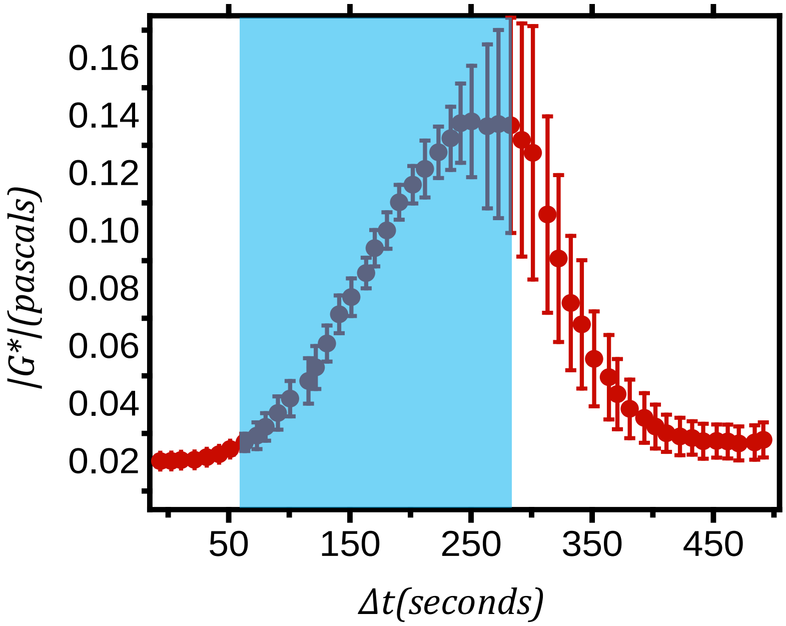

Figure 5.11: Measurement of viscoelastic modulus |G*|.Viscoelastic modulus for sample under oscillation strain of 0.1 at 1Hz is seen to change with UV illumination. Image taken from Ref. 57.

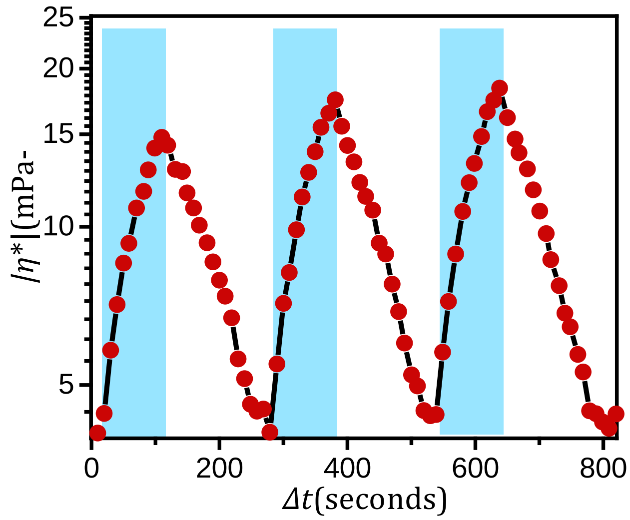

Figure 5.12: Demonstration of the optorheological properties. The viscosity is seen to change with UV illumination. Blue shaded region indicates that the UV illumination is on for 100 seconds. Image taken from Ref. 57.

Thus, the active suspension undergoes a completely reversible change in viscosity by an order of magnitude. Furthermore, by cycling the UV illumination, the viscosity can be changed multiple times as shown in Figure 5.12.

5.4 Discussion

In this chapter, an active suspension that consumes fuel from its solvent to form an opto-rheological medium was demonstrated. The suspension undergoes dynamical and structural transformations leading to reversible changes in its rheological properties. The active unit of this system is a shape-asymmetric anatase TiO_2 colloidal powder particle that self-propels in a Tempol solution. At higher densities the system shows clustering and aggregation leading to network formation and finally an arrested state. Further, being light controlled, the activity can be externally tuned. Micro-rheology confirms that microstructural changes underlie the viscosity changes of the active suspension. Measurements conducted in a bulk rheometer demonstrate that the active colloids cause reversible, optically-triggered viscosity changes. Thus the collective behavior of the system of active colloids determines the bulk properties of the suspension. In contrast to biological active suspensions, that show a dynamic steady state, the present system progresses toward an arrested steady state at high activity (light illumination). Since the base viscosity of the passive suspension can be tuned by increasing the particle density of the passive (fumed silica) component of the suspension, or the particle density of the active titania colloids, the system can be extended to show reversible changes in different viscosity regimes, depending on the desired applications. Further, since the powders are readily available at potentially kilogram quantities, these active chemical motors can now be used at large scales, which opens up new possibilities in engineering applications of chemical motors and in forming novel active materials.

5.5 Experimental Methods

5.5.1 Colloids

TiO_2 colloids were obtained from US Research Nano-Materials Inc., fumed silica (Aerosil 150) from Evonik, and TEMPOL from Sigma Aldrich.

5.5.2 Dynamic Differential Microscopy

Videos were recorded at 100fps after 15 seconds of UV light illumination. The detailed theory of DDM has been described in References 48, 49 and 51. The image structure function $D(q,\Delta t)$ can be further expressed as[48,54]

$$D(q,\Delta t) = A(q)(1 - f(q,\Delta t) + B(q), \tag{4}$$

where $A(q)$ is the image transfer function, $B(q)$ is any additional camera noise and $f(q,\Delta t)$ is the intermediate scattering function. At short timescales, $f(q,\Delta t) = 1$,[54,55] such that $D(q,\Delta t \to 0) = B(q)$ and at long time scales , $f(q,\Delta t) = 0$, hence $D(q, \Delta t \to \infty) = A(q) + B(q)$. From $D(q,\Delta t)$ in the long term and short term limits, one can deduce the constants A(q) and B(q). Matlab algorithm developed by Hegelson *et al.*[56] was used to process the images and calculate $D(q, \Delta t)$. For fixed q, we can thus estimate $A(q)$ and $B(q)$ from the data and obtain $f(q,\Delta t)$.

5.5.3 Micro-Rheology

The micro stir-bars were fabricated by first lithographically patterning a 7.5um layer of photoresist (SU-8). The SU-8 bar was then coated with a Ni layer of 300nm by e-beam evaporation. The samples were kept at an angle of 45 degrees during e-beam deposition to create a shadow adjacent to each SU-8 structure. This ensured easy release of the structures from the wafer post fabrication. The micro stir-bars were magnetized in an electromagnet and then placed in the suspension. A custom-made 3-axis Helmholtz coil[52] was placed in a microscope and used to apply the magnetic fields for the micro-rheology measurements. Bright field illumination from above was used to image the sample while UV light was incident through the imaging objective from below.

5.5.4 Bulk Rheology

Bulk rheology measurements were performed in a HAAKE MARS III rheometer. A 35mm parallel plate geometry with a 100 µm gap was used for all the measurements. The bottom plate was made of glass (1mm thick) to allow for UV illumination. Four UV (365nm) LEDs with an area of 6.3mm x 6.3mm and an output optical power of 5 W were mounted on a custom-made water-cooled aluminum plate and arranged to provide uniform illumination at the center of the sample. To minimize radiant heating from the LEDs, air-cooling was directed at the underside of the rheometer glass window. All rheological measurements were conducted in a custom-made humidity chamber to minimize evaporative losses during measurements.

5.6 References

1. Lin, S.-N., Lo, W.-C. & Lo, C.-J. Dynamics of self-organized rotating spiral-coils in bacterial swarms. *Soft Matter* **10,** 760–766 (2014).
2. Ndlec, F. J., Surrey, T., Maggs, A. C. & Leibler, S. Self-organization of microtubules and motors. *Nature* **389,** 305–308 (1997).
3. Schmoller, K. M., Fernández, P., Arevalo, R. C., Blair, D. L. & Bausch, A. R. Cyclic hardening in bundled actin networks. *Nat. Commun.* **1,** 134 (2010).
4. Köhler, S., Schaller, V. & Bausch, A. R. Structure formation in active networks. *Nat. Mater.* **10,** 462 (2011).
5. Silva, M. S. e *et al.* Active multistage coarsening of actin networks driven by myosin motors. *Proc. Natl. Acad. Sci.* **108,** 9408–9413 (2011).
6. Alvarado, J., Sheinman, M., Sharma, A., MacKintosh, F. C. & Koenderink, G. H. Molecular motors robustly drive active gels to a critically connected state. *Nat. Phys.* **9,** 591 (2013).
7. Boekhoven, J., Hendriksen, W. E., Koper, G. J. M., Eelkema, R. & Esch, J. H. van. Transient assembly of active materials fueled by a chemical reaction. *Science* **349,** 1075–1079 (2015).
8. Yan, J. *et al.* Reconfiguring active particles by electrostatic imbalance. *Nat. Mater.* **15,** 1095–1099 (2016).
9. Bricard, A., Caussin, J.-B., Desreumaux, N., Dauchot, O. & Bartolo, D. Emergence of macroscopic directed motion in populations of motile colloids. *Nature* **503,** 95–98 (2013).
10. Sokolov, A. & Aranson, I. S. Reduction of Viscosity in Suspension of Swimming Bacteria. *Phys. Rev. Lett.* **103,** 148101 (2009).
11. López, H. M., Gachelin, J., Douarche, C., Auradou, H. & Clément, E. Turning Bacteria Suspensions into Superfluids. *Phys. Rev. Lett.* **115,** 028301 (2015).
12. Illien, P., Golestanian, R. & Sen, A. 'Fuelled' motion: phoretic motility and collective behaviour of active colloids. *Chem. Soc. Rev.* **46,** 5508–5518 (2017).
13. Schuppler, M., Keber, F. C., Kröger, M. & Bausch, A. R. Boundaries steer the contraction of active gels. *Nat. Commun.* **7,** 13120 (2016).

14. Bricard, A. *et al.* Emergent vortices in populations of colloidal rollers. *Nat. Commun.* **6,** 7470 (2015).
15. Ohiri, U. *et al.* Reconfigurable engineered motile semiconductor microparticles. *Nat. Commun.* **9,** 1791 (2018).
16. Driscoll, M. *et al.* Unstable fronts and motile structures formed by microrollers. *Nat. Phys.* **13,** 375–379 (2017).
17. Kokot, G. *et al.* Active turbulence in a gas of self-assembled spinners. *Proc. Natl. Acad. Sci.* **114,** 12870–12875 (2017).
18. Stenhammar, J., Wittkowski, R., Marenduzzo, D. & Cates, M. E. Activity-Induced Phase Separation and Self-Assembly in Mixtures of Active and Passive Particles. *Phys. Rev. Lett.* **114,** 018301 (2015).
19. Hemingway, E. J. *et al.* Active Viscoelastic Matter: From Bacterial Drag Reduction to Turbulent Solids. *Phys. Rev. Lett.* **114,** 098302 (2015).
20. Redner, G. S., Baskaran, A. & Hagan, M. F. Reentrant phase behavior in active colloids with attraction. *Phys. Rev. E* **88,** 012305 (2013).
21. Pohl, O. & Stark, H. Dynamic Clustering and Chemotactic Collapse of Self-Phoretic Active Particles. *Phys. Rev. Lett.* **112,** 238303 (2014).
22. Liebchen, B., Marenduzzo, D., Pagonabarraga, I. & Cates, M. E. Clustering and Pattern Formation in Chemorepulsive Active Colloids. *Phys. Rev. Lett.* **115,** 258301 (2015).
23. Gao, W., Pei, A., Dong, R. & Wang, J. Catalytic Iridium-Based Janus Micromotors Powered by Ultralow Levels of Chemical Fuels. *J. Am. Chem. Soc.* **136,** 2276–2279 (2014).
24. Howse, J. R. *et al.* Self-Motile Colloidal Particles: From Directed Propulsion to Random Walk. *Phys. Rev. Lett.* **99,** 048102 (2007).
25. Dong, R., Zhang, Q., Gao, W., Pei, A. & Ren, B. Highly Efficient Light-Driven TiO2–Au Janus Micromotors. *ACS Nano* **10,** 839–844 (2016).
26. Palacci, J. *et al.* Artificial rheotaxis. *Sci. Adv.* **1,** e1400214 (2015).
27. Takatori, S. C., Dier, R. D., Vermant, J. & Brady, J. F. Acoustic trapping of active matter. *Nat. Commun.* **7,** 10694 (2016).
28. Palacci, J., Sacanna, S., Steinberg, A. P., Pine, D. J. & Chaikin, P. M. Living Crystals of Light-Activated Colloidal Surfers. *Science* **339,** 936–940 (2013).

29. Lee, T.-C. *et al.* Self-Propelling Nanomotors in the Presence of Strong Brownian Forces. *Nano Lett.* **14,** 2407–2412 (2014).
30. Nourhani, A., Brown, D., Pletzer, N. & Gibbs, J. G. Engineering Contactless Particle–Particle Interactions in Active Microswimmers. *Adv. Mater.* **29,** 1703910 (2017).
31. Choudhury, U., Soler, L., G. Gibbs, J., Sanchez, S. & Fischer, P. Surface roughness-induced speed increase for active Janus micromotors. *Chem. Commun.* **51,** 8660–8663 (2015).
32. Gao, W., Pei, A., Feng, X., Hennessy, C. & Wang, J. Organized Self-Assembly of Janus Micromotors with Hydrophobic Hemispheres. **135,** 998–1001 (2013).
33. Mei, Y., Solovev, A. A., Sanchez, S. & Schmidt, O. G. Rolled-up nanotech on polymers: from basic perception to self-propelled catalytic microengines. *Chem. Soc. Rev.* **40,** 2109–2119 (2011).
34. Hong, Y., Diaz, M., Córdova-Figueroa, U. M. & Sen, A. Light-Driven Titanium-Dioxide-Based Reversible Microfireworks and Micromotor/Micropump Systems. *Adv. Funct. Mater.* **20,** 1568–1576 (2010).
35. Dai, B. *et al.* Programmable artificial phototactic microswimmer. *Nat. Nanotechnol.* **11,** 1087 (2016).
36. Kim, J. T., Choudhury, U., Jeong, H.-H. & Fischer, P. Nanodiamonds That Swim. *Adv. Mater.* **29,** 1701024 (2017).
37. Palacci, J., Cottin-Bizonne, C., Ybert, C. & Bocquet, L. Sedimentation and Effective Temperature of Active Colloidal Suspensions. *Phys. Rev. Lett.* **105,** 088304 (2010).
38. Shklyaev, S., Brady, J. F. & Córdova-Figueroa, U. M. Non-spherical osmotic motor: chemical sailing. *J. Fluid Mech.* **748,** 488–520 (2014).
39. Jang, B. *et al.* Catalytic Locomotion of Core–Shell Nanowire Motors. *ACS Nano* **10,** 9983–9991 (2016).
40. Hong, L., Jiang, S. & Granick, S. Simple Method to Produce Janus Colloidal Particles in Large Quantity. *Langmuir* **22,** 9495–9499 (2006).
41. Loget, G., Roche, J. & Kuhn, A. True Bulk Synthesis of Janus Objects by Bipolar Electrochemistry. *Adv. Mater.* **24,** 5111–5116 (2012).
42. Michelin, S. & Lauga, E. Autophoretic locomotion from geometric asymmetry. *Eur. Phys. J. E* **38,** 7 (2015).

43. Li, F. *et al.* Microbiome remodelling leads to inhibition of intestinal farnesoid X receptor signalling and decreased obesity. *Nat. Commun.* **4,** 2384 (2013).
44. Cai, J. *et al.* The Anti-Oxidant Drug Tempol Promotes Functional Metabolic Changes in the Gut Microbiota. *J. Proteome Res.* **15,** 563–571 (2016).
45. Marshall, D. L. *et al.* Oxidation of 4-substituted TEMPO derivatives reveals modifications at the 1- and 4-positions. *Org. Biomol. Chem.* **9,** 4936–4947 (2011).
46. Singh Dhruv P., Uspal William E., Popescu Mihail N., Wilson Laurence G. & Fischer Peer. Photogravitactic Microswimmers. *Adv. Funct. Mater.* **0,** 1706660 (2018).
47. Singh, D. P., Choudhury, U., Fischer, P. & Mark, A. G. Non-Equilibrium Assembly of Light-Activated Colloidal Mixtures. *Adv. Mater.* **29,** 1701328 (2017).
48. Cerbino, R. & Trappe, V. Differential Dynamic Microscopy: Probing Wave Vector Dependent Dynamics with a Microscope. *Phys. Rev. Lett.* **100,** 188102 (2008).
49. Ferri, F. *et al.* Kinetics of colloidal fractal aggregation by differential dynamic microscopy. *Eur. Phys. J. Spec. Top.* **199,** 139–148 (2011).
50. Wittmeier, A., Leeth Holterhoff, A., Johnson, J. & Gibbs, J. G. Rotational Analysis of Spherical, Optically Anisotropic Janus Particles by Dynamic Microscopy. *Langmuir* **31,** 10402–10410 (2015).
51. Bayles, A. V., Squires, T. M. & Helgeson, M. E. Dark-field differential dynamic microscopy. *Soft Matter* **12,** 2440–2452 (2016).
52. Jeong, H.-H. *et al.* Active Nanorheology with Plasmonics. *Nano Lett.* **16,** 4887–4894 (2016).
53. Amiri, A., Øye, G. & Sjöblom, J. Influence of pH, high salinity and particle concentration on stability and rheological properties of aqueous suspensions of fumed silica. *Colloids Surf. Physicochem. Eng. Asp.* **349,** 43–54 (2009).
54. Martinez, V. A. *et al.* Differential Dynamic Microscopy: A High-Throughput Method for Characterizing the Motility of Microorganisms. *Biophys. J.* **103,** 1637–1647 (2012).
55. Germain, D., Leocmach, M. & Gibaud, T. Differential dynamic microscopy to characterize Brownian motion and bacteria motility. *Am. J. Phys.* **84,** 202–210 (2016).
56. https://engineering.ucsb.edu/~helgeson/ddm.html
57. Choudhury, U., Singh, Dhruv P., Qiu, T.,& Fischer,P.,. *XX,***XX,**XXXX(XXXX) *(under review)*

6 : Conclusions

6.1 Conclusions

Research on active colloids has convincingly established the dynamics of colloids. Further, many different model systems of realizing self-propulsion have been demonstrated. This has resulted in experimental and theoretical studies of non-equilibrium systems – model model systems which can be used to understand phenomena related to locomotion, swimming and swarming that are generally associated with living systems. This thesis has focused on aspects of the motion of colloids and has explored certain uses for active matter.

In particular, the thesis has demonstrated how the speed of catalytic micro-motors can be increased by increasing the effective surface area of the Janus colloids, and how a complex topography changes the dynamics of the self-propelled colloids. The colloids move due to the decomposition of hydrogen peroxide which limits their usefulness. Still, the method used to increase the speed in this thesis and hence the catalytic activity of the colloids is general, and can therefore be applied to other materials and surfaces. The method could also be useful in the fabrication of metal electrodes and can lead to significant enhancement in turnover rates of catalytic reactions.

The demonstration of a sensor functionality in self-thermophoretic swimmers circumvent the challenges of bio-compatibility, since it relies on local heating rather than reactions in hydrogen peroxide fuels. Hence, this approach is in principle suitable for *in vitro* biological applications. However, experiments with nano-diamond sensors remain challenging as the required microwave radiation for spin transitions are emitted from linear antenna that can only deliver powers in its close vicinity (<100 μm). Hence, a better antenna design that can deliver microwave power to the entire sample volume and specimen must be developed. Also, since the experimentally observed change in optical intensity is around 10%, the system is susceptible to external noises and is only well-suited for optically transparent mediums. Nevertheless, future experiments with self-thermophoretic swimmers could be used for *in vitro* monitoring of local properties of biological samples, e.g. living cells, with nanodiamond-coupled swimmers.

A major result of this thesis is the demonstration of a material property that arises and depends on the self-organization of active colloids. An active opto-rheological medium with a biocompatible chemical fuel is realized. While the viscosity change that has been demonstrated in the active opto-rheological medium can only be maintained at lower strain rates, the system is based on inexpensive commercially available products, and can thus be useful for a number of applications involving colloidal materials. Future research could focus on the development of analogous active materials for higher strain rates. Nevertheless, the system is shown to be chemically stable, and can be prepared in large quantities, and can therefore serve as a model system for studying collective behavior of active colloids at high density.

Many questions remain to be addressed in the field of self-propelled and active colloids – both in the study of single particle dynamics as well as the collective behavior of colloids. Single particle dynamics studies have, for instance, so far been limited to two-dimensional space. One may ask the question if colloidal motion and self-organization in three dimensional space can be suitably controlled, for instance by optical holography techniques to fabricate three dimensional microstructures, or by chemical means *via* chemotaxis. With regards, to collective dynamics, it will interesting to see if inanimate active colloids can demonstrate the rich collective phenomenology observed in cells and microorganisms. Active matter can also be investigated from the point of view of fundamental statistical physics, where one can ask several questions like how does directed collective motion arise from random motion of individual units and what role does hydrodynamic and chemical coupling play in such phenomena. Further, the thesis has adopted an experimental approach to study active matter. Simulations of the active materials had been studied in literature before. However, with the experimental techniques presented in the thesis it becomes possible to compare simulations with real experiments and design new properties in active matter. Hence, future studies can involve detailed simulations the experimental active material system presented in the thesis to fabricate materials with designer properties. Finally, one major goal of the field is to develop colloids that can be used as 'intelligent autonomous' particles, for instance as drug carriers for targeted delivery into specific cells.

7 : Summary

7.1 Summary

In this thesis, the behavior of active particles spanning from single particle dynamics to collective behavior of many particles is explored. Active colloids are out-of equilibrium systems that have been studied extensively over the past 15 years. This thesis addresses several phenomena that arise in the field of active colloids.

The first chapter gives a brief introduction to mechanisms of propulsion of active colloids and related fabrication techniques.

In the second chapter, a simple technique to increase the speed of catalytic motors is discussed. Janus-particles, half coated with a catalyst are the most widely studied system of self-propelled colloids. To fabricate these particles, physical vapor deposition techniques, such as sputtering, are used, and a catalyst (typically Platinum) is evaporated onto the colloids inside a vacuum chamber. Here, it is examined if one can use nano-structuring to increase the speed of the Janus particles. A simple technique of introducing a thin oxide underlayer underneath the catalyst is demonstrated. The oxide layer creates nanoscale roughness on the surface of the colloids. By depositing metal platinum catalyst on top of the oxide, the active rough catalytic surface has a higher surface area than if it had been deposited on the smooth surface of the particle. Hence, a higher turnover rate due to an effectively larger surface area is expected. This results in a higher speed of the catalytic motors and a four-fold enhancement of their speed is observed.

In the third chapter of this thesis, the motion of active self-propelled colloids on a complex surface topography is studied. The model surface consists of a close-packed monolayer of spherical particles. This model system shows similarities to the periodic potential found in atomic diffusion. The self-propelled colloids could be considered as “model adatoms” to understand basic physics of atomic diffusion process. The slow micron scale dynamics of the colloids permit observation by simple optical microscopy and simplifies measuring otherwise challenging surface diffusion process. On two-dimensional crystalline surfaces, at low fuel concentrations, sub-diffusive behavior is observed. However, as the fuel concentration was increased, the active colloids could easily hop from one lattice site to the next and freely diffuse, although with a lower diffusion coefficient compared to a planar substrate. The dynamics of activated diffusion of colloids on surfaces was studied and compared to a theoretical model.

In the fourth chapter, an application of active colloids in the field of nanoscale sensing is described. Here, for biocompatibility and ease of integration into the experimental setup, a self-thermophoretic rather than a chemically-active colloid is used. By coupling a fluorescent nano-diamond on the tip of the colloid, a swimming hybrid structure was fabricated. The fluorescence stems from a nitrogen vacancy center in the nano-diamond and is exceedingly sensitive to temperature and local electro-magnetic fields. The colloid-coupled NV center was excited with a laser at 532 nm and the fluorescence was observed between 637-750nm. The colloid was also equipped with a small metallic patch, such that the same 532 nm laser could locally heat the colloid and hence the fluid near the colloid. This self-thermophoretic process propelled the microstructure and made a micro-swimmer that could be manipulated with light. The shape of colloid was designed by glancing angled vapor deposition technique, so that it could perform rotary or translatory motion. Electron spin resonance measurements on the NV center attached to a rotary swimmer were used to detect the magnitude and direction of an externally applied magnetic field. Thus, a microscale self-thermophoretic “compass” capable of sensing local magnetic field with NV center was realized. Future applications of such swimmer-sensor can include sensing of local physical properties in biological fluids.

In the final results chapter, an active opto-rheological suspension is demonstrated. Here, the collective behavior of a dense active suspension of self-propelling (chemically-active) colloids was studied. The single unit of the suspension is a shape-asymmetric anatase titania colloid that is powered by the photochemical decomposition of an aqueous fuel to self-propel and interact with neighboring particles. Since, the catalytic reaction is light controlled; the properties of the suspension could be tuned with light. By increasing the activity (or the light intensity), the suspension makes a microstructural transition from a fluctuating state to an arrested state. The microstructural change translates into change in viscosity of the suspension. Magnetic micro-rheology was used to measure the change of viscosity of the chemically-active suspension and an 8-fold increase in the local viscosity was observed. Next, the suspension was transferred to a commercial rheometer to investigate the bulk properties of this active medium. A reversible 10-fold increase of the suspension’s viscosity was demonstrated. Further, the viscosity could be changed multiple times by switching the light on and off. It is thought that this presents a first demonstration of the collective behavior of synthetic active colloids giving rise to a change of a bulk material property. This study opens up possibilities for the large scale application of active colloids and for the development of novel materials that are based on non-equilibrium physics.

In the concluding sixth chapter, the contributions of the thesis were evaluated briefly and possible future directions are discussed. Future studies can lead to both fundamental insight regarding the behavior of active particles, and to applications of active matter.

8 : Samenvatting

8.1 Samenvatting

(Translated to Dutch by Prof.Andreas Herrmann)

In dit proefschrift wordt het gedrag van actieve deeltjes onderzocht, variërend van single particle dynamics tot collectief gedrag van veel deeltjes. Actieve colloïden zijn niet-evenwichtssystemen die de afgelopen 15 jaar uitgebreid zijn bestudeerd. Dit proefschrift behandelt een aantal fenomenen die zich voordoen op het gebied van actieve colloïden.

Het eerste hoofdstuk geeft een korte inleiding over mechanismen van voortstuwing van actieve colloïden en gerelateerde fabricagetechnieken.

In het tweede hoofdstuk wordt een eenvoudige techniek besproken om de snelheid van katalytische motoren te verhogen. Janus-deeltjes, half gecoat met een katalysator, zijn het meest bestudeerde systeem van zelfvoortbewegende colloïden. Voor het vervaardigen van deze deeltjes worden fysische dampafzettingstechnieken, zoals sputteren, gebruikt en wordt een katalysator (typisch platina) op de colloïden binnen een vacuümkamer verdampt. Hier wordt onderzocht of nano-structurering kan worden gebruikt om de snelheid van de Janus-deeltjes te verhogen. Een eenvoudige techniek voor het introduceren van een dunne oxide-onderlaag onder de katalysator wordt gedemonstreerd. De oxidelaag creëert ruwheid op het oppervlak van de colloïden op de nanoschaal. Door het afzetten van een metaalplatinakatalysator bovenop het oxide heeft het actieve ruwe katalytische oppervlak een groter specifiek oppervlak dan wanneer het op het gladde oppervlak van het deeltje was afgezet. Daarom wordt een hogere omloopsnelheid verwacht door een effectief groter oppervlak. Dit resulteert in een hogere snelheid van de katalytische motoren en een viervoudige verbetering van hun snelheid wordt waargenomen.

In het derde hoofdstuk van dit proefschrift wordt de beweging van actieve zelfrijdende colloïden op een complexe oppervlaktetopografie bestudeerd. Het modeloppervlak bestaat uit een dichte monolaag van bolvormige deeltjes. Dit modelsysteem vertoont overeenkomsten met het periodieke potentiaal dat wordt gevonden bij atomaire diffusie. De zelfvoortbewegende colloïden kunnen worden beschouwd als "modeladatomen" om de basisfysica van het atomaire diffusieproces te begrijpen. De langzame dynamiek op de micronschaal van de colloïden maakt observatie mogelijk met behulp van eenvoudige optische microscopie en vereenvoudigt het meten van een anders uitdagend proces van oppervlaktediffusie. Op tweedimensionale kristallijne oppervlakken wordt bij lage brandstofconcentraties sub-diffusief gedrag waargenomen. Naarmate echter de brandstofconcentratie toenam, konden de actieve colloïden gemakkelijk van de ene positie op het rooster naar de volgende springen en vrij diffunderen, hoewel met een lagere diffusiecoëfficiënt vergeleken met een vlak substraat. De dynamiek van geactiveerde diffusie van colloïden op oppervlakken werd bestudeerd en vergeleken met een theoretisch model.

In het vierde hoofdstuk wordt een toepassing van actieve colloïden op het gebied van analyse op de nanoschaal beschreven. Hier wordt voor biocompatibiliteit en gemak van integratie in de experimentele opstelling een zelf-thermophoretisch in plaats van een chemisch actief colloïde gebruikt. Door een fluorescerende nanodiamant aan het uiteinde van het colloïde te koppelen, werd een zwemmende hybride structuur vervaardigd. De fluorescentie komt voort uit een vacante stikstofpositie in de nanodiamant en is buitengewoon gevoelig voor temperatuur en lokale elektromagnetische velden. Het colloïde-gekoppelde NV-centrum werd geëxciteerd met een laser op 532 nm en de fluorescentie werd waargenomen tussen 637-750 nm. Het colloïd was ook uitgerust met een klein metalen regio, zodat dezelfde 532 nm-laser plaatselijk het colloïde en dus het vloeistof nabij het colloïde kon verwarmen. Dit zelf-thermophoretische proces dreef de microstructuur aan en maakte een micro-zwemmer die met licht kon worden gemanipuleerd. De vorm van het colloïde werd ontworpen door een dampafzettingstechniek onder een hoek, zodat deze roterende of translerende beweging kon uitvoeren. Elektron-spinresonantiemetingen op het NV-centrum bevestigd aan een roterende zwemmer werden gebruikt om de grootte en richting van een extern aangelegd magnetisch veld te detecteren. Zo werd een microscopisch zelfthermoforetisch "kompas" gerealiseerd dat in staat is om lokaal magnetisch veld met NV-centrum te detecteren. Toekomstige toepassingen van een dergelijke zwemsensor kunnen het waarnemen van lokale fysische eigenschappen in biologische vloeistoffen omvatten

In het laatste hoofdstuk met resultaten wordt een actieve opto-reologische suspensie gedemonstreerd. Hier werd het collectieve gedrag van een dichte actieve suspensie van zichzelf voortstuwende (chemisch actieve) colloïden bestudeerd. De eenheid van de suspensie is een vorm-asymmetrisch anataas-titania-colloïd dat wordt aangedreven door de fotochemische ontleding van een waterige brandstof om zichzelf voort te bewegen en interactie met naburige deeltjes te vertonen. Omdat de katalytische reactie licht gecontroleerd is kunnen de eigenschappen van de suspensie worden afgestemd met licht. Door de activiteit (of de lichtintensiteit) te vergroten, maakt de suspensie een microstructurele overgang van een fluctuerende toestand naar een stopgezette toestand. De microstructurele verandering vertaalt zich in verandering in viscositeit van de suspensie. Magnetische micro-rheologie werd gebruikt om de verandering van de viscositeit van de chemisch actieve suspensie te meten en een 8-voudige toename van de lokale viscositeit werd waargenomen. Vervolgens werd de suspensie overgebracht naar een commerciële reometer om de bulkeigenschappen van dit actieve medium te onderzoeken. Een reversibele 10-voudige toename van de viscositeit van de suspensie werd aangetoond. Verder zou de viscositeit meerdere keren kunnen worden veranderd door het licht aan en uit te schakelen. Men denkt dat dit een eerste demonstratie is van het collectieve gedrag van synthetische actieve colloïden die aanleiding geven tot een verandering van een eigenschap van bulkmateriaal. Deze studie opent mogelijkheden voor de grootschalige toepassing van actieve colloïden en voor de ontwikkeling van nieuwe materialen die gebaseerd zijn op niet-evenwichtsfysica.

In het afsluitende zesde hoofdstuk werden de bijdragen van het proefschrift kort geëvalueerd en mogelijke toekomstige richtingen besproken. Toekomstige studies kunnen leiden tot zowel fundamenteel inzicht met betrekking tot het gedrag van actieve deeltjes als toepassingen van actieve stoffen.

9 : Curriculum Vitae and Publications

Curriculum Vitae

Udit Choudhury

Heisenbergstrasse 3
Stuttgart -70569,Germany

Tel : (+49)15215714055
E-mail: choudhury@is.mpg.de

Research

Nov 2012 – January 2018	PhD student in Materials Science at the Max Planck Institute for Intelligent Systems, Stuttgart, Germany and in The University of Groningen, Netherlands. Advisor: Prof. Peer Fischer (MPI, Germany, Nov 2012-present) and Prof. Andreas Hermann (RUG, Netherlands, July 2015-present)
Feb 2012 - Sep 2012	Research Assistant in Propulsion Physiology lab in the Rowland Institute at Harvard University, MA, USA Advisor: Dr.Chris Richards
Jan 2010 - Jan 2012	Graduate Assistant at the Engineering, Science and Mechanics Department, Virginia Tech, USA

Education

Jan 2010 - Jan 2012	Master of Science in Engineering Mechanics, Virginia Tech, USA, Advisor : Prof. Daniel M Dudek Thesis "Dynamic Mechanical Properties of Cockroach (*Periplaneta Americana)* Resilin" G.P.A. : 3.96/4.00
July 2005 - June 2009	Bachelor of Mechanical Engineering (Honors), Jadavpur University, India. G.P.A. : 8.24 /10

Conference(underlined is as presenter)

- "Rheology of active colloidal suspensions", Choudhury, U., Singh, D. P., Qiu T., Jeong H.H, Mark A.G. and Fischer, P., (*oral presentation*)The Society of Rheology, 88th Annual Meeting, Tampa, Florida, February,2017
- "Nanorheology with nano-propellers in biological fluids", Jeong H.H., Wu Z., Qiu T., Walker D., Mark A.G., Choudhury, U. and Fischer, P.,The Society of Rheology, 88th Annual Meeting, Tampa, Florida, February, 2017
- "Nanodiamond-Swimmers", Choudhury U., Kim J.T., Jeong H.H. and Fischer P., Micro-Nano machines, Hannover, July2016. (*poster*)
- "Surface interactions of active Janus particles on a hexagonal close-packed colloidal crystal surfaces", Choudhury U., Gibbs J.G. and Fischer P. (*oral presentation*) Deutsche Physikalische Gesellschaft Meeting, Berlin, Germany, February 2015
- "Dynamic mechanical properties of Cockroach resilin" Choudhury U. and Dudek D.M.Society of Integrative and Comparative Biology Annual Meeting, Charleston, South Carolina, USA, January 2012. (*oral presentation*)
- A Theoretical Framework for the Determination of Stretch-corrected Laminar Burning Velocity using the Spherical Constant Volume Vessel Method" Ratna Kishore V., Choudhury U., Ray A. and Ravi M.R.. Proceedings of the 6th U.S National Combustion Meeting, Michigan, Ann Arbor ,USA May 2009

Publications

Following is a list of publications by the author which are presented as part of the thesis. These publications form the basis of this Ph.D. thesis (apart from publication 4, which is an additional publication by the author not discussed in this thesis,):

1. Choudhury, U.†, Soler, L., G.† Gibbs, J., Sanchez, S. & Fischer, P. Surface roughness-induced speed increase for active Janus micromotors. *Chem. Commun.* **51,** 8660–8663 (2015).
2. Choudhury, U. †, Straube, A. V. †, Fischer, P., Gibbs, J. G. & Höfling, F. Active colloidal propulsion over a crystalline surface. *New J. Phys.* **19,** 125010 (2017).
3. Kim, J. T. †, Choudhury, U.†, Jeong, H.-H. & Fischer, P. Nanodiamonds That Swim. *Adv. Mater.* **29,** (2017). (selected as back cover)
4. Singh, D. P., Choudhury, U., Fischer, P. & Mark, A. G. Non-Equilibrium Assembly of Light-Activated Colloidal Mixtures. *Adv. Mater.* **29,** 1701328 (2017).
5. Choudhury, U. , Singh, D. P. Qiu, T. &Fischer, P. Chemical nanomotors at the gram scale at high density form an active opto-rheological medium. (*under review*).

† denotes equal contribution

10: Acknowledgements

Firstly, I would like to thank my supervisor Prof. Peer Fischer for his kind guidance, support and encouragement throughout my PhD. I am also obliged to Prof. Andreas Hermann for being my supervisor at the University of Groningen. I would also like to thank Prof. Petra Rudolf, Prof. Thomas Palberg and Prof. Christian Holm for reviewing the thesis and Prof. Ria de Boer and Prof. Giuseppe Portale for being the members defense committee along with the thesis reviewers.

Next, I would like to thank all my lab colleagues who have made my research stay a happy experience : Mariana Alarcón-Correa, Alejandro Posada, John G. Gibbs, Andrew G. Mark, Ji-Tae Kim, Dhruv Singh, Tian Qiu, Hyeon-Ho Jeong, Eunjin Choi, Stefano Palagi, Stefan Knoppe, Zhiguang Wu, Tung-Chun Lee, Alex Solovev, Melanie Adams, Nico Segreto, Jonas Troll, Kai Melde, Johannes Sachs, Vincent Kadiri, Cornelia Miksch, Ute Heinrichs, Debora Walker, Sahand Eslami, Insook Kim, Vijay Chikkadi, Tingting Yu and Jan-Philipp Guenther. My sincere regards to Jutta Hess for her constant administrative support.

I am also grateful to my collaborators Dr. Lluis Soler Turu, Prof. Samuel Sanchez, Prof. Felix Höfling and Prof. Ambarish Ghosh for their insightful scientific discussions.

I would also like to thank my colleagues at the MPI : Arghya Majee, Sutapa Roy and Tamal Das for their invaluable friendship.

Finally, my deepest regards to my family in India who have supported me throughout the journey.